

AD A 043965

12
J
DNA 4225F

INVESTIGATION OF IONOSPHERIC DISTURBANCES

Lockheed Palo Alto Research Laboratory
3251 Hanover Street
Palo Alto, California 94304

28 January 1977

Final Report for Period 15 April 1976--28 January 1977

CONTRACT No. DNA 001-76-C-0247

APPROVED FOR PUBLIC RELEASE;
DISTRIBUTION UNLIMITED.

DDC
SEP 9 1977
C

THIS WORK SPONSORED BY THE DEFENSE NUCLEAR AGENCY
UNDER RDT&E RMSS CODE B322075462 L25AAXYX96623 H2590D.

AD No. _____
DDC FILE COPY

Prepared for
Director
DEFENSE NUCLEAR AGENCY
Washington, D. C. 20305

Destroy this report when it is no longer
needed. Do not return to sender.



UNCLASSIFIED

SECURITY CLASSIFICATION OF THIS PAGE (When Data Entered)

19 REPORT DOCUMENTATION PAGE		READ INSTRUCTIONS BEFORE COMPLETING FORM
1. REPORT NUMBER	2. GOVT ACCESSION NO.	3. RECIPIENT'S CATALOG NUMBER
18 DNA 4225F		
6 INVESTIGATION OF IONOSPHERIC DISTURBANCES		9 TYPE OF REPORT & PERIOD COVERED Final Report, For Period 15 Apr 76 - 28 Jan 77
		14 REPORT NUMBER LMSC/D555985
10 AUTHOR J. B. Cladis, G. T. Davidson L. L. Newkirk, W. E. Francis M. Walt		8. CONTRACT OR GRANT NUMBER(s) DNA 001-76-C-0247
9 PERFORMING ORGANIZATION NAME AND ADDRESS Lockheed Palo Alto Research Laboratory 3251 Hanover Street, Palo Alto, California 94304		10 PROGRAM ELEMENT, PROJECT, TASK AREA & WORK UNIT NUMBERS NWET Subtask L25AAXYX966-23
11 CONTROLLING OFFICE NAME AND ADDRESS Director Defense Nuclear Agency Washington, D.C. 20305		12 REPORT DATE 28 Jan 1977
14 MONITORING AGENCY NAME & ADDRESS (if different from Controlling Office) 12 107p.		13 NUMBER OF PAGES 116
		15 SECURITY CLASS (of this report) UNCLASSIFIED
		15a. DECLASSIFICATION/DOWNGRADING SCHEDULE
16 DISTRIBUTION STATEMENT (of this Report) Approved for public release; distribution unlimited.		
17 DISTRIBUTION STATEMENT (of the abstract entered in Block 20, if different from Report) C		
18 SUPPLEMENTARY NOTES This work sponsored by the Defense Nuclear Agency under RDT&E RMSS Code B322075462 L25AAXYX96623 H2590D.		
19 KEY WORDS (Continue on reverse side if necessary and identify by block number) Trapped Radiation Ionospheric Irregularities Trapped Electron Precipitation Scintillations Pitch-Angle Diffusion Electric Fields Atmospheric Energy Deposition High Altitude Nuclear Effects AURORA Computer Code Farley-Buneman Instability		
20 ABSTRACT (Continue on reverse side if necessary and identify by block number) Methods are described for solving the diffusion equation for trapped particles precipitating in the ionosphere. It is shown that the variation of the particle distribution with spatial location, both latitudinal and longitudinal, must be considered, and that the bounce averaged diffusion equations are inadequate to treat the loss-cone distributions. The coupling of precipitating particles to the ionosphere is described, with applications of the AURORA code. Mid-latitude WIDEBAND observations are described, with a discussion of interpretations based on trapped particle precipitation.		

DDC
SEP 9 1977
C

210118

y/p

UNCLASSIFIED

SECURITY CLASSIFICATION OF THIS PAGE(When Data Entered)

20. ABSTRACT (Continued)

Recent observations are described of loss-cone distributions of ions and electrons which do not fit the simple diffusion model. It is shown that these observations can be accounted for by the presence of kilovolt electric fields aligned with the magnetic field. It is shown that the ionosphere at large distances from a high-altitude nuclear explosion may be unstable to the Farley-Buneman mechanism, thereby providing a new mechanism for ionospheric irregularities.

UNCLASSIFIED

SECURITY CLASSIFICATION OF THIS PAGE(When Data Entered)

PREFACE

We wish to express our thanks to research workers in several laboratories who graciously provided assistance and the data used in the work described here. We are grateful to Dr. Ed Fremouw and Mr. S. Matthews of Stanford Research Institute (Menlo Park) who allowed us access to their unprocessed data from the WIDEBAND receivers; to Dr. S. Fisher of the Naval Research Laboratories (Washington) who made several runs of the MRHYDE code at our request; and to Dr. F. Fajen of Mission Research Corporation (Santa Barbara) who furnished output from the MICE code. We also thank Drs. E.G. Shelley, R.G. Johnson, and R.D. Sharp of Lockheed (Palo Alto) who made available to us unpublished data from their satellite experiments. We wish especially to thank Dr. C.A. Blank of Defense Nuclear Agency for his support and coordination of the research effort.

ADDITIONAL FOR	White Section <input checked="" type="checkbox"/>
NIS	B.H. Section <input type="checkbox"/>
ADD	<input type="checkbox"/>
TRANSFORMED	
1.0.0.0.0.0.0	
BY	DISTRIBUTION/AVAILABILITY CODES
	SPECIAL
A	

TABLE OF CONTENTS

	<u>Page</u>
PREFACE	1
LIST OF ILLUSTRATIONS	3
LIST OF TABLES	5
1. INTRODUCTION	7
2. DIFFUSION OF TRAPPED PARTICLES AND THE DISTRIBUTION OF PRECIPITATING PARTICLES	12
2.1 The Pitch-Angle Diffusion Equation	12
2.1.1 The Bounce-Averaged Diffusion Equation	13
2.1.2 Solution of the Three-Dimensional Diffusion Equation	24
2.2 Tests of the Pitch-Angle Diffusion Theory	38
2.3 Longitudinal Drift and the Filling of the Loss Cone	40
3. OBSERVATIONS OF SCINTILLATIONS IN MID-LATITUDES	49
4. COUPLING OF IONOSPHERE AND MAGNETOSPHERE	60
4.1 Anomalous Phenomena Affecting Coupling	60
4.2 Effects of Electric Potentials and Magnetic Mirrors on Charged Particle Fluxes	63
4.3 Electric Fields Inferred From Satellite Data	69
4.3.1 Satellite Measurements	69
4.3.2 Interpretation of Data	70
5. IONOSPHERIC IRREGULARITIES DUE TO ATMOSPHERIC HEAVE	92
6. CONCLUSIONS AND RECOMMENDATIONS	99
REFERENCES	101

LIST OF ILLUSTRATIONS

<u>Figure</u>		<u>Page</u>
1	Solutions of the averaged diffusion equation for 50 keV protons on $L = 4$.	22
2	The domain of integration of the pitch-angle diffusion equation.	25
3	Comparison of bounce-averaged diffusion calculations with new results.	29
4	Loss-cone distribution of 50 keV protons on $L = 4$; $\langle D_{\alpha_0\alpha_0} \rangle = 10^{-8} \text{ sec}^{-1}$.	32
5	Loss-cone distribution of 50 keV protons on $L = 4$; $\langle D_{\alpha_0\alpha_0} \rangle = 10^{-7} \text{ sec}^{-1}$.	33
6	Loss-cone distribution of 50 keV protons on $L = 4$; $\langle D_{\alpha_0\alpha_0} \rangle = 10^{-6} \text{ sec}^{-1}$.	34
7	Loss-cone distribution of 50 keV protons on $L = 4$; $\langle D_{\alpha_0\alpha_0} \rangle = 10^{-5} \text{ sec}^{-1}$.	35
8	Variation of the edge of the loss cone with geomagnetic longitude.	41
9	Solutions of the averaged diffusion equation for various longitudes; small diffusion coefficient.	44
10	Solutions of the averaged diffusion equation for various longitudes; large diffusion coefficient.	45
11	Filling of the "quasi trapping" electron loss cone observed by a satellite at constant altitude.	46
12	The data of Figure 11 with several solutions to the diffusion equation superimposed.	48
13	Equipotential model for electric fields above the auroral ionosphere.	62
14	The field geometry used in calculations of effects of electric fields.	64
15a	Pitch-angle data obtained on spins 1 and 3 by the CME A detector.	75
15b	Pitch-angle data obtained on spin 2 by the CME A detector.	76

<u>Figure</u>		<u>Page</u>
16a	Pitch-angle data obtained on spin 1 by the CME B detector.	78
16b	Pitch-angle data obtained on spin 2 by CME B detector.	79
16c	Pitch-angle data obtained on spin 3 by the CME B detector.	80
17a	Pitch-angle data obtained on spin 1 by the CME C detector.	81
17b	Pitch-angle data obtained on spin 2 by the CME C detector.	82
17c	Pitch-angle data obtained on spin 3 by the CME C detector.	83
18	Pitch-angle data obtained on spins 1 and 3 by the CME D detector.	84
19	Energy spectra of electrons measured on spins 1 and 3. The triangles are the spectral intensities of the disturbed flux computed from the spin 1 data assuming a .5 kV potential above the satellite.	86
20	Theoretical relationship of loss-cone width observed by electron detectors to the electric potential below the satellite.	87
21	Schematic representation of electric field distribution resulting from the atmospheric heave. R is the effective radius of the "heave" region. E_i is the induced electric field, and E is the electrostatic field.	95

LIST OF TABLES

<u>Table</u>		<u>Page</u>
I.	Range of influence of atmosphere on permanently trapped particle distribution.	17
II.	Minimum pitch-angle diffusion coefficient that allows some filling of the loss cone at all longitudes.	42
III.	Scintillation levels at Stanford.	51
IV.	Observed values of loss cone widths.	88
V.	Values of $e\phi_b$ in keV inferred from loss cone widths.	88
VI.	Observed ratios of loss cone depths.	90
VII.	Computed ratios of loss cone depths.	90

Section 1

INTRODUCTION

Ionospheric disturbances cause severe disruptions of radar and communications systems, and high background rates in optical defense systems. The most troublesome disturbances affecting high frequency wave propagation are the scintillations, which can occur at any time, and are expected to be especially severe after a high-altitude nuclear explosion. An extensive program is now underway to find out how ionospheric disturbances affect radiowave propagation through the ionosphere. The program comprises experimental studies, such as WIDEBAND, on naturally occurring disturbances in the ionosphere, and theoretical studies of the scintillations and of the ionospheric conditions which lead to this occurrence. This report addresses several aspects of the theoretical investigation of ionospheric irregularities. It is mainly concerned with the effects of particles and fields in the upper ionosphere -- a problem which must be solved if the underlying causes of irregularities are to be understood. The emphasis in the first sections is on processes in the natural ionosphere. The last section treats an effect that may be expected to occur after a high-altitude nuclear detonation.

A new method was recently described for calculating the distribution of electrons leaking out of the permanently trapped radiation belts (Ref. 1, 2). The results are important for their implications to magnetospheric physics and the coupling of the ionosphere to the magnetosphere. An important by-product of the calculation is the energy deposited in the upper ionosphere by electrons precipitating in mid-latitude regions ($L \leq 6$). The distribution

of energy deposition can be calculated quite accurately because the method incorporates the AURORA code, which has been carefully developed and tested over a period of many years (Ref. 3, 4, 1). It was therefore suggested that results from this program could be of great value to the interpretation of data from WIDEBAND and other experiments directed at the assessment of radio propagation through the ionosphere. The fundamental advantage is that the precipitation of electrons from the trapped particle belts, and the resultant energy deposition, are more understandable and readily predictable than in the auroral regions. Eventually it might be possible to predict the particle precipitation contribution to ionospheric heating, even without well-coordinated satellite observations -- something that will probably never be accomplished for the auroral regions. The advantages have been somewhat offset by the lack of mid-latitude observational data. The sparsity of particle precipitation data has precluded the calibration of diffusion and precipitation rates. The mid-latitude WIDEBAND data were limited mainly to one station that only operated for a portion of a four month interval, though we intend to look into the possibility of using low elevation data from the WIDEBAND receivers at high latitudes to investigate the northern edge of the mid-latitude region.

Sections 2 and 3 describe a continuation of previous work (Ref. 1) and first attempts at interpreting WIDEBAND data using our results. Section 2.1 is a discussion of the basic theory behind the calculations. It has heretofore been assumed that the conventional bounce-averaged diffusion equation might be adequate to treat the electron precipitation problem. We shall show how our approach is related to the bounce-average method, and why a bounce-averaged

treatment can never yield satisfactory results. Section 2.2 describes further efforts to calibrate the electron diffusion rates by observations of trapped and precipitating particles. The results have not been very encouraging, mainly because of instrumental difficulties. However, some of the difficulties might be overcome by a new method, outlined in Section 2.3, that takes advantage of the variation in electron fluxes due to their longitudinal drift motion. The following section, 3, is concerned with a preliminary analysis of WIDEBAND data. Unfortunately, those data, and the supportive data on magnetic variations, ionospheric densities, and trapped particles did not become available soon enough to allow a detailed statistical analysis for possible correlations. There were, however, a sufficient number of interesting scintillation events at mid-latitudes to lend support to our suggestion that studies of ionospheric activity and particle precipitation could profitably be carried out in mid-latitudes.

Recent satellite measurements of the angular and energy distributions of ions and electrons by Shelley et al. (Ref. 5) and McIlwain (Ref. 6) and electric fields of Mozer et al. (Ref. 7) provide improved information on phenomena affecting the coupling of the ionosphere and magnetosphere and on the acceleration of ion from the upper ionosphere to energies in the keV range. The reason these results are of interest here is that they imply the widespread and frequent occurrence of plasma instabilities that lead to anomalous resistivity and electric "double layers," which, in turn, cause large electric fields aligned along the magnetic field. These phenomena may lead us to modify our entire understanding of the exchange of particles between the ionosphere and magnetosphere, and of the motion of nuclear debris after a high altitude nuclear explosion.

Section 4 describes an interpretation of some ion and electron distributions observed by Shelley et al. (Ref. 5). The events selected were those wherein high fluxes of keV-type H^+ and O^+ ions were observed moving away from the atmosphere and highly directed along the magnetic field. In the analysis, an electric field was assumed extending below and above the satellite along the magnetic field. In the calculations described here the distribution of ions and electrons was followed downward from the observation point, through the electric field region, into the atmosphere, and back up to the observation point. The AURORA code was used to compute the flux of backscattered electrons. The computational model was much simpler than that described in Section 2 -- ignoring the pitch-angle diffusion due to wave-particle interactions at high altitudes. The observations could be explained quite convincingly by passage through a potential drop of as much as 4.5 kV. The data also indicated that high fluxes of keV-type electrons were trapped between the converging magnetic field below and the electric field above.

One of the prime candidates for a mechanism that produces ionospheric irregularities is the Farley-Buneman instability (Ref. 8) that is driven by the kinetic energy in the streaming motion of the plasma. If the streaming velocity is greater than the thermal velocities the instability grows rapidly. Obviously, a high-altitude nuclear explosion, with the attendant plasma motions, is a likely candidate for plasma instabilities. The atmospheric heave drives plasma across the magnetic field, inducing a large electric field. This electric field polarizes the ionospheric, and the polarization

charges propagate to high altitudes along the magnetic field. The resulting electrostatic field extends to large areas of the ionosphere, far beyond the region principally disturbed by the burst. The Farley-Buneman instability can be excited if this electric field in the effective E-region of the ionosphere induces a strong drift motion of the electrons with respect to the ions -- at a rate higher than the ion thermal velocity.

Section 5 describes a test of the Farley-Buneman instability criterion, using some MRHYDE and MICE computer data on upper atmosphere conditions following two H.A.N.E. events. Unfortunately, all of the data required for a complete analysis were not available. Nevertheless, the analysis indicated that the electrostatic field arising from the atmospheric heave is indeed very large and that magnetic field-aligned plasma irregularities due to this instability may be expected to extend to several thousand kilometers from the burst.

Section 2

DIFFUSION OF TRAPPED PARTICLES AND THE DISTRIBUTION OF PRECIPITATING PARTICLES

2.1 THE PITCH-ANGLE DIFFUSION EQUATION

The motions of trapped particles in the magnetosphere can be studied by a statistical treatment that results in a Fokker-Planck diffusion equation. By considering times longer than the particles' gyroperiods one of the six degrees of freedom can be eliminated. Another variable can be eliminated by either assuming uniformity of the distribution in longitude, or by acknowledging that the longitudinal drift motion is predictable, and linear with time. That leaves four parameters (plus time) to describe the particles' distribution - one advantageous choice is L-shell, latitude or position on a field line, energy, E , and pitch angle, α . We may also choose to ignore the L-parameter and concentrate on the physical processes that involve only the remaining three parameters. We do not mean to imply that L-shell - or radial - diffusion has no significant effect on the distribution of precipitating particles. Radial diffusion is important and should eventually be included in the treatment of particle losses (Ref. 9). The remainder of this section is devoted to practical methods for solving the Fokker-Planck equation, primarily by judicious elimination of one or more variables.

2.1.1 The Bounce-Averaged Diffusion Equation

Stably trapped particles interacting with low-level waves, or with other particles obey a diffusion-type equation (Ref. 10,11).

$$\begin{aligned} \frac{\partial f}{\partial t} + V \cos \alpha \left(\frac{\partial f}{\partial s} \right)_{\text{constant ad.inv.}} & \quad (1) \\ = \frac{1}{\sin \alpha} \frac{\partial}{\partial \alpha} \left[D_{\alpha\alpha} \sin \alpha \frac{\partial f}{\partial \alpha} \right] - [\text{energy loss term}] + [\text{sources}] - [\text{losses}] \end{aligned}$$

where $f(t,s,E,\alpha)$ is a phase space number - density distribution function, and $D_{\alpha\alpha}(t,s,E,\alpha)$ is a pitch angle diffusion coefficient. The remaining independent variables are time, t , and distance along a field line, s , (usually measured from the equator); V is the velocity. The energy loss term is important for collisions with particles in the atmosphere (Ref.10), but can generally be ignored for interactions of electrons with waves at high altitudes (Ref. 11, 12). Most of the important physical processes are described by the first term on the right side, so we will concentrate on that term, and ignore the remaining three terms (usually small) except when the source and loss terms are needed for logical consistency.

Equation (1) is a local diffusion equation. The second term, however, must be differentiated with the first adiabatic invariant held constant. A suitable replacement for the local pitch angle is any variable that depends only on the adiabatic invariant. A suitable adiabatic invariant variable is, if energy remains constant,

$$u = 1 - \frac{B_0}{B(s)} \sin^2 \alpha \quad (2)$$

where B_0 ($s = 0$) is the minimum magnetic field strength - or equatorial field - and $B(s)$ is the local field. For free, non-interacting charged particles, u would be $\frac{1}{2}$ times the cosine squared of the pitch angle, α_0 , at the equator; in the present case there is no simple functional relation between u and α_0 .

The diffusion equation can be written

$$\begin{aligned} \frac{\partial f}{\partial t} + v \sqrt{1 - (1-u) \frac{B}{B_0}} \frac{\partial f}{\partial s} & \quad (1) \\ = -h \frac{B}{B_0} \sqrt{1 - (1-u) \frac{B}{B_0}} \frac{\partial}{\partial u} \left[D_{\alpha\alpha} \sqrt{1 - (1-u) \frac{B}{B_0}} (1-u) \frac{\partial f}{\partial u} \right] \\ + \sqrt{1 - (1-u) \frac{B}{B_0}} \frac{\partial}{\partial u} \left[(D_{uu} \sqrt{1 - (1-u) \frac{B}{B_0}}) \frac{\partial f}{\partial u} \right] \end{aligned}$$

The conventional method for treating this equation has been to average over the length of the trajectories between the mirror points, s_1 and s_2 . The element of distance along a particle trajectory is $ds/\cos \alpha$. A simple integration gives

$$\frac{\partial \langle f \rangle}{\partial t} + \frac{v}{T} (f_2 - f_1) = \frac{1}{T} \frac{\partial}{\partial u} \left[\frac{T}{2R_0} \int_{s_1}^{s_2} \frac{ds}{\cos \alpha} D_{uu} \frac{\partial f}{\partial u} \right] = \frac{1}{T} \frac{\partial}{\partial u} \left[T \langle D_{uu} \frac{\partial f}{\partial u} \rangle \right] \quad (4)$$

where the subscripts 1 and 2 indicate values at the conjugate mirror points; $\langle \rangle$ denotes an average over $ds/\cos \alpha$, and T is the "quarter bounce period" integral

$$T = \frac{1}{2R_0} \int_{s_1}^{s_2} \frac{ds}{\cos \alpha} \quad (5)$$

The constant R_0 has the dimensions of a length; in a dipole field it is just the radial distance to the equatorial crossing. In a (nearly) symmetric dipole field a simple empirical approximation holds for T (Ref. 13).

$$T(u) \approx 1.380173 - .639693 (1-u)^{3/8} \quad (6)$$

In Equation (4) the commutativity of the operations $\frac{\partial}{\partial u}$ and $\langle \rangle$ is ensured if $D_{\alpha\alpha}$ and $\frac{\partial f}{\partial u}$ remain bounded at the mirror points. The separation of D_{uu} and $\frac{\partial f}{\partial u}$ in the average on the right side would further simplify the equation, though this requires an assumption that is not always warranted. Usually the diffusion rate has been assumed low enough that f does not appreciably vary over a particle trajectory. If f is independent of s a "bounce averaged" equation results

$$\frac{\partial f}{\partial t} = \frac{1}{T} \frac{\partial}{\partial u} \left[\langle D_{uu} \rangle T \frac{\partial f}{\partial u} \right] \quad (7)$$

[Note that an average over $ds/\cos \alpha$ is the only way to remove the $\partial f/\partial s$ term, though the original justification for the averaging procedure did not take this into account (Ref. 10)]. In the loss cone, $\alpha < \alpha_c$, the assumption of uniformity of f along the field line cannot be valid. In the limiting case of a totally absorbing atmosphere, where no particles are scattered backward into the upward direction, the df/ds term becomes Vf_2/T . The resulting equation, which has been frequently used for the loss cone, is

$$\frac{\partial f}{\partial t} = \frac{1}{T} \frac{\partial}{\partial u} \left[\langle D_{uu} \rangle T \frac{\partial f}{\partial u} \right] - \frac{2f}{\tau_B}$$

where τ_B is the bounce period ($4R_0T/V$). Somewhat different derivations have been used elsewhere to justify Equation (8). An alternate method is to assume that the particles are lost within one-fourth bounce period, on the average. The loss term is then $4f/\tau_B$ (Ref. 14, 15, 16, 17).

It is relatively easy to demonstrate that the bounce averaging procedure runs into difficulties when the variability of f with s is taken into account.

When f depends on spatial position it is not generally possible to write a diffusion equation for $\langle f \rangle$. A case of interest is where $D_{\alpha\alpha}(u,s)$ is a function of u only, independent of s (this is not the same as the assumption that $D_{\alpha\alpha}(\alpha,s)$ is a function of α only). There follow from Equations (4) and (5) the simple relations (Ref. 18).

$$\langle D_{uu} \rangle = \frac{Z(1-u)}{T} D_{\alpha\alpha} \quad (9)$$

$$\begin{aligned} Z &= \frac{1}{2R_0} \int_{s_1}^{s_2} \frac{B_0}{B} \cos \alpha \, ds \\ &= \frac{1}{2} \int_0^u T(u) \, du \end{aligned} \quad (10)$$

The bounce averaged diffusion equation is now

$$\begin{aligned} \frac{\partial \langle f \rangle}{\partial t} + \frac{v}{T} (f_2 - f_1) \\ &= \frac{1}{T} \frac{\partial}{\partial u} \left[\langle D_{uu} \rangle T \langle \frac{\partial f}{\partial u} \rangle \right] \\ &= \frac{1}{T} \frac{\partial}{\partial u} \left[\langle D_{uu} \rangle T \left(\frac{\partial \langle\langle f \rangle\rangle}{\partial u} + \frac{T}{Z} \langle\langle f \rangle\rangle - \frac{T}{2Z} \langle f \rangle \right) \right] \end{aligned} \quad (11)$$

where the symbols $\langle\langle \rangle\rangle$ denote a new kind of average

$$\langle\langle X \rangle\rangle = \int_{s_1}^{s_2} X \frac{B_0}{B} \cos \alpha \, ds / \int_{s_1}^{s_2} \frac{B_0}{B} \cos \alpha \, ds \quad (12)$$

Thus an attempt to remove one integration variable, s , has only resulted in the appearance of a new dependent variable, $\langle\langle f \rangle\rangle$, on the right side of the diffusion equation. It may be concluded that, except for special cases, the bounce-averaged diffusion equation is not valid for the treatment of distributions in and near the loss cone. Bounce-averaging is only justified for slow

diffusion of "permanently" trapped particles with large pitch angles.

A rough criterion can be formulated for the range of validity of Equation (7). If there is a cutoff equatorial pitch angle, α_c , below which all the trapped particles interact strongly with the atmosphere within half a bounce period, the distribution can be symmetric in s only for pitch angles α_0 greater than $\alpha_c + \Delta\alpha_0$, where

$$\begin{aligned} \Delta\alpha_0 &\approx \sqrt{\tau_B \langle D_{\alpha_0 \alpha_0} \rangle} \\ &= \sqrt{\tau_B \langle D_{\alpha\alpha} \frac{B_0}{B} \frac{\cos^2 \alpha}{\cos^2 \alpha_0} \rangle} \end{aligned} \quad (13)$$

Values of $\langle D_{\alpha_0 \alpha_0} \rangle$ are available from several sources (e.g. Ref. 19,20); normally $\langle D_{\alpha_0 \alpha_0} \rangle$ is expected to be less than $10^{-4} \text{ rad}^2 \text{ sec}^{-1}$. Table I shows the numerical factors that give $\Delta\alpha_0$ from $\langle D_{\alpha_0 \alpha_0} \rangle$. Except for the case of strong diffusion, when $\langle D_{\alpha_0 \alpha_0} \rangle$ becomes comparable with $1/\tau_B$, Equation (7) is satisfactory for most of the trapped particles. But near and within the loss cone, $\alpha_0 \lesssim \alpha_c$, the pitch angle diffusion equation must be solved explicitly for (at least) three independent variables.

To see what can be accomplished with Equations (7) and (8), consider the idealized case where

$$D_{\sin \alpha_0, \sin \alpha_0} = D_0 (\sin \alpha_0)^q \quad (14)$$

TABLE I
 Range of Influence of Atmosphere on
 Permanently Trapped Particle Distribution

E ev	$\Delta\alpha_0$ (electrons)	$\Delta\alpha_0$ (protons)
10^3	$1.68\sqrt{L < D >}$	$11.1\sqrt{L < D >}$
10^4	.953 "	6.26 "
10^5	.568 "	3.52 "
10^6	.434 "	1.98 "
10^7	.420 "	1.12 "

and the source that maintains the trapped particles is

$$S = S_0 (\sin \alpha_0)^2 \quad (15)$$

where D_0 and S_0 are constants. The diffusion equation for a stationary distribution ($\alpha/\alpha_0 = 0$) is, after replacing $\sin \alpha_0$ by x ,

$$\text{trapped: } 0 = \frac{1}{\tau_B} \frac{1}{x} \frac{\partial}{\partial x} \left[D_0 \tau_B x^{q+1} \frac{\partial f}{\partial x} \right] = S_0 x^{p-1} \quad x > x_c \quad (16a)$$

$$\text{loss cone: } 0 = \frac{1}{\tau_B} \frac{1}{x} \frac{\partial}{\partial x} \left[D_0 \tau_B x^{q+1} \frac{\partial f}{\partial x} \right] = \frac{2f}{\tau_B} \quad x \leq x_c \quad (16b)$$

To simplify the solutions let τ_B be a constant, equal to the bounce period at x_c . The solutions of Equation (16a) are straightforward, and give for trapped particles

$$f = - \frac{S_0}{D_0} \frac{1}{(p+2)(p+2-q)} x^{p+2-q} + C_1 x^{-q} + C_2 \quad q \neq 0 \quad (17a)$$

$$f = - \frac{S_0}{D_0} \frac{1}{(p+2)^2} x^{p+2} + C_1 \ln x + C_2 \quad q = 0 \quad (17b)$$

where the C's are constants. The loss cone equation, (16b), is Bessel's equation, and gives solutions in terms of Bessel functions, I_n , of imaginary argument

$$f = C_3 x^{-q/2} \left\{ \frac{2}{2-q} \left(\frac{2y^{2-q}}{D_0 \tau_B} \right)^{1/2} \right\} \quad q \neq 2 \quad (18a)$$

$$f = C_3/x \quad \left\{ \right. \quad q = 2 \quad (18b)$$

It is necessary to match the functions and their first derivatives at x_c ; the remaining constant can be eliminated by letting $f = 1$ at $x = 0$. The solutions for $q \neq 2$ are

$$r = 1 + \frac{S_0}{D_0} \frac{1}{(p+2)^2} (1 - x_c^{p+2}) - \frac{\ln x}{\ln x_c - x/x_c} \left\{ 1 + \right. \quad (19a)$$

$$\left. \frac{S_0}{D_0} \frac{1}{(p+2)^2} (1 - x_c^{p+2}) + x \frac{S_0}{D_0} \frac{1}{p+2} x_c^{p+1} \right\} \quad q = 0, x > x_c$$

$$r = \left\{ 1 - \left[\left(\frac{2x_c}{D_0 \tau_B} \right)^{1/2} \right] / \left[\left(\frac{2x_c}{D_0 \tau_B} \right)^{1/2} \right] \right\} \left\{ \frac{x}{x - x_c \ln x_c} \right\} \quad (19b)$$

$$x \left\{ 1 + \frac{S_0}{D_0} \frac{1}{(p+2)^2} (1 - x_c^{p+2}) + \frac{S_0}{D_0} \frac{1}{p+2} x_c \ln x_c \right\} \quad q = 0, x \leq x_c$$

$$r = - \frac{S_0}{D_0} \frac{1}{(p+2)(p+2-q)} x^{p+2-q} \quad (19c)$$

$$+ \left\{ 1 + \frac{S_0}{D_0} \frac{1}{(p+2)(p+2-q)} (1 - x_c^{p+2-q}) + x \frac{S_0}{D_0} \frac{p+2-2}{(p+2)(p+2+q)} x^{p+1-q/2} \right.$$

$$\left. / \left\{ x^q (1 - x_c^{-q} - q x x_c^{-1-q/2}) \right\} + \left\{ -x_c^{-q} - q x x_c^{-q/2-1} \right. \right.$$

$$\left. + \frac{S_0}{D_0} \frac{1}{(p+2)(p+2+q)} (2 - x_c^{-q} - x_c^{p+2-q}) + \frac{S_0}{D_0} \frac{x}{(p+2)(p+2+q)} \right.$$

$$\left. \left[-q x_c^{-1-q/2} + (p+2-q) x_c^{p+1-q/2} \right] \right\} / \left\{ 1 - x_c^{-q} - q x x_c^{-1-q/2} \right\} \quad q \neq 0, x > x_c$$

$$r = \left\{ x^{-q/2} / \left[\frac{2}{2-q} \left(\frac{2x_c}{D_0 \tau_B} \right)^{1/2} \right] \right\} / x_c^{-q/2} \quad (19d)$$

$$\left\{ \frac{2}{2-q} \left(\frac{2x_c}{D_0 \tau_B} \right)^{1/2} \right\} \left\{ -q x x_c^{-1-q/2} + \frac{S_0}{D_0} \frac{q}{(p+2)(p+2+q)} \right.$$

$$\left. x x_c^{-1-q/2} (x_c^{p+2-q-1}) + \frac{S_0}{D_0} \frac{p+2-q}{(p+2)(p+2+q)} x x_c^{p+1-q/2} (x_c^{-q} - 1) \right\}$$

$$\left\{ 1 - x_c^{-q} - q x x_c^{-1-q/2} \right\}$$

$$X = \sqrt{\frac{D\tau_B}{2}} \left| \frac{q/2-q}{2-q} \left[\frac{2}{2-q} \left(\frac{2x_c^{2-q}}{D_o\tau_B} \right)^{1/2} \right] \right| \quad (1a)$$

$$/ \left| \frac{2/2-q}{2-q} \left[\frac{2}{2-q} \left(\frac{2x_c^{2-q}}{D_o\tau_B} \right)^{1/2} \right] \right|$$

These results are fairly insensitive to the strength of the source. A great simplification, therefore, occurs in the limit as S_o becomes zero; the loss cone solutions are:

$$f \sim \frac{\sqrt{D_o\tau_B/2} \Big|_o \left[\left(\frac{2 \sin^2 \alpha_o}{D_o\tau_B} \right)^{1/2} \right]}{\sqrt{D_o\tau_B/2} \Big|_o \left[\left(\frac{2 \sin^2 \alpha_c}{D_o\tau_B} \right)^{1/2} \right] - \sin \alpha_c \ln (\sin \alpha_c) \Big|_1 \left[\left(\frac{2 \sin^2 \alpha_c}{D_o\tau_B} \right)^{1/2} \right]} \quad (2a)$$

$q = 0$

$$f \approx (\sin \alpha_o)^{-q/2} I_{q/2-q} \left[\frac{2}{2-q} \left(\frac{2 \sin \alpha_o^{2-q}}{D_o\tau_B} \right)^{1/2} \right] \sin \alpha_c^{q-1} \sqrt{\frac{D_o\tau_B}{2}} \quad (2b)$$

$$/ \left\{ (1 - \sin \alpha_c^q) I_{2/2-q} \left[\frac{2}{2-q} \left(\frac{2 \sin \alpha_c^{2-q}}{D_o\tau_B} \right)^{1/2} \right] \right.$$

$$\left. - q \sin \alpha_c^{q-2/2} \sqrt{\frac{D_o\tau_B}{2}} I_{q/2-q} \left[\frac{2}{2-q} \left(\frac{2 \sin \alpha_c^{2-q}}{D_o\tau_B} \right)^{1/2} \right] \right\}$$

$q \neq 0$.

These are similar to the solutions for the same case found by Theodoridis and Paolini (Ref. 14) except that they normalized their solutions somewhat differently.

Several solutions for the weak source, $q = 0$ case are shown in Figure 1. The figure was drawn for 50 kev protons, which are not reflected by the atmosphere, on $L = 4$. The reason for considering protons, is that the

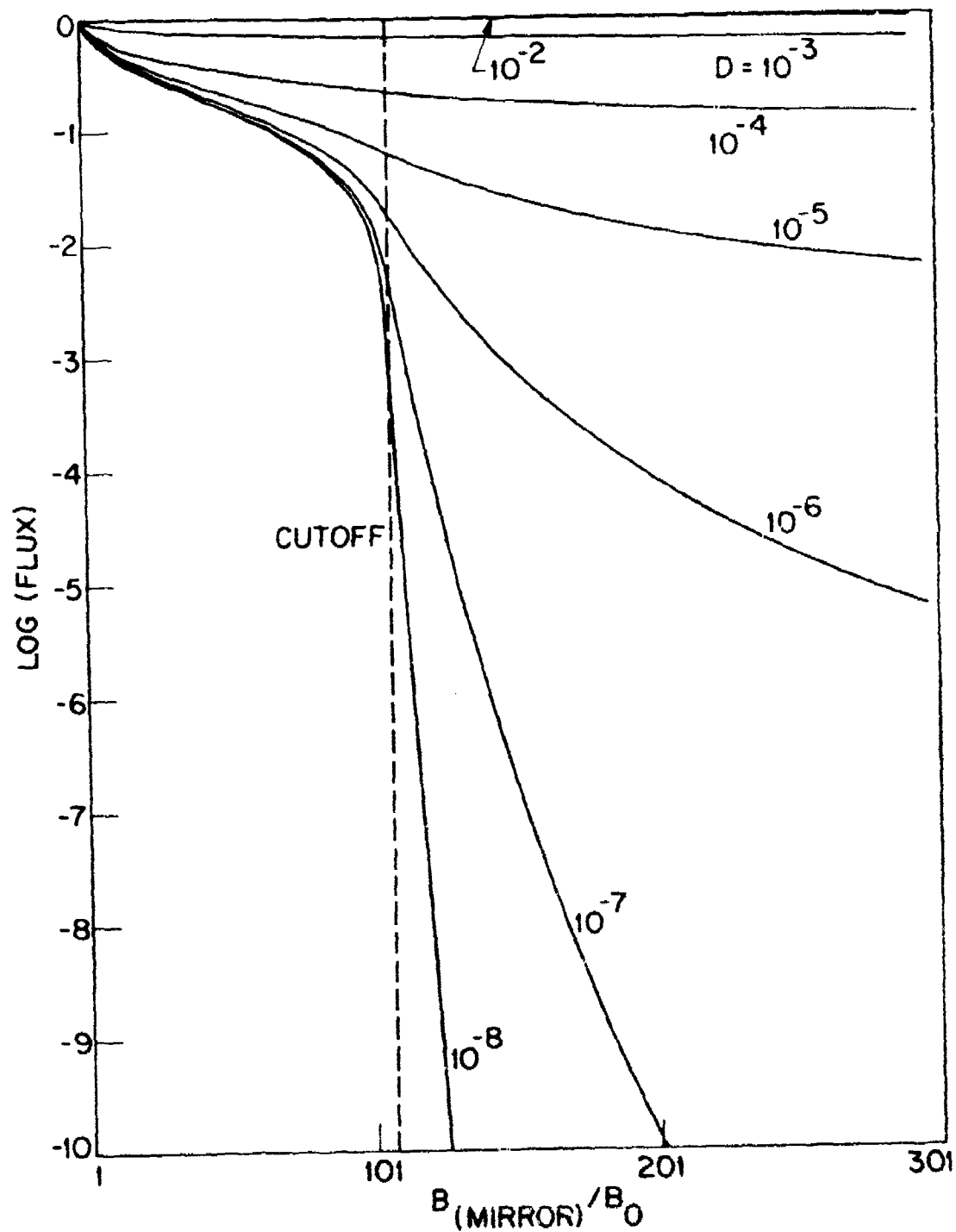


Figure 1 Solutions of the averaged diffusion equation for 50 keV protons on L=4. The individual curves are labeled with the value of the assumed (constant) diffusion coefficient $\langle D_{\alpha\alpha_0} \rangle$ in $\text{rad}^2 \text{sec}^{-1}$.

solutions here can be compared in the following section with the correct solutions without the complication of backscatter by the atmosphere. Some of the features of Figure 1 are expected in the solutions resulting from an explicit integration along the field line. For instance the bounce-averaged diffusion equation predicts the level of diffusion at which the magnetic field disappears and the distribution approaches isotropy. The main point is that solutions of the bounce-averaged diffusion equation appear reasonable and in agreement with intuition, even though they are founded on incorrect assumptions.

2.1.2 Solution of the Three-Dimensional Diffusion Equation

The integration of Equation(3) poses some novel difficulties, mainly because of the distortion of the domain of integration. The numerical techniques were described previously (Ref. 1), so the following discussion is devoted mainly to fundamental questions.

The time integration of the pitch angle diffusion equation is not always interesting, and can be avoided by assuming either a steady state, or a lowest eigenmode decay with

$$f = g(u, s) e^{-t/\tau} \quad (21)$$

The characteristic decay period is τ . The differential equation for g is

$$\frac{\partial g}{\partial v} = \frac{\partial}{\partial u} \left[\frac{R_0}{V} D_{uu} \frac{1}{\sqrt{1-(1-u)B/B_0}} \frac{\partial g}{\partial u} \right] \quad (22)$$

where v is the dimensionless distance from the equatorial plane, S/R_0 . The domain of integration (for a dipole field) is shown in Figure 2. The extreme limits of v are $\pm T(0) = \pm 1.380173$. The domain of integration is bounded on the right by the curve $v = v_m(u)$, where the subscript m denotes that a parameter is evaluated at the mirror point. The figure shows only half of the domain; the earth's field is sufficiently symmetric that the lower half can be considered a reflection of the upper half. The particles generally enter the atmosphere at different values of v , say $-v_{c1}$ and $+v_{c2}$, in the two opposite hemispheres, so the integration is not really symmetric. Several horizontal dashed lines have been drawn to indicate for different L shells the v_c values

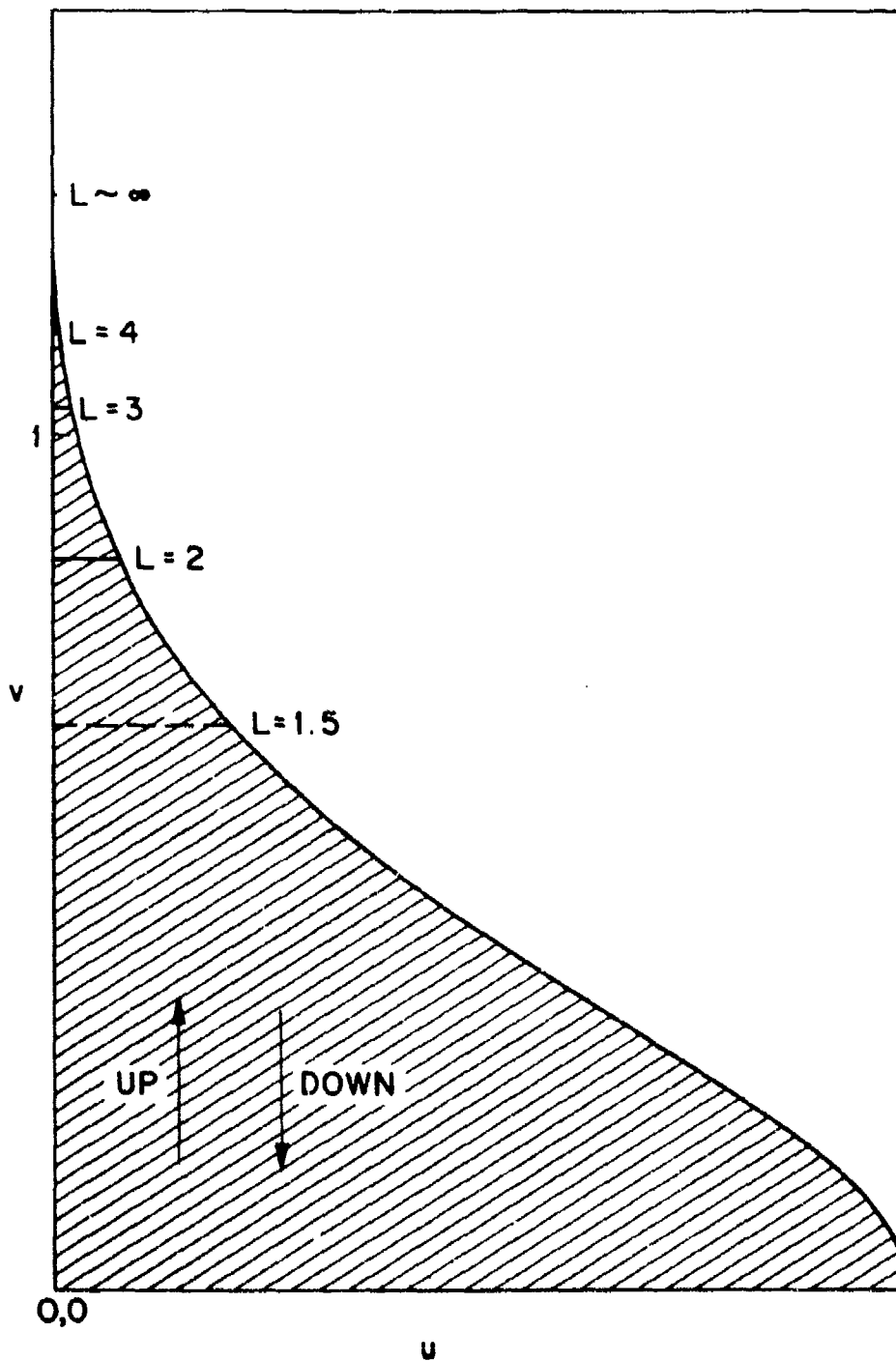


Figure 2. The domain of integration of the pitch angle diffusion equation.

where atmospheric scattering and energy loss must be brought into the diffusion equation.

The transformation from local pitch angle, α , to adiabatic invariant variable u , has altered the domain of integration in another way that is not immediately apparent in Figure 2. Everywhere except at the equator ($v = 0$) the distribution in u has been split into two separate parts: a group of particles going in one direction with $\alpha_0 \lesssim \arcsin \sqrt{\frac{B}{B_0}} (1-u)$ and another group going in the opposite direction with $\alpha_0 \gtrsim \pi - \arcsin \sqrt{\frac{B}{B_0}} (1-u)$. The choice of $u \approx \cos^2 \alpha_0$ rather than $\sim \cos \alpha_0$ has caused the separate regions to lie on top of one another, though they are actually joined only at the point $v = 0, u = 1$. A simple way around the difficulty is to label the two distributions with superscripts UP and DOWN, and perform the v integration in each direction.

If $f(\alpha)$ is to be continuous at $\alpha = \frac{\pi}{2}$, it follows that, on the line $v = v_m(u)$

$$g^{\text{UP}}(u, v_m) = g^{\text{DOWN}}(u, v_m) \quad (23)$$

If the domain were symmetric about $v = 0$, only one g would need to be considered with

$$g(u, v_m) = g(u, -v_m) \quad (24)$$

This condition leads immediately to the conclusion that g cannot be separated into a function of v multiplied by a function of u (as f was separated to give g and a function of t). If g were separable the v eigenfunctions would have the form $\exp(-Cv)$; which is incompatible with Equation (24) except in the trivial case $C = 0$ (or f independent of s).

It also appears that, if $\partial g/\partial v$ is to remain bounded at $v = v_m$ the derivative $\partial g/\partial u$ must vanish at the mirror points. For most of the interesting pitch angle diffusion mechanisms, the diffusion coefficient approaches zero so fast at $\alpha = \pi/2$ that the two distributions, g^{UP} and g^{DOWN} , can be considered fully independent. Even if $D_{\alpha\alpha}$ does not approach zero at least as fast as $\cos \alpha$, the derivative condition follows from the differential equation, 22.

The boundary condition at $u = 1$ is

$$\left. \begin{aligned} \frac{\partial g}{\partial \alpha} = 0 \\ \alpha = 0 \end{aligned} \right\} \alpha = 0 \quad (25)$$

This does not imply that $\partial g/\partial u$ is zero, though this type of boundary condition on $g(u)$ is fairly easy to incorporate in a numerical finite difference integration.

The most interesting boundary is at $v = v_c$; here the integration switches over from generally slow pitch angle diffusion at nearly constant energy to rapid diffusion and energy loss due to collisions with atmospheric atoms and molecules. The time scales in the two v regions are so vastly different that it is impractical to solve the combined diffusion equations in a routine fashion, integrating over both regions simultaneously until convergence is attained. The characteristic times for diffusion in the magnetosphere are hours to days; the characteristic times for diffusion in the atmosphere are less than the particles' bounce periods - of the order seconds or less. It is just this disparity that renders liable to suspicion any attempt to treat the distinct physical processes on an equal footing. For example Spjeldvik and Thorne (Ref. 21) attempted to treat the atmospheric interactions by introducing a diffusion coefficient in the bounce-averaged diffusion equation that was very large in the loss cone region. Apart from the difficulties of constructing a numerical solution across the boundary

where some parameters change by orders of magnitude, their results do not appear entirely reasonable. At the transition between the two modes of diffusion they show a sudden, steep drop, followed by a nearly isotropic distribution within the loss cone. Yet one would expect the downgoing flux at the top of the atmosphere to show a nearly exponential fall-off at the transition, with a characteristic scale given by Equation (13). In Figure 3 [similar to Figure 3 of Ref. 1 except that the no-backscatter case shows the new results of Equation (19)] are compared to the Spjeldvik and Thorne results and our new results. For a wave field of 30 mV the predicted diffusion coefficient for 50 keV electrons is approximately

$$\langle D_{\alpha_0 \alpha_0} \rangle \approx 10^{-4} \text{ sec}^{-1} \quad (26)$$

This gives a $\Delta\alpha_0$ of about $.5^\circ$ at the equator. The distribution at 300 keV altitude should therefore be spread out over nearly 18° near the "cutoff" at 75° . The results of Spjeldvik and Thorne fall off much faster than the expected $\exp(\alpha/18^\circ)$ rate; our results are consistent with the expected fall-off rate, and are nearly indistinguishable from the bounce-averaged results where those results are expected to be applicable ($\alpha \gtrsim 60^\circ$).

A few words of caution are in order here. While scattering within the atmosphere may be treated in the numerical integration as a boundary condition at $v = v_c$, it is not generally possible to construct a simple boundary condition there. Consider the simple case where no particles are assumed to be reflected, or

$$g^{UP}(u, v_c) = 0 \quad (27)$$

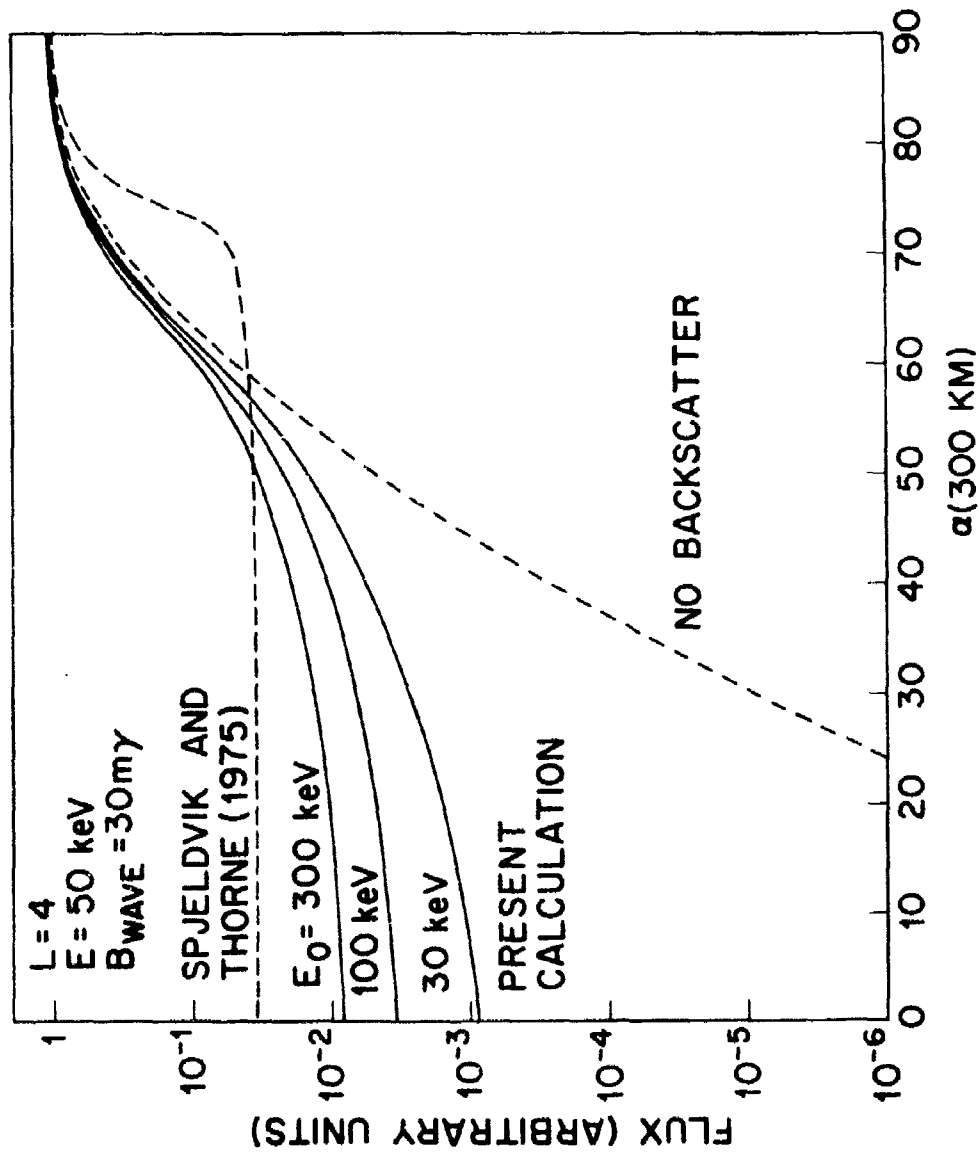


Figure 3. Comparison of bounce-averaged diffusion calculations with new results. The curve marked SPJELDVIK and THORNE is from Ref. 21. The curve labeled NO BACKSCATTER is a plot of Equation (19).

This condition is incompatible with Equation (22) unless ϵ^{DOWN} is also zero at $v_m = v_c$, which in turn denies the possibility of particle loss in the atmosphere. The difficulty is removed if the particles which would mirror a small, but finite, distance beyond v_c are returned after being slightly attenuated. A simple prescription based on this observation can be used in most situations where the physical processes are understood. Often the "penetration depth" is small enough that the mathematical difficulties only affect one point $v_m(u_1) = v_c$ in an array of discrete points.

Ideally, the integration would be joined across the boundary at v_c , to a detailed solution of the Fokker Planck equation describing scattering in the atmosphere. The AURORA code generally suffices for that purpose except that the change in the pitch angle due to magnetic reflection was incorporated in the code only in an approximate fashion. To the best of our knowledge, none of the atmospheric scattering and energy deposition codes have explicitly taken into account the precautions discussed above. As a result it has taken some experimentation to establish the optimum altitude for the transition to atmospheric scattering. In our previous calculations an altitude of 150 to 180 km was chosen. At higher altitudes (above 200 km), errors quickly build up, even in the parts of the distribution that are not strongly affected by the atmosphere. This means that it might not always be feasible to obtain reliable results for electron energies below 1 keV.

The case of zero reflection is very much like what actually happens to trapped protons. Protons entering the atmosphere are rapidly degraded to thermal energies before suffering appreciable deflection (Ref. 10). The steady state differential equation (22) has been solved for a range of values of D_{OX} up to the limit of strong diffusion. The most readily accessible published values of the diffusion

coefficient (e.g. Ref. 19) are for the average $\langle D_{\alpha_0 \alpha_0} \rangle$. The simplest assumption about the form of $D_{\alpha\alpha}$ is that it is a function only of α_0 . It is curious that this assumption leads to values of $\langle D_{\alpha_0 \alpha_0} \rangle$ that are just slightly less than one-half $D_{\alpha\alpha}$ over most of the range of α_0 . The conversion formula is, from Equations 6 and 9

$$\langle D_{\alpha_0 \alpha_0} \rangle = \frac{Z}{T \cos^2 \alpha_0} D_{\alpha\alpha} \quad (28)$$

$$\approx \frac{.332 + .169 \tan^2 \alpha_0 (\sin^{3/4} \alpha_0 - 1)}{1 + .463 \sin^{3/4} \alpha_0} D_{\alpha\alpha}$$

The diffusion coefficient $\langle D_{\alpha_0 \alpha_0} \rangle$ was also assumed independent of α_0 .

Some sample results of calculations for 50 keV protons on $L = 4$ are shown in Figures 4 through 7. These results should be compared with Figure 1, which treats the same case by the bounce averaging method. However, it is now possible to calculate the distribution at any point along the field line. Even if the bounce-averaged diffusion equation were fully applicable it would only give a sort of "average" distribution. In the cases shown we have plotted the distribution at the equator and the distribution at the top of the atmosphere (in terms of an adiabatic invariant parameter $B_m/B_0 = 1/1-u$).

At small values of B_m/B_0 there is a discrepancy that is simply a consequence of stopping the calculation before the solutions for particles with large pitch angles had fully converged. In this region the bounce-averaged equation gives better results with less demands on computer time. The new results beyond $B_m/B_0 \sim 50$ are satisfactory, and should be accepted as the correct solutions against which others should be judged. It is peculiar that for moderate diffusion rates the averaged diffusion equation results would agree

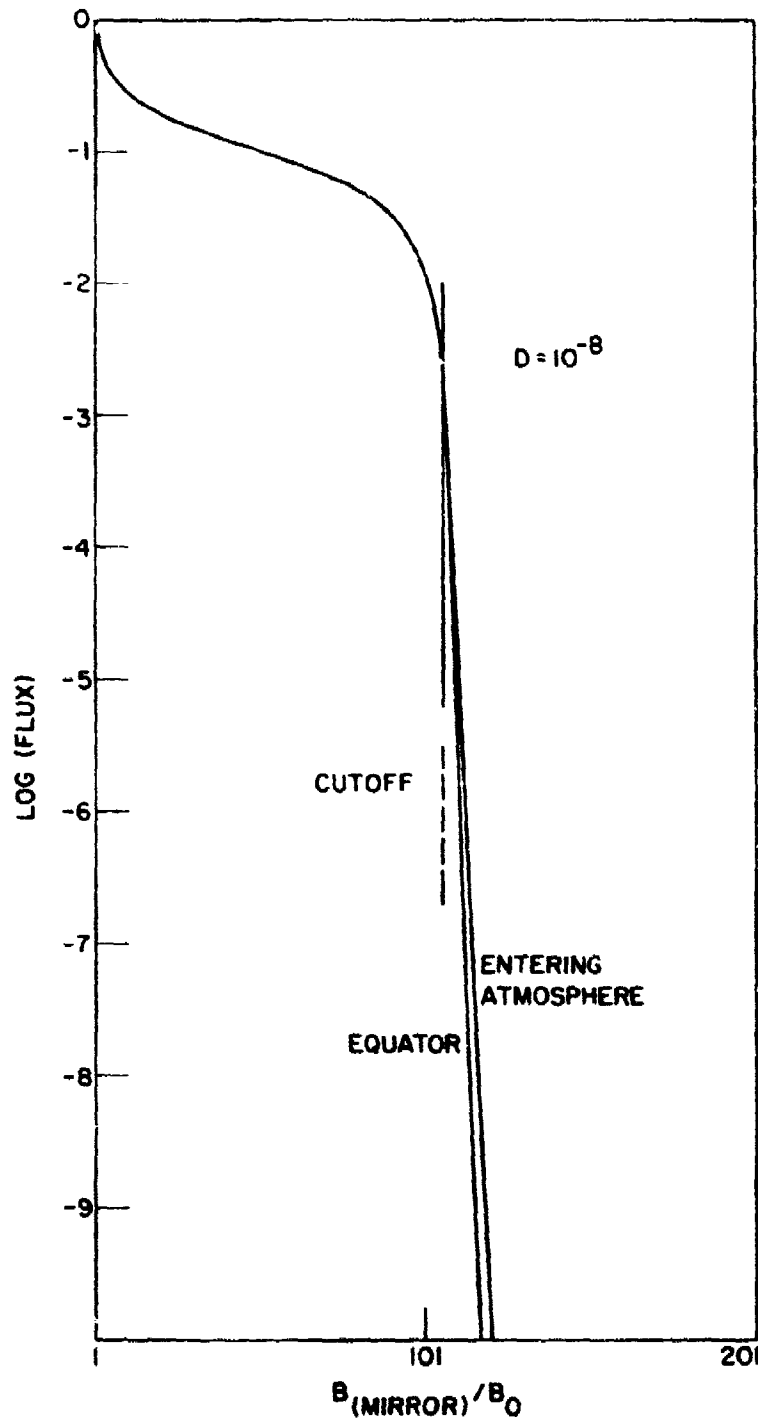


Figure 4. Loss-cone distributions of 50 keV protons on $L=4$; $\langle D_{\alpha_0 \alpha_0} \rangle = 10^{-8} \text{sec}^{-1}$. The two curves shown are for the distribution at the equator, and for the distribution going downward at the top of the atmosphere.

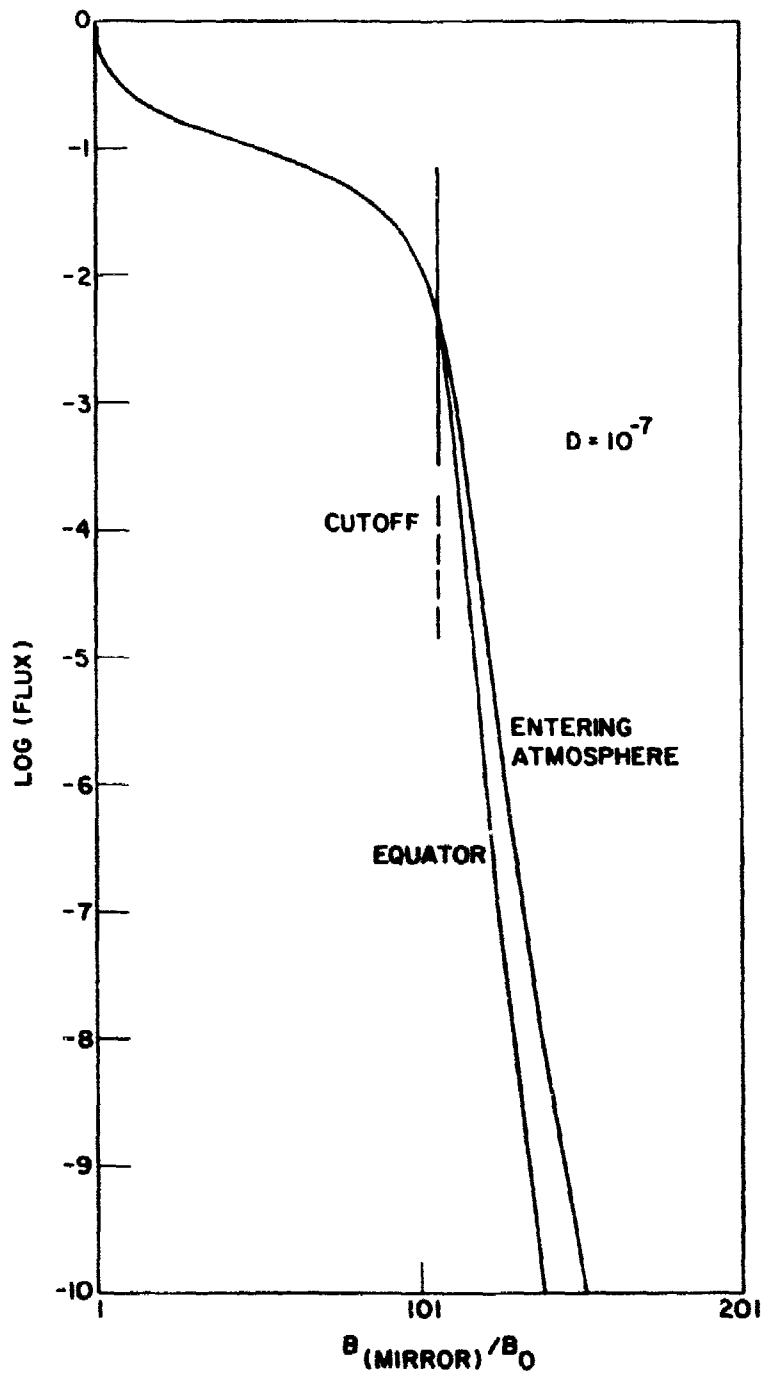


Figure 5. Loss-cone distributions of 50 keV protons on $L=4$; $\langle D_{\alpha_0 \alpha_0} \rangle = 10^{-7} \text{sec}^{-1}$. The two curves shown are for the distribution at the equator, and for the distribution going downward at the top of the atmosphere.

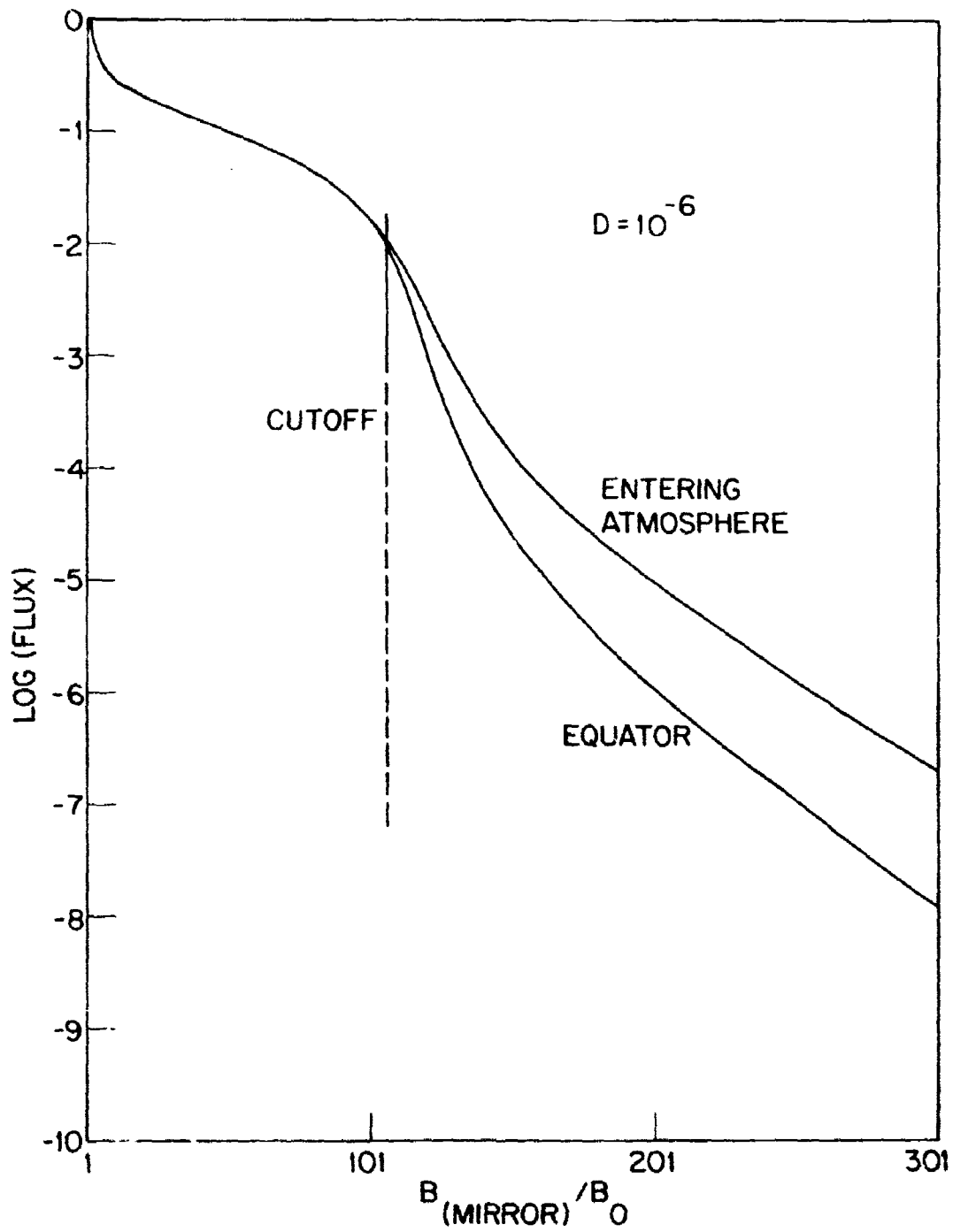


Figure 6. Loss-cone distributions at 50 keV protons on $L=4$; $\langle D_{\alpha\alpha\alpha_0} \rangle = 10^{-6} \text{sec}^{-1}$. The two curves shown are for the distribution at the equator, and for the distribution going downward at the top of the atmosphere.

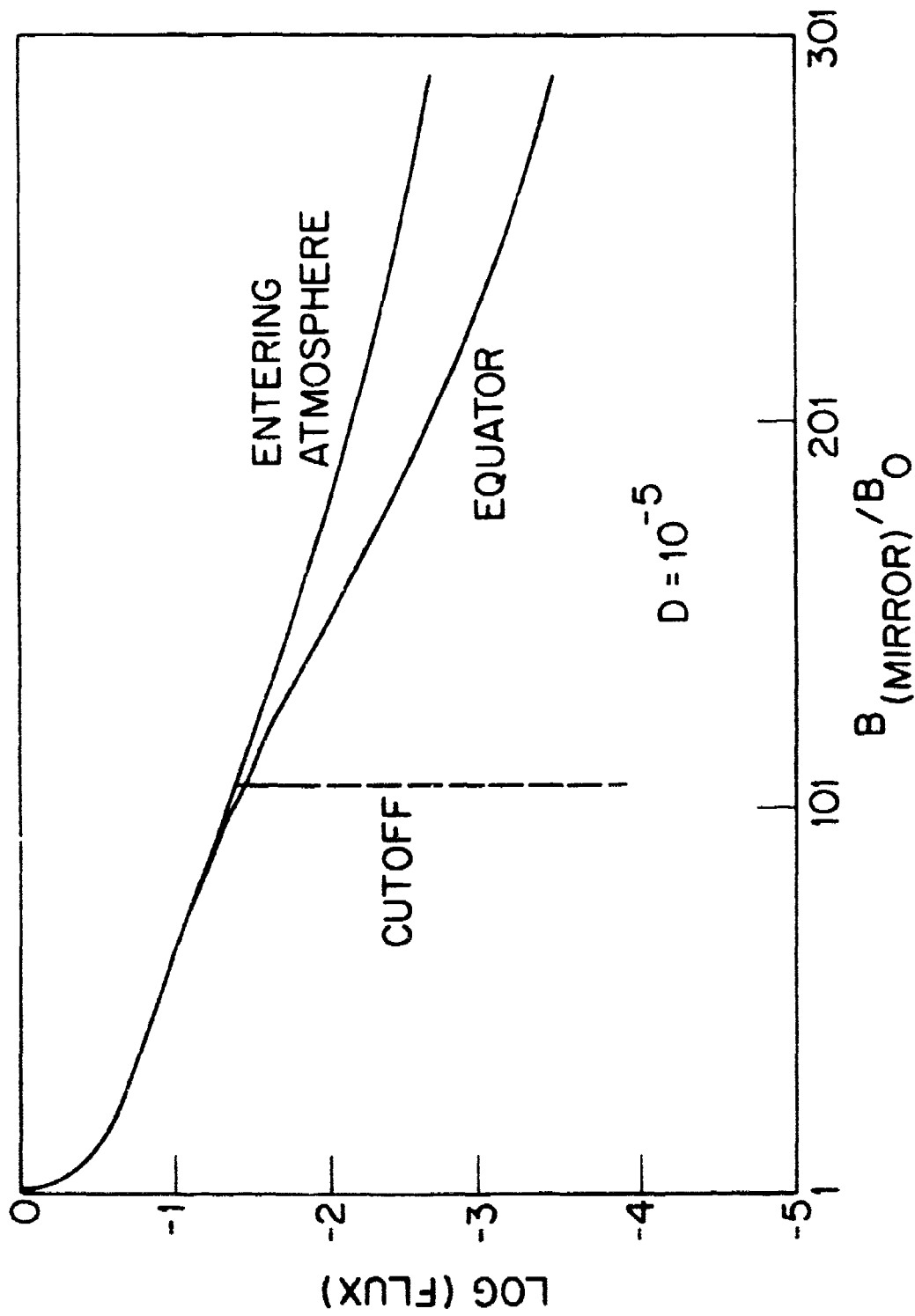


Figure 7. Loss-cone distributions of 50 keV protons on $L=4$; $\langle D_{\alpha_0 \alpha_0} \rangle = 10^{-5} \text{ sec}^{-1}$. The two curves shown are for the distribution at the equator, and $\alpha_0 \alpha_0$ for the distribution going downward at the top of the atmosphere.

almost exactly with the new results, except that the assumed diffusion coefficient must be lower by factor of about 2, or the loss rate raised to hf/τ_B - just what had been assumed in earlier work. This seems to be fortuitous; the correction factor varies from near 1 to a value much greater than 2 at very small diffusion coefficients. Yet, for the most part the agreement between the two kinds of results is very good.

The fact that the bounce-averaged proton distributions are so near to the correct solutions in the loss cone might lead one to suppose that the bounce averaged equation could work as well for electrons, given a satisfactory heuristic loss term. There are several factors that work against this supposition. First, there is the expectation that the distribution at very small pitch angles should be almost entirely due to the atmospheric scattering processes, which are exceedingly difficult to incorporate in a simple model. Second, the energy loss of electrons in the atmosphere must be considered. It is unlikely that calculations at a single energy such as reported by Spjeldvik and Thorne, (Ref. 21) could ever yield more than a crude order-of-magnitude estimate of the total precipitation rate (though their distributions are questionable, comparisons with our new results indicate that both methods predict approximately the same number of particles in the loss cone).

The major conclusions that can be drawn at this point are that our basic method is sound, and that the only significant uncertainties are in the predictions of backscattered electron distributions by the AURORA code. The close agreement of the proton distributions with results of bounce-averaged calculations indicates that the numerical integration method is giving correct results. That the bounce averaged formulation is good over such a large range of pitch angles means that the seemingly crude assumption for the form of D_{∞}

cannot appreciably degrade the results. Only if the diffusion coefficients vary markedly for particles in the loss cone can the assumed form of $D_{\alpha\alpha}$ have any bearing on the correctness of the results. So all that needs to be done to verify the method is the calibration of the diffusion coefficients, and the confirmation of the backscatter predictions - both non-trivial exercises, as will be apparent in the following section.

2.2 TESTS OF THE PITCH-ANGLE DIFFUSION THEORY

A careful observation of the distribution of electrons within the loss cone has great potential as a means of determining both diffusion rates and atmospheric backscatter rates. Inspection of Figures 4 through 7 and 9 of Reference 1, (also see Ref. 2) confirms that the loss cone distribution is indeed very sensitive to the diffusion rate. But the important measurable parameters are not necessarily **those** that simple intuition might lead one to believe useful for this purpose. For example, total flux in the center of the loss cone (or ratio of $\alpha \sim 0^\circ$ flux to 90° flux at low altitude) is nearly independent of diffusion rate, except in strong diffusion. The distribution near the center of the loss cone is most valuable for the information it provides about backscatter rates. Ideally the ratio of downgoing flux to upgoing flux at intermediate pitch angles in the loss cone would give directly the instantaneous value of the diffusion coefficient, a quantity that has not yet been found by any other method.

Unfortunately most of the loss cone data we have examined do not appear to be reliable. The data are very sparse, and of uncertain quality. It is likely that most of the data were contaminated by cosmic ray induced bremsstrahlung: Spjeldvik (Ref. 22) has noted similar difficulties. The only case we found in which bremsstrahlung contamination of the loss cone counting rates could be ruled out was the one reported in Figure 9 of Reference 2. The data for that case were collected during a time of intense magnetic activity ($K_p = 8-$);

so it is uncertain whether other processes could have affected the trapped electrons.

We have great hopes that the instrumental contamination problems may have been overcome in the most recent satellite experiments; and we are awaiting the new data. But, in view of the grave difficulties, we wish to suggest, in the following section, another method that might be used to **derive** diffusion coefficients.

2.3 LONGITUDINAL DRIFT AND THE FILLING OF THE LOSS CONE

An important effect that has been ignored in the preceding discussion is the variation of the size of the loss cone with geomagnetic longitude. The earth's magnetic field is only very roughly approximated by a simple dipole field. For most purposes the important deviations from the simple model can be accommodated in an off-center dipole field model (Ref. 23). The cutoff, α_c , then varies with azimuthal position. Figure 8 shows the 100 km altitude trace plotted against geomagnetic longitude for two L shells. The particle's azimuthal drift allows them to diffuse beyond $\alpha_{c-\max}$ and partially fill the so-called "quasi trapping" regions where the cutoff α_c is reduced. A diagonal line is sketched in Figure 8 to indicate how the "edge" of the distribution advances as the particles drift (in this sample, electrons drifting eastward).

If the diffusion coefficient is large enough, the diffusing particles can advance into the gap between $\alpha_{c-\max}$ and α_c as fast as α_c recedes. The maximum change in α_c with longitude ϕ is of the order

$$\frac{\partial \alpha_c}{\partial \phi} \sim .35/L^2 . \quad (29)$$

The mean α_c distance a particle can diffuse during a complete bounce period is given by Equation (13). The diffusion coefficient near α_c needed to keep the gap filled is therefore

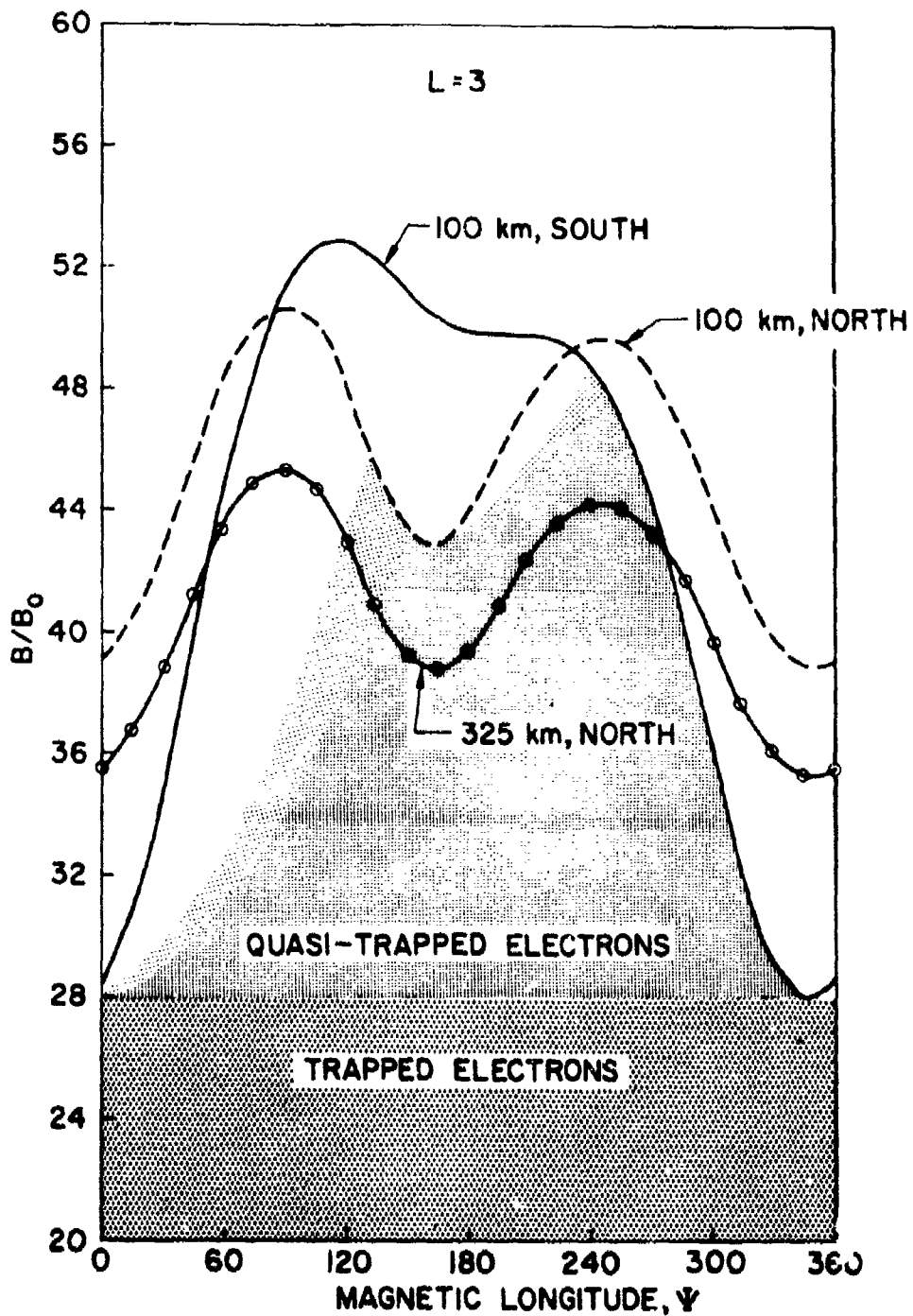


Figure 8. Variation of the edge of the loss cone with geomagnetic longitude. Of the two 100 km altitude traces, the smaller B value determines the limit of influence of the atmosphere.

$$\langle D_{\alpha_0 \alpha_0} \rangle \approx \frac{1}{2} \frac{(\Delta \alpha)^2}{\Delta t} \quad (30)$$

$$\approx \frac{1}{2} \frac{1}{\tau_B} \left(\frac{\partial \alpha}{\partial \psi} \right)^2 \approx \frac{1}{2} \left(\frac{\tau_B}{\tau_D} \right)^2$$

where τ_D is the drift period. Table II lists some values estimated for $\langle D_{\alpha_0 \alpha_0} \rangle$. Equation (30) however, refers only to the necessary diffusion coefficient that will allow a small number of particles to leak out of the trapping region at every longitude. As the diffusion coefficient is increased it will gradually approach a value that follows f to adjust continuously to the changing cutoff, with a nearly uniform leakage rate independent of longitude. This latter limiting value is much less than the strong diffusion limit, $\langle D \rangle \sim \frac{1}{\tau_B}$, but as much as 5 decades higher than the values of Table II.

Figures 9 and 10 show results of sample calculations using Equation (7) for the diffusion of electrons (with an assumed $\langle D_{\alpha_0 \alpha_0} \rangle =$ constant) with no allowance for backscatter. Similar results have appeared previously (Ref. 24). For low values of the diffusion coefficient, the tail of the distribution fills in nearly as $\exp(-\text{const } \frac{B}{B_0})$; the local cutoff, B_c/B_0 , is generally out of sight at the lower right of the figure. When the diffusion coefficient becomes large enough, in this case 10^{-5} sec^{-1} , the pitch angle distribution is similar at every longitude, except that the local cutoff determines the location of the shoulder of the distribution.

The filling and depletion of the quasi-trapping loss cone has been observed for trapped electrons and for trapped protons. Figure 11 shows some results of Imhof (Ref. 25) for a low altitude satellite whose east-west motion

TABLE II
 Minimum Pitch Angle Diffusion Coefficient That Allows
 Some Filling of the Loss Cone at All Longitudes

E (ev)	D_{lim} (electrons)	D_{lim} (protons)
10^3	$4.3^{-13}/L$	$1.9^{-11}/L$
10^4	$1.4^{-11}/L$	$5.9^{-10}/L$
10^5	$4.2^{-10}/L$	$1.9^{-8} /L$
10^6	$1.3^{-8} /L$	$5.9^{-7} /L$
10^7	$7.4^{-7} /L$	$1.9^{-5} /L$

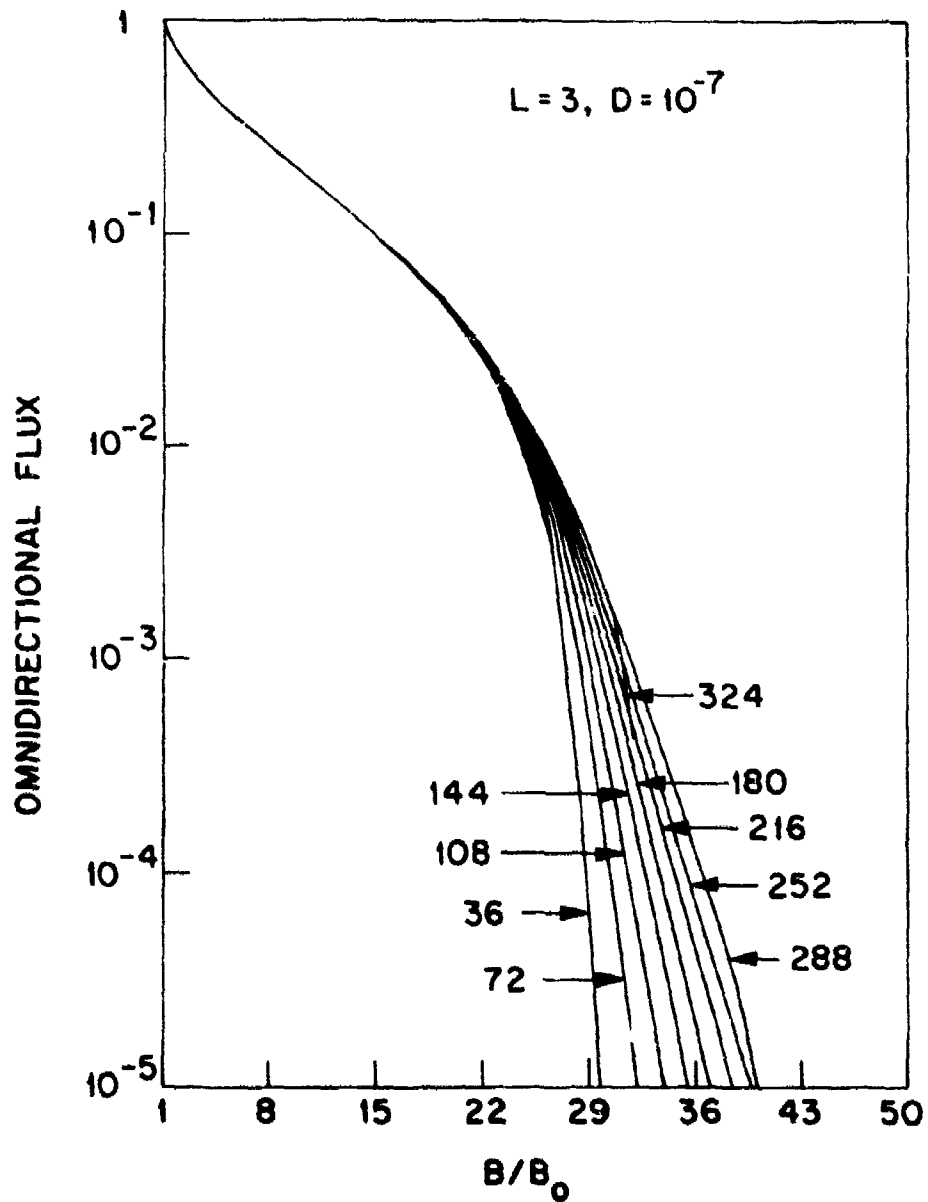


Figure 9. Solutions of the averaged diffusion equation for various longitudes (relative to the SA anomaly, denoted by the label on each curve). This case is for a small diffusion coefficient so the bottom edge of the particles remains nearly fixed at one B value.

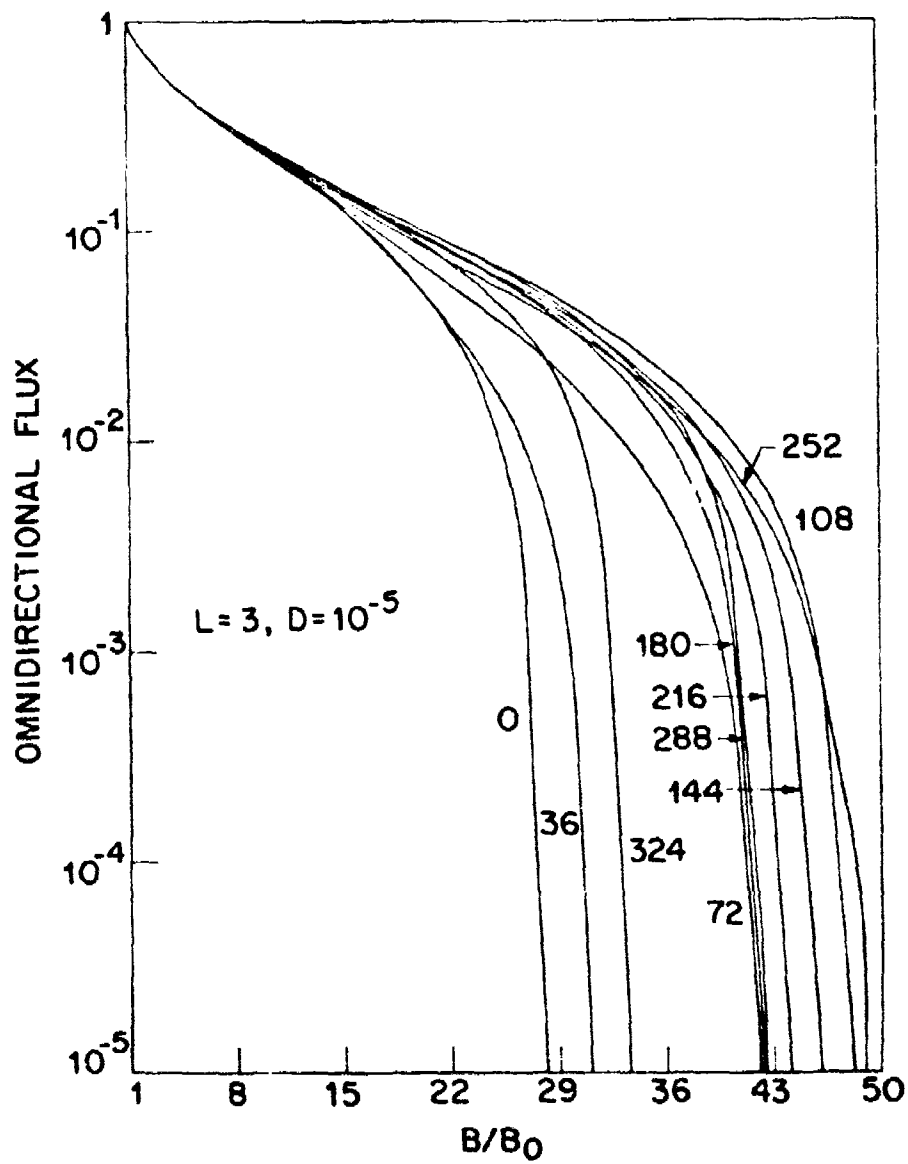


Figure 10. Solution of the averaged diffusion equation for various longitudes (relative to the SA anomaly, denoted by the label on each curve). This case is for a diffusion coefficient large enough that the edge of the distribution follows a constant altitude trace.

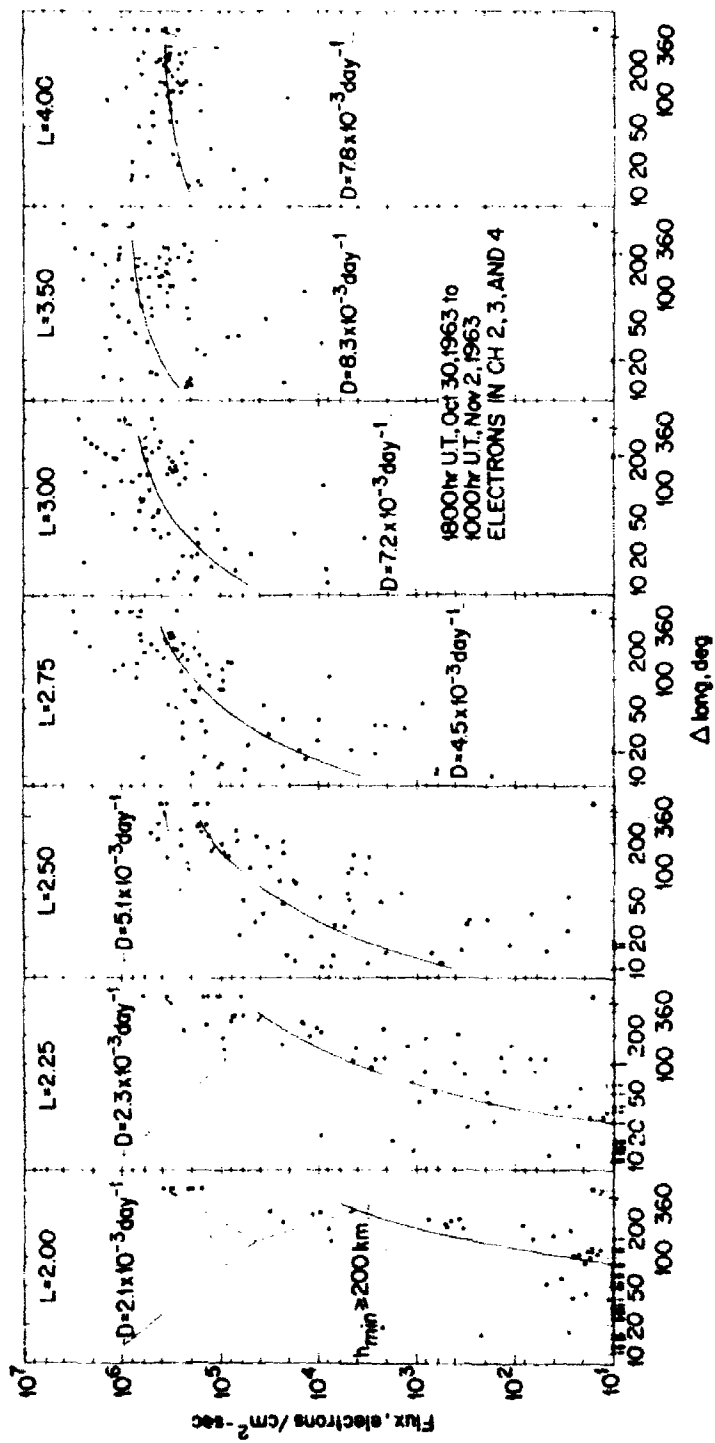


Figure 11. Filling of the "quasi trapping" electron loss cone observed by a satellite at constant altitude. The solid curves are results of a diffusion calculation by Imhof (Ref. 25).

was adequate to exhibit the effect. We have done a simple calculation using Equation 8 with the loss term multiplied by 1 minus a "reflection coefficient", R. A plausible fit to the data is shown in Figure 12. The backscatter of electrons does tend to mask the eastward drift effect; but since the quasi trapping phenomenon affects mainly particles mirroring above the atmosphere, there is hope that the effect may be of value in determining diffusion coefficients.

How then might the atmospheric backscatter be treated simultaneously with longitudinal drift, while avoiding the rigors of a diffusion equation with four independent variables, longitude, latitude pitch angle, and energy? Again, it should be feasible to take advantage of the fact that the various phenomena have quite different time scales. If the cutoff boundary, α_c , does not move too rapidly, then the steady state equation, 22, should give valid results for the atmospheric backscatter. The averaged diffusion equation should then be adequate to treat the major part of the trapped distribution, plus the quasi trapping region. This first-approximation could be used as a starting point for several iterations of Equation 22 to obtain detailed solutions for all longitudes. We expect to test this method soon to find out whether it is practical, and indeed results in great savings of computer time.

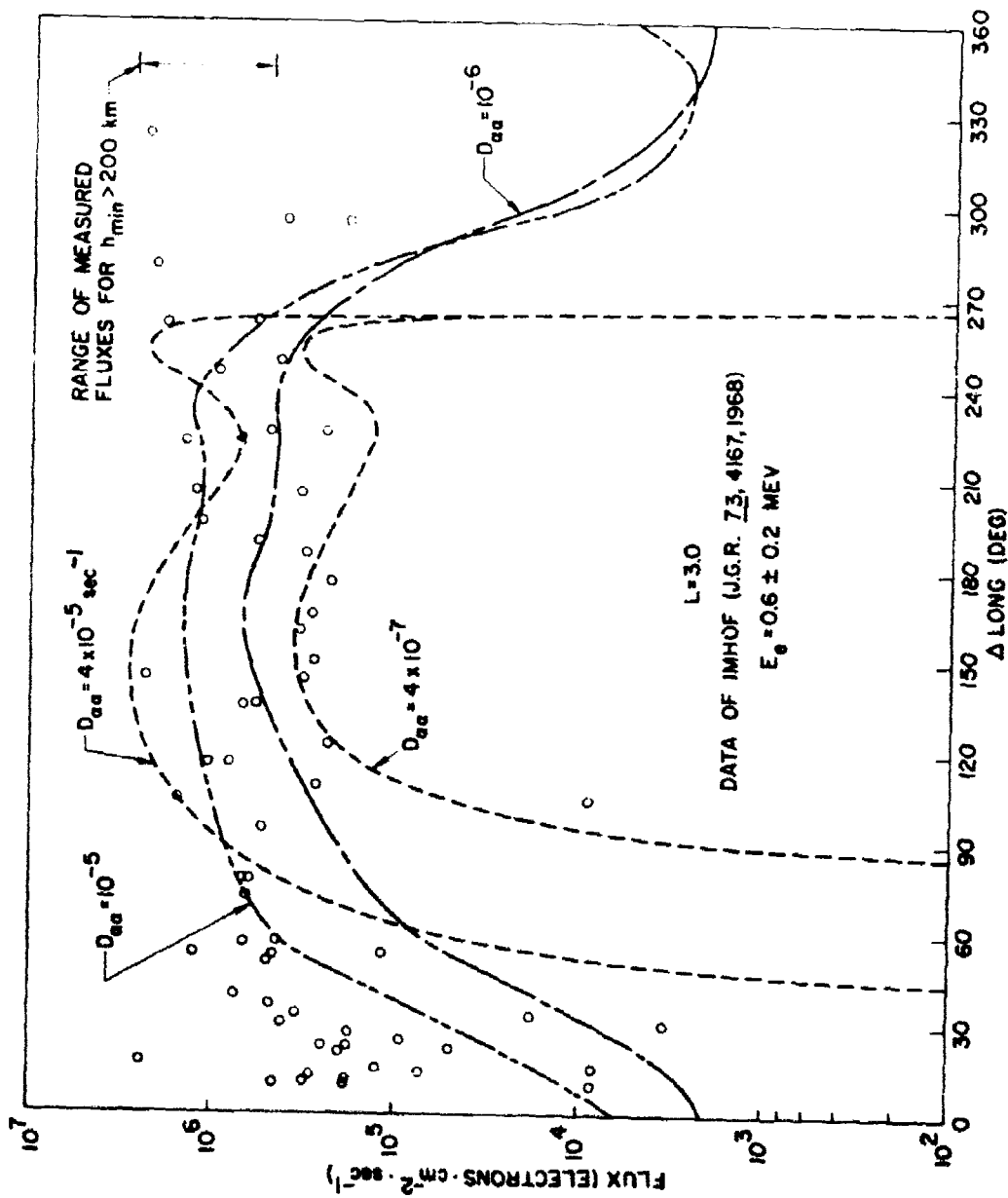


Figure 12. The data of Figure 11 with several solutions to the diffusion equation superimposed. The dashed curves are for no atmospheric backscatter. The other results include a crude approximation to the backscatter, based on the results of the preceding sections.

Section 3

OBSERVATIONS OF SCINTILLATIONS IN MID LATITUDES

Ionospheric scintillations have been observed at all latitudes, though research on their effects has been concentrated in the equatorial and auroral regions. Recently, there has perhaps been a tendency to emphasize the equatorial regions because those regions are most predictable. However, it might be argued that the mid- and high-latitude ionospheric disturbances more closely approximate the effects induced by high-altitude nuclear explosions. We have therefore directed our efforts at a search for correlations in mid latitudes between scintillation activity and energetic particle precipitation. The mechanisms underlying such correlations are poorly understood, so our work has been mainly explorational.

A receiver station in the WIDEBAND program was operated at Stanford, California from May 25, 1976 to mid-September 1976. The purpose of the Stanford station was mainly to check out procedures, and verify the operation of the system. Operation of the Stanford station was therefore somewhat irregular, covering only about three days of each week. Nonetheless, an appreciable amount of data was acquired showing high degrees of scintillation activity (Ref. 26). E. J. Fremouw of SRI graciously allowed us access to the data, and with the assistance of S. Matthews (also of SRI), we were also to construct our own summaries of the data.

Table III lists the times of the observations and the estimated levels of activity. The scintillation activity levels from A-quiet - to B-intense - pertain to the combined amplitude displacement, S_V , and the phase duration, α_p , of the VHF signals. Our assessments were made independently, and may differ

slightly from those arrived at by the SRI group (Ref. 26). The levels A to B correspond roughly to the designations very quiet and very active, respectively, in Ref. 26, though we have tried to break down the individual pass records by the elevation angles. Some low elevation intense scintillations should be discounted because they reflect merely a large total electron content over a long path.

We have also listed available data on K_p indices, solar sector crossings, and the character of the total electron content (TEC) as observed by the WIDEBAND receiver.

The first thing to be noticed is that moderate-to-intense activity in mid latitudes can occur at all times of the day, and with no obvious pattern. (The early morning passes are labelled with a N because they started in the north, and the afternoon passes starting in the south are labelled with a S.) There may be a correlation between the north-to-south gradients of the ionospheric electron content, but the predictive value of this correlation is not clear. The absolute levels of the total electron content have not yet been established, either by comparison with (very limited) ionospheric sounder data, or by absolute calibration of the WIDEBAND data (Ref. 26). If the correlation is established and confirmed, it is not clear how it would be exploited to obtain local predictions of scintillation levels. Perhaps new ionospheric sounding stations might be established at critical sites. In any event the electron density and temperature are the most likely ionospheric parameters that might reflect the deposition of energy from the trapped particle belts. The three-fold correlation of scintillation activity, ionospheric conditions, and precipitation of trapped electrons is a topic which calls for an extended investigation.





TABLE III

SCINTILLATION LEVELS AT STANFORD

Scintillation level:

- A: Quiet $S_V < .2, \alpha\phi < .3$
 B: Quiet, trace of scintillations $S_V < .4, \alpha\phi < .7$
 C: Weak scintillations $S_V < .5, \alpha\phi < 1.2$
 D: Moderate scintillations
 E: Intense scintillations

Total electron content (TEC):

- Uniform  Deep minimum
 Rise  Minor peaks superimposed on trend
 Gentle rise  Sharp drop
 Minimum  Scatter










Date	Time (UT)	Start	Scintillation Level/Elevation (deg.)	TEC	$\sum K_p$	INF
5/25/76	0611	0624	N E/3-13 D/13 C/13-8 D-E/8		17	T -
	0708	0809	N A-B/-80-			
	1802	1813	S A/-39-			
5/26	1946	1957	S A/-33-			
	0641	0704	N D/6-16 C/16-25 A/25-30-22 C/22-16 A/16-7		12+	T T
	0834	0849	N C-D/6-14 B/14-35 C-D/35-39-36 B/36-22 C/22-3			
5/27	1838	1854	S C/7-15 A/15-77-20 C/20-6			
	0729	0745	N C/7-21 A/21-63-6 C/6-3		10+	T -
	0914	0927	N C-D/6-19 B/19-2			T T

Table III, Page 2

Date	Time (UT)	Start	Scintillation Level/Elevation (deg.)	TEC	ΣK_p	IMF
5/28/76	0626	N	B/5-7 A/17-18 C/18-10 B/10-3	/	23-	T T
	0809	N	A/16-61-60 C/60-36 B/36-4	/	26-	T T
5/29					25-	T T
5/30					17+	T T
5/31					13-	T T
6/01	1910	S	A/16-62-10	~	14	T *
6/02	0759	N	A/7-73 B/73-74-12 D/12-3	/		
	1804	S	A 7-41-11 B/11-3	~		
	1949	S	B/6-12 A/12-30-3	~		
6/03	0655	N	A/6-30-33-32 D/32-3	? SC	17+	TA T
	0839	N	A/10-36-3	?	25	A A
6/04	0734	N	A/-71-3	/	27	A A
6/05					16+	A A
6/06					22-	A T
6/07					17	A T
6/08					17+	A -
6/09	0724	N	B/9 30 A/30-58-40 B/40-15 D/15-3	/		
	0910	N	A/-21-16 B/16-2	/		
	1731	S	A/-22-20 B/20-14 C/14-4	~		
	1913	S	C/7-16 A/16-23 B/23-34 A/34-48 B/48-65-52 A/52-25 B/25-	~		
6/10	0804	N	B/6-50 A/50-68-18 B/18-5	/	11	T *

Table III, Page 3

Date	Time (UT)	Start	Scintillation Level/Elevation (deg.)	TEC	ΣK_p	IMF
6/11/76	0700	N	A	SC	30	A A
	0844	N	?A/33-3	✓		
6/12	1848	S	A/6-86-	✓	14+	A A
6/13	1904	S	A/6-86-	✓	9-	A -
6/14					5	T T
6/15					6+	T A
6/16					10	T T
6/17	0650	N	C/5- 8 A/18-29-28 B/28-8 D/8-2	✓	22	A A
	0729	N	E/6-18 B/18-63 C/63-64-5	✓		
6/18	0809	N	A/7-63-13 B/13-4	✓	27+	T *
6/19					8+	A T
6/20					11	T A
6/21					6+	A A
6/22					6-	T A*
6/23	0759	N	D/6-13 C/13-56 A/56-75 B/75-10 C/10-5	✓	9-	T T
	1806	S	A/13-40-10 B-C/10-2	✓		
	1949	S	B/6-9 D-E/9-14 B/14-20 A/20-30-	✓		
6/24	0655	N	B/33-28 C/28-13 E/13-3	✓	19+	T T
	0834	S	A/6-82-10 B/10-3	✓		
	1843	S	A/6-86-6	✓		
6/25	0734	N	A/6-70-60 B/60-40 A/40-5	✓	26-	T T
6/26					13-	T T
6/27					14-	T T

Table III, Page 4













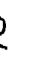
Date	Time (UT)	Start	Scintillation Level/Elevation (deg.)	TEC	ΣK_p	IMF
6/28/76					11+	AT A
6/29					10	T T
6/30	0910	N	B/6-19 C/19-22-17 A/17-6 B/6-2		28+	A A
	1732	S	B/6-22-5			
	1914	N	A/-58-			
7/1	0805	N	A/-69-		25-	AT T
7/2	0700	N	C/6-36 A/36-25 C/25-20 E/20-13		18-	A A
			C/13- E/3-2			
	0845	N	C/7-24 B/24-34-33 C/33-3			
7/2	1849	S	A/-88-			
7/3					20+	TA T*
7/4					22+	AT A
7/5					12+	A A
7/6					12	A A
7/7	0651	N	A/17-22 D-E/22-30-29 B-C/29-17		16+	A A
	0834	N	B/6-26 C/26-41-3			
	1839	S	C/6-8 A/18-75-17 E/17-9 C/9-5			
7/8	0730	N	C/7-24 A/24-64-43 B/43-7		21+	TA A*
7/9	0810	N	B/7-42 A/42-64-37 C/37-6		19-	T T
7/10					12+	A A
7/11					8+	A A
7/12					11	T T
7/13					9-	T A

Table III, Page 5

Date	Time (UT)	Start	Scintillation Level/Elevation (deg.)	TEC	ΣK_p	IMF
7/14/76	0800	N	C/8-12 A/12-76-61 D/61-45 B/45-7	~	13-	AT T*
	1805	S	A/8-39-10 C/10-	~		
	1950	S	A-B/7-30-24 C/24-16 A/16-4	~	23-	A TA
7/15	0657	S	D/7-26 B/26-33-32 C/32-8 D/8-4	~		
	0840	N	B/-36 A/36-38-15 B/15-4	~	25-	AT AT
7/16	0742	N	A/-68-9 B-D/9-3	~	11-	T A
7/17					12-	A A
7/18					11	T A*
7/19					8	T A
7/20					6	A T*
7/21	0724	N	C/8-28 A/28-58-36 B/36-6	~		
	1731	S	C/7-9 B/9-20 C/20-21 A/21-18 B/18-11 E/11-6	~		
	1914	S	A/-59-	~	9	T T
7/22	08	N	E/7-10 B/10-29 A/29-71-67 B/67-8	~	10	A A
7/23	0700	N	C/7-36-35 B/35-15 D-E/15-5 C/5-4	~		
	0845	N	B/8-35-	~	8+	A A
7/24					17+	A A
7/25					7	A A
7/26					14+	A A
7/27					25	A A
7/28	0650	N	B/10-15 A/15-49-21 C/21-12 E/12-6	~		
	0834	N	C/10-12 A/12-42-30 C/30-12 E/12-9 C/9-6	~		

Table III, Page 6

Date	Time	(UT)	Start	Scintillation Level/Elevation (deg.)	TEC	ΣK_p	IMF
7/29/76	0720	0745	N	A/10-63-27 B/27-6	✓	26-	TA A*
	0914	0926	N	B/11-21-6	✓	26+	T T
7/30	0810	0824	N	A/10-65-6	✓	15+	A A
7/31						15+	A A
8/01						14+	T T
8/02						17+	A A
8/03						10+	A A
8/04	0759	0814	N	C/10-12 A-B/12-77-5	✓		
			N	A/10-33-6	✓	11	A A
8/05	0656	0710	N	B/9-33-6	✓		
	0840	0854	N	A/10-39-5	✓		
8/06	0735	0750	N	E/10-12 C/13-17 A/17-69-53 C/53-32 A/32-17 E/17-6	✓	11	T A
8/07						11-	AT T*
8/08						9	TA TA
8/09						18	TA -
8/10						16	TA TA
8/11	0725	0740	N	B/10-48 A/48-58-36 B/36-6	✓	10	A A
	1732	1743	S	C/10-19 A/19-21 C/21-18 A/18-7	✓		
	1914	1922	S	B-D/10-17 A/17-60-12 B-D/12-6	✓		
8/12	0805	0819	N	A/11-72-56 B-C/56-9 D/19-7	✓	7-	T T
8/13	0701	0714	N	C/11-18 A/18-36-7	✓	6-	T T
	0845	0859	N	C/11-21 B/21-36-7	✓		

Table III, Page 7











Date	Time (UT)	Start	Scintillation Level/Elevation (deg.)	TEC	ΣK_p	IMF
8/14/76					8+	A A
8/15					4+	A A
8/16					13	A A
8/17					9	T T
8/18	0651	N	C/9-23 B/23-30 A/30-16 C/16-6		9	T T
	0835	N	C/10-18 A/18-42-6			
	1840	S	A/10-73-15 B-C/15-10			
8/19	0730	N	B/10-60 C/60-63 D-E/63-10 C/10-5		13-	T T
	0915	N	C/9-11 D/11-19 C/19-22-21 D-E/21-13 B-C/13-5			
8/20	0811	N	B/14-66-48 C/48-24 B/24-7		11+	A A
8/21					15	A A
8/22					10+	TA T*
8/23					31-	A A
8/24					29	A A
8/25	0800	N	A/10-62 B/62-78-66 E/66-44 D/44-32 C/32-14 B/14-6		30+	A A
	1807	S	B/16-36 A/36-39-11			
8/26	0841	N	A/15-39-37 B/37-11		26	A A
8/27	0735	N	A/16-68-12		20+	A A
8/28					19-	A A
8/29					14	A A
8/30					12+	A *
8/31					11	A A

Table III, Page 8

Date	Time (UT)	Start	Scintillation Level/Elevation (deg.)	TEC	ΣK_p	IMF
9/01/76	0724	N	B/10-49 A/49-52-51 B-C/51-13 A/13-5	—	—	AT A
	0909	N	C/9-19 B/19-23 A/23-12 C/12-10	—	—	
	1732	S	A-B/-22-	∩		
	1914	S	A/-61-	∩		
9/02	0804	N	A/11-72-64 B/64-54 A/54-16 B/16-8	∩		A A
9/03	0700	N	A/-36-	∩	SC	A A
	0844	N	A/10-36-7 C/7-5	∩		
9/04						A
9/05						A T
9/06						A T
9/07						A T
9/08	0650	N	B/9-19 C-D/19-28 B/28-29 A/29-5	∩	SC	T A
	0834	N	B/10-41 A/41-42-6	∩		
	1839	S	A/16-73-24 B/24-12	∩	SC	
9/09	0729	N	B/10-30 A/30-62-6	∩		A
	0914	N	C/9-21 A/21-6	∩		
9/10	0810	N	A-B/-66-	∩		A

We had initially hoped to find correlations between the global indicators -- such as K_p -- and the mid latitude scintillations. Table III lists the K_p index and the character of the interplanetary magnetic field. Only the sum, ΣK_p , of the 8 three-hour K_p 's is shown because activity was very low during the period. Values less than 20 for ΣK_p indicate quiet days, and only values greater than 30 should be considered significant. The interplanetary field during a half-day is characterized by the direction of the field near the earth; T stands for toward and A for away. An inspection of the most readily available indicators, K_p and the solar sector structure reveals no such correlations. Analysis of a larger body of data might reveal low-level correlations, but such correlations would be of little value to an operational system.

We are just now beginning to receive new data on electron precipitation rates, though we have not found any that are directly applicable to the period in question.

It should be kept in mind that the WIDEBAND experiments were initiated at the bottom of the solar minimum. Magnetospheric and ionospheric activity have been very low, but are expected to rise rapidly through the next several years. That the anticipated correlations failed to materialize is not surprising because no great solar events occurred during the period while the Stanford receiving station was in operation. It has, however, been demonstrated that high levels of scintillation activity do occur frequently in mid-latitude regions; frequently enough that the study of mid-latitude scintillations is a worthy endeavor.

Section 4

COUPLING OF IONOSPHERE AND MAGNETOSPHERE

4.1 ANOMALOUS PHENOMENA AFFECTING COUPLING

Many processes of importance to defense problems are sensitive to the coupling of the ionosphere and the magnetosphere. This coupling is severely altered when plasma instabilities form anomalous resistivity, or electric double layers, in the upper ionosphere that impede the flow of thermal plasma currents along the magnetic field. The resulting electric fields, with components along the magnetic field, preclude the neutralization of large-scale electric fields produced in the magnetosphere by high altitude nuclear explosions. Such obstructions thereby affect (i) the growth rate of plasma irregularities all along the magnetic tubes containing the debris and "atmospheric-heave" plasma, (ii) the dynamical motion of the debris tube, hence the eventual distributions of the debris and the trapped electrons, and (iii) the energy deposition in the upper atmosphere and the attendant interference with radio-wave propagation and optical/IR systems. Furthermore, the obstructions affect natural processes in the auroral zones, which are examined to understand phenomena produced by high-altitude nuclear explosions.

Anomalous resistivity and electric double layers are due to plasma instabilities that inhibit the mobility of thermal electrons along the magnetic field. Although much theoretical effort has been devoted to the investigation of the pertinent instabilities (see Perkins, Ref. 27; Kindel and Kennel, Ref. 28; Block, Refs. 29,30; Carlqvist and Bostrom, Ref. 31; Papadopoulos and Coffey, Ref. 32; Swift, Ref. 33; and Swift et al., Ref. 34), many

uncertainties remain (see Papadopoulos, Ref. 35, for a recent review of this subject).

Much experimental evidence, however, is now available on the electric fields resulting from the instabilities. The fields were inferred initially from observations of "monoenergetic" electrons in the auroral zones (see, e.g., Hoffman and Evans, Ref. 36; Evans, et al., Ref. 37; Paschman, et al., Ref. 38; Machlum and Moeystue, Ref. 39; Arnoldy, et al., Ref. 40; and Basqued, et al., Ref. 41). More recently they have been inferred from observations of energetic ions generally moving along the magnetic field away from the upper ionosphere (see Hultquist et al., Ref. 42; Reme and Bosqued, Ref. 43; McIlwain, Ref. 6; and Shelley et al., Ref. 5). In addition, the electric fields have been inferred from shaped-charge barium releases (Wescott et al., Ref. 44; Haerendel et al., Ref. 45) and direct measurements (Mozer et al., Ref. 7; Mozer, Ref. 46). The data indicate that the electric potentials extend to 6 kV and higher, and are located within a few thousand kilometers from the earth (Evans, Ref. 47; Lampton, Ref. 48; Winiecki, Ref. 49; Arnoldy, Ref. 50; and Haerendel et al., Ref. 45). Moreover, they occur in regions where field-aligned currents are high and where the auroral-electron precipitation is intense.

A model of the electric potentials in a cross section normal to an auroral arc, which accounts for most of the observations (Swift, Ref. 33), is shown in Figure 13. Here, the magnetic field lines are taken to be vertical. The equipotentials are symmetrical about the magnetic field line at the center of the arc. At any altitude, the potential is a minimum at the center and increases monotonically toward the sides; hence the electric field component

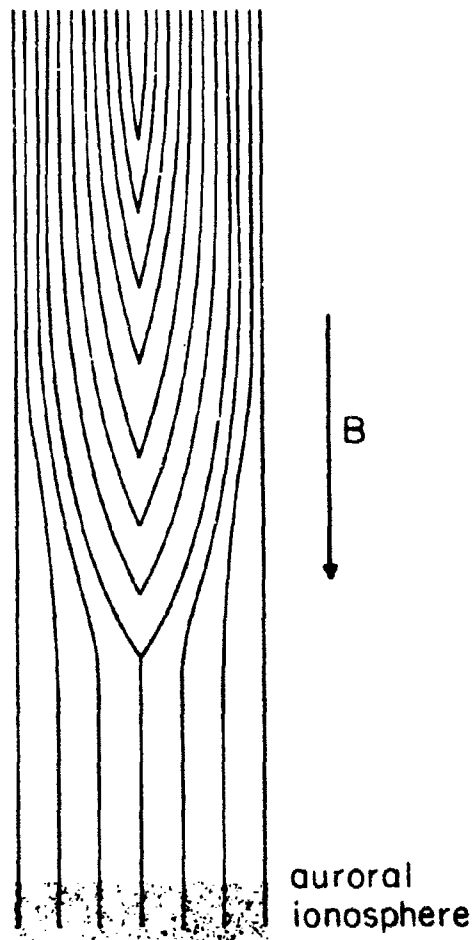


Figure 13. Equipotential model for electric fields above auroral ionosphere. Lines represent equipotential surfaces; the magnetic field is taken to be vertical.

normal to the magnetic field is directed toward the center of the arc. Toward higher altitudes, along magnetic field lines, the electric potentials decrease in magnitude; thus, the electric-field component along the magnetic field is directed upward. Such a field component tends to accelerate electrons downward and ions upward. Note that the electric field normal to the arc increases toward higher altitudes. No data are available on the closure of the potential contours above the top of the diagram. It seems plausible, however, that the contours near the sides continue upward, parallel to the magnetic field, and close in the conjugate region, maintaining approximate symmetry about the geomagnetic equator.

The work described below provides additional information on the properties of this electric field and the conditions under which it develops. The properties of the field are inferred from recent satellite measurements of electron and ion distributions. In the following section (4.2), equations are developed which describe the effects of an electrostatic field along the magnetic field on charged particle fluxes. In section 4.3 the observed fluxes are interpreted in terms of the parameters of the potential model described above.

4.2 EFFECTS OF ELECTRIC POTENTIALS AND MAGNETIC MIRRORS ON CHARGED PARTICLE FLUXES

Transformations of particle fluxes will be described with reference to the diagram shown in Figure 14, which depicts a converging magnetic field and an electrostatic potential. Altitudes and magnetic field intensities are denoted by z and B , and electric potentials by ϕ . The subscripts s

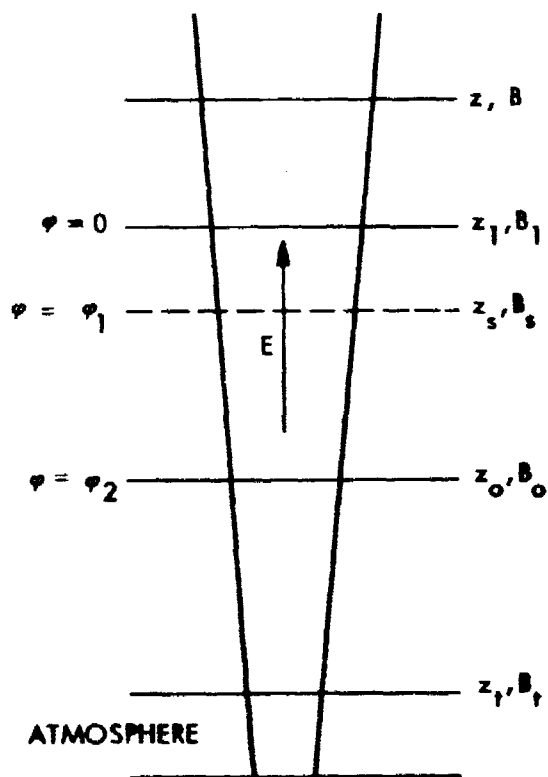


Figure 14. The field geometry used in calculations of effects of electric fields. The oblique solid lines represent magnetic field lines. The horizontal lines represent equipotential surfaces; the satellite is on the dashed horizontal line at z_s .

denotes the parameters at the location of the satellite. The electric field E , which is directed upward, extends from z_0 , where the potential is ϕ_2 , to z_1 . The potential at the satellite is ϕ_1 . The subscript t denotes quantities at the "top" of the atmosphere, where particle collisions become appreciable.

The particle data which will be described in the following section were obtained before and after the electric fields were established. We will, therefore, relate the flux, $j^{(E)}$, when the field was present to the flux, j , when the field was absent.

In the absence of E , the incident flux, at the top of the atmosphere is equal to the flux at z_s , i.e.

$$j(\alpha_t, B_t, w_t) = j(\alpha_s, B_s, w_s) \quad (31)$$

$$\text{where the kinetic energy is } w_t = w_s \quad (32)$$

$$\text{and } \frac{\sin^2 \alpha_t}{B_t} = \frac{\sin^2 \alpha_s}{B_s} \quad (33)$$

The edge of the loss cone, $\alpha_s = \alpha_{sc}$, is obtained from (33) for $\alpha_t = \pi/2$; i.e.,

$$\alpha_{sc} = \sin^{-1}(B_s/B_t)^{\frac{1}{2}} \quad (34)$$

If the backscattered flux at z_t is denoted by $j_B(\alpha_t, B_t, w_{Bt})$, $\pi/2 \leq \alpha_t \leq \pi$, then at the satellite,

$$j(\alpha_s, B_s, w_s) = j_B(\alpha_t, B_t, w_{Bt}) \quad (35)$$

where again α_s and α_t are related through (33) in the "loss cone,"

$$\pi \geq \alpha_s \geq \pi - \alpha_{sc}, \text{ and } w_s = w_{Bt}.$$

When an electric field is applied along the magnetic field direction, j itself is no longer an invariant, as in equation (31). Rather, the proper invariant of the motion is f , the phase space distribution function (the distribution function used in Section 2). The two functions are related by the (non-relativistic) formula,

$$j = 2\pi w f \quad (36)$$

It follows that the flux at z_1 -- which equals the undisturbed flux at z_s for $\alpha_1 \leq \sin^{-1}(B_1/B_s)^{1/2}$ -- is transformed to

$$j^{(E)}(\alpha'_s, B_s, w'_s) = \frac{w'_s}{w_s} j(\alpha_s, B_s, w_s) \quad (37)$$

$$\text{where } w'_s = w_s + e\phi_1 \quad (38)$$

$$\text{and } \sin^2 \alpha'_s = \frac{w_s}{w'_s} \sin^2 \alpha_s \quad (39)$$

$$\text{for } 0 \leq \alpha_s \leq \pi/2 \quad (40)$$

(Pitch-angle diffusion has been ignored here. However, it will eventually be necessary to extend the analysis to cases where the effects of diffusion are of magnitudes comparable to electric field effects. If energy diffusion is negligible, the right-hand side of equation (3) retains its form, but with the space-like variable B/B_0 everywhere replaced by the transformed variable $\frac{B(w-e\phi)}{B_0(w)}$; the phase space distribution function must be a function of $w-e\phi$ rather than w . It is not likely that energy diffusion can be ignored if the electric field is set up by plasma turbulence of electrostatic-type waves.) Although the primary flux for $\alpha'_s > \sin^{-1}(\frac{w_s}{w'_s})^{1/2}$ is unknown, the potential ϕ_1 will reflect upgoing electrons observed at z_s with energies w'_s and pitch angles α'_s such that,

$$w'_s \left[\cos^2 \alpha'_s + \frac{B_s - B_1}{B_s} \sin^2 \alpha'_s \right] < e\varphi_1. \quad (41)$$

Hence, in the pitch-angle range

$$\sin^{-1} \left(\frac{w'_s - e\varphi_1}{w'_s} \cdot \frac{B_s}{B_1} \right)^{\frac{1}{2}} \leq \alpha'_s \leq \pi/2 \quad (42)$$

$$\text{with } e\varphi_1 \leq w'_s \leq e\varphi_1 \left(\frac{B_s}{B_s - B_1} \right) \quad (43)$$

as well as for $0 < \alpha'_s \leq \pi/2$ with $w'_s \leq e\varphi_1$, the downgoing flux at z_s is equal to the upgoing flux, i.e.

$$j^{(D)}(\alpha'_s, B_s, w'_s) = j^{(U)}(\pi - \alpha'_s, B_s, w'_s). \quad (44)$$

At the top of the atmosphere, z_t , through the potential φ_b , the electron flux becomes

$$j^{(E)}(\alpha_t, B_t, w_t) = \frac{w_t}{w'_s} j^{(E)}(\alpha'_s, B_s, w'_s) \quad (45)$$

$$\text{where } w_t = w'_s + e\varphi_b, \quad \varphi_b = \varphi_2 - \varphi_1 \quad (46)$$

$$\text{and } \sin^2 \alpha_t = \frac{w'_s}{w'_s + e\varphi_b} \cdot \frac{B_t}{B_s} \sin^2 \alpha'_s. \quad (47)$$

Hence, the edge of the loss cone of the observed flux at z_s is now energy dependent and has increased from the value given in Equation (34) to

$$\alpha'_{sc} = \sin^{-1} \left(\frac{w'_s + e\varphi_b}{w'_s} \cdot \frac{B_s}{B_t} \right)^{\frac{1}{2}}. \quad (48)$$

The pitch-angle distributions of the electrons can therefore be used to determine φ_b .

Note also that the electron flux reflected by the potential above the satellite (Eq. 44) is also transformed to the top of the atmosphere according to Eqs. (45)-(47), and those electrons with

$$\alpha'_s \geq \alpha'_{sc} \quad (49)$$

are reflected back toward the satellite by the magnetic field. Since Eqs. (49) and (42) are satisfied by electrons in the energy range

$$\frac{\exp_1 + \exp_b \frac{B_1}{B_t}}{(1 - B_1/B_t)} \leq w'_s \leq \exp_1 \left(\frac{1}{1 - B_1/B_s} \right), \quad (50)$$

such electrons will be trapped between the magnetic mirror at the top of the atmosphere (z_t) and the upper boundary (z_1) of the electric potential. The electron data discussed in the next section indicates that electrons are indeed trapped in this manner.

The AURORA code was used to compute the flux of electrons backscattered from the atmosphere. An iteration procedure was used to determine the appropriate incident flux which included not only that given by Eq. (45) but also the backscattered electrons which were reflected back to the atmosphere by the electric field. The latter flux, $j_R^{(E)}$, was determined from the equations

$$j_R^{(E)}(\alpha_t, B_t, w) = j_B^{(E)}(\pi - \alpha_t, B_t, w) \quad (51)$$

$$\text{where } 0 \leq \alpha_t \leq \pi/2 \text{ for } w \leq \exp_2 \quad (52)$$

$$\text{and } \sin^{-1} \left(\frac{w - \exp_2}{w} \cdot \frac{B_t}{B_1} \right)^{1/2} \leq \alpha_t \leq \pi/2 \text{ for } \exp_2 \leq w \leq \exp_2 \left(\frac{B_t}{B_t - B_1} \right) \quad (53)$$

Here $j_B^{(E)}$ is the backscattered flux.

The backscattered flux which reaches the satellite is

$$j_B^{(E)}(\alpha'_s, B_s, w - \epsilon p_b) = \frac{w - \epsilon p_b}{w} j_B^{(E)}(\alpha_t, B_t, w) \quad (54)$$

$$\text{where } \sin^2 \alpha'_s = \frac{w}{w - \epsilon p_b} \cdot \frac{B_s}{B_t} \sin^2 \alpha_t \quad (55)$$

$$w > \epsilon p_b .$$

4.3 ELECTRIC FIELDS INFERRED FROM SATELLITE DATA

4.3.1 Satellite Measurements

Exceptionally valuable data on particle distributions in the magnetosphere are being obtained with the satellite 1976-65B, a high-altitude polar orbiting satellite that has been launched recently. Drs. E.G. Shelley, R.D. Sharp, and R.G. Johnson of LMSC are the principal investigators of a major experiment on-board which measures the energy and angular distributions of ions in the energy range 0.5 to 16 keV and electrons in the range 70 eV- 24 keV. The ions are detected with three mass spectrometers which sample the mass-per-unit charge (m/q) distribution, in the m/q range 1-30, once per second. Since particle fluxes change rapidly in space and time at high latitudes, it is important to emphasize the time periods over which the energy and pitch-angle ranges are sampled. The energy-per-unit charge range 0.5 to 16 keV is covered by each spectrometer in 12 steps (0.5, 0.68, 0.94, 1.28, 1.76, 2.4, 3.3, 4.5, 6.2, 8.5, 11.6 and 16.0 keV). At any particular time, the energy settings of the detectors are at different values. They are cycled through 4 values every 64 seconds, remaining on each step for 16 seconds. Thus, a 12-point energy spectrum is acquired from the 3 spectrometers every 64 seconds.

The pitch-angles of the particles are determined by correlating the view directions of the detectors, which are perpendicular to the spin axis of the satellite, with the direction of the magnetic field. The satellite is spinning at 3 RPM with its spin axis perpendicular to the orbital plane. Thus, essentially the entire pitch-angle range is sampled by each detector every 10 seconds.

The electrons were detected by four spectrometers, designated CME A, CME B, CME C, and CME D. These spectrometer channels detected electrons principally in the ranges .074-.238 keV, .352-1.13 keV, 1.58-5.04 keV, and 7.3-23.5 keV, respectively.

Data from the first few orbits revealed several events of H^+ and O^+ ions streaming upward along the magnetic field in the auroral and polar regions, even during times of magnetic quiet. In the following section, we offer an interpretation of the data obtained on two of these events which were reported recently by Shelley et al. (Ref. 5). We also analyze an additional event for which we utilize the electron data as well as the ion data to interpret the results.

4.3.2 Interpretation of Data

In the two examples of the satellite data reported by Shelley et al. (Ref. 5), approximately equal fluxes of O^+ and H^+ ions (about $10^8/cm^2 \cdot sec \cdot sr \cdot keV$ at 1.28 keV) were observed simultaneously. (The detector settings were at 0.94 and 1.28 keV at the time of the measurements). Moreover, the pitch angle distributions of

both ions were nearly identical. They were sharply peaked along the field with a half-width-at-half-height of roughly 15° . Both events were observed at high magnetic latitudes ($\geq 69^\circ$); one was observed at a local time of about 14.5 hr at an altitude of about 7680 km, the other was observed at a local time of about 21hr at an altitude of about 5450 km.

These data indicate that the accelerating potentials below the satellite were about 1 kV. From the altitudes of the observations, we note that the electric field intensities must have been higher than about 1000V/6000 km or 0.2 mV/m. In such a field ambient H^+ and O^+ would be accelerated to 1 keV in about 22 sec and 90 sec, respectively. Now, if we assume steady-state conditions on a time scale of 90 sec, the observed ion flux, should, as discussed in Section 4.2, be a factor w_i/w_{th} higher than the flux of ambient, ionospheric ions at the base of the acceleration region. Here, $w_{th} \approx 0.1$ eV (the ion thermal energy in the ionosphere), and $w_i = w_{th} + 1$ keV. Moreover, the pitch angles of the energetic ions, α_i , should be related to the pitch angles of the thermal ions, α_{th} , by the equation

$$\sin^2 \alpha_i = \frac{w_{th}}{w_i} \frac{B_s}{B_o} \sin^2 \alpha_{th} \quad (56)$$

where B_s/B_o is the ratio of the magnetic-field intensity at the satellite to that at the base of the acceleration region. According to this equation the pitch-angle distribution of the ions should have been even more sharply peaked along the field than indicated by the data. Such a broadening of the distribution could have been due to scattering of the ions by the waves in the anomalous resistivity region. The magnitude of the observed flux,

however, indicates that the ions, even at low energies, are not severely restrained by the waves. If we equate the ion flow (number/sec) in the magnetic tube sections at the source and at the observation altitudes, we get,

$$\langle f v_{||} \rangle A_0 = 2\pi A_s \int_0^{1.25} dw_i \int_0^{15^\circ} j(\alpha_i, B_s, w_i) \sin \alpha_i \cos \alpha_i d\alpha_i \quad (57)$$

where f is the velocity distribution function of the ions, assumed to be Maxwellian, and A_0 and A_s are the normal cross sectional areas of the tube at the source and at B_s . Now, if we assume that all thermal ions with $v_{||} > 0$ along the field become accelerated, then

$$\begin{aligned} \langle f v_{||} \rangle &= \frac{n}{(\pi)^{3/2} v_{th}^3} \int_0^\infty e^{-v_{\perp}^2/v_{th}^2} 2\pi v_{\perp} dv_{\perp} \int_0^\infty e^{-v_{||}^2/v_{th}^2} v_{||} dv_{||} \\ &= n v_{th} / 2 \end{aligned} \quad (58)$$

Here, n is the number density of the ions at the source and v_{th} is the thermal velocity of the ions. By substituting this result and the observed flux in Eq. (57), we find that

$$n \approx \frac{2 \times 10^7}{v_{th}} \cdot \frac{B_0}{B_s} \quad (59)$$

where we have put $A_0/A_s = B_0/B_s$. Thus, since $v_{th} \approx 2 \times 10^5$ cm/sec ($\approx 3000^\circ K$) for O^+ ions, and using $B_0/B_s \approx 3 [(6000 + R_E)^3 / (2500 + R_E)^3]$, we find that an O^+ ion density of about $300/\text{cm}^3$ at the base of the acceleration region can provide the observed flux. Since the H^+ ion thermal velocity is about 4 times that of the O^+ ions, the required H^+ ion concentration is about $80/\text{cm}^3$. The distributions of ions in the polar ionosphere are quite variable. However, such concentrations at altitudes of several thousand kilometers are not unreasonable.

The observed pitch-angle distribution of the ions can also be accounted for by assuming time and/or space variations of the potential model shown in Figure 13. In that model note that ions are accelerated by a weak electric field component along the magnetic field; but at high altitudes, they encounter a much stronger electric field which is perpendicular to the magnetic field. There, the ions will acquire a high $\bar{E} \times \bar{B}$ drift velocity. Mozer et al. (Ref. 7), with instrumentation on the same satellite, has measured electric fields perpendicular to the magnetic field as high as 1 V/m. In such a field at the altitude of the satellite the ions would acquire a v_{\perp} component of about 170 km/sec, which is the velocity of a 2.4 keV O^+ ion. Hence, a perpendicular electric field of about .2 V/m for the O^+ ions, .7 V/m for H^+ , can account for the 15-degree widths of the ion distributions. Certainly both this mechanism and wave-particle interactions must be affecting the ion distributions. The relative importance of the roles of these mechanisms, however, is uncertain at the present time.

The analysis of the additional event of this type that we investigated indicated that the electric potential difference along the magnetic field increased with time and/or space and that the field extended above as well as below the satellite. The data were obtained at 1034 UT, September 15, 1976, at dusk, ~ 18 hr. LT, near the geographical coordinates 101.5° E. Long., 69.5° N. Lat., and at an altitude of 7280 km. At the time of the measurements the satellite was moving toward higher latitudes.

The data obtained during three successive spin periods of the satellite were investigated. Field-aligned H^+ and O^+ ions, with pitch-angle

distributions similar to those described above, were observed on the 2nd and 3d spin periods but not on the first. Accordingly, it will be assumed that the accelerating field was not present at the time of the 1st spin period. (It is most likely that the onset of the electric field was due to the relative motion of the satellite and the region containing the field.) The electron distributions were fairly uniform during several spin periods prior to the observation of the ions. The electron flux measured during the 1st spin period will, therefore, be taken to be the undisturbed flux, $j(\alpha_s, B_s, w_s)$, according to the notation used in Section 4.2, and the electron flux measured later will be the flux perturbed by the field, $j^{(E)}(\alpha'_s, B_s, w'_s)$. The electron distributions changed rapidly during the time of the measurements. Hence, the pitch-angle data shown below for the high counting rate channels, CME B and CME C, are plotted separately for each of the two pitch-angle scans that were made during a particular spin period. These individual scans during a spin period, N , are designated by N^- for the scan of pitch angles from 0 to π and N^+ for the succeeding scan from π to 0. The counting rates of the CME A and CME D channels were low; to improve the statistical accuracy of the data, those counting rates were averaged over similar pitch-angle intervals observed during scans N^- and N^+ .

The pitch-angle measurements obtained with the CME A detector are shown in Figures 15a and b. The triangles in Figure 15a designate the averaged counting rates obtained during spin 1 and the open circles designate the rates obtained during spin 3. Figure 15b shows the counting rates obtained on the individual scans 2^- and 2^+ . Note that the undisturbed flux of these low-energy electrons, .074-.238 keV, is quite uniform, even in the loss cones.

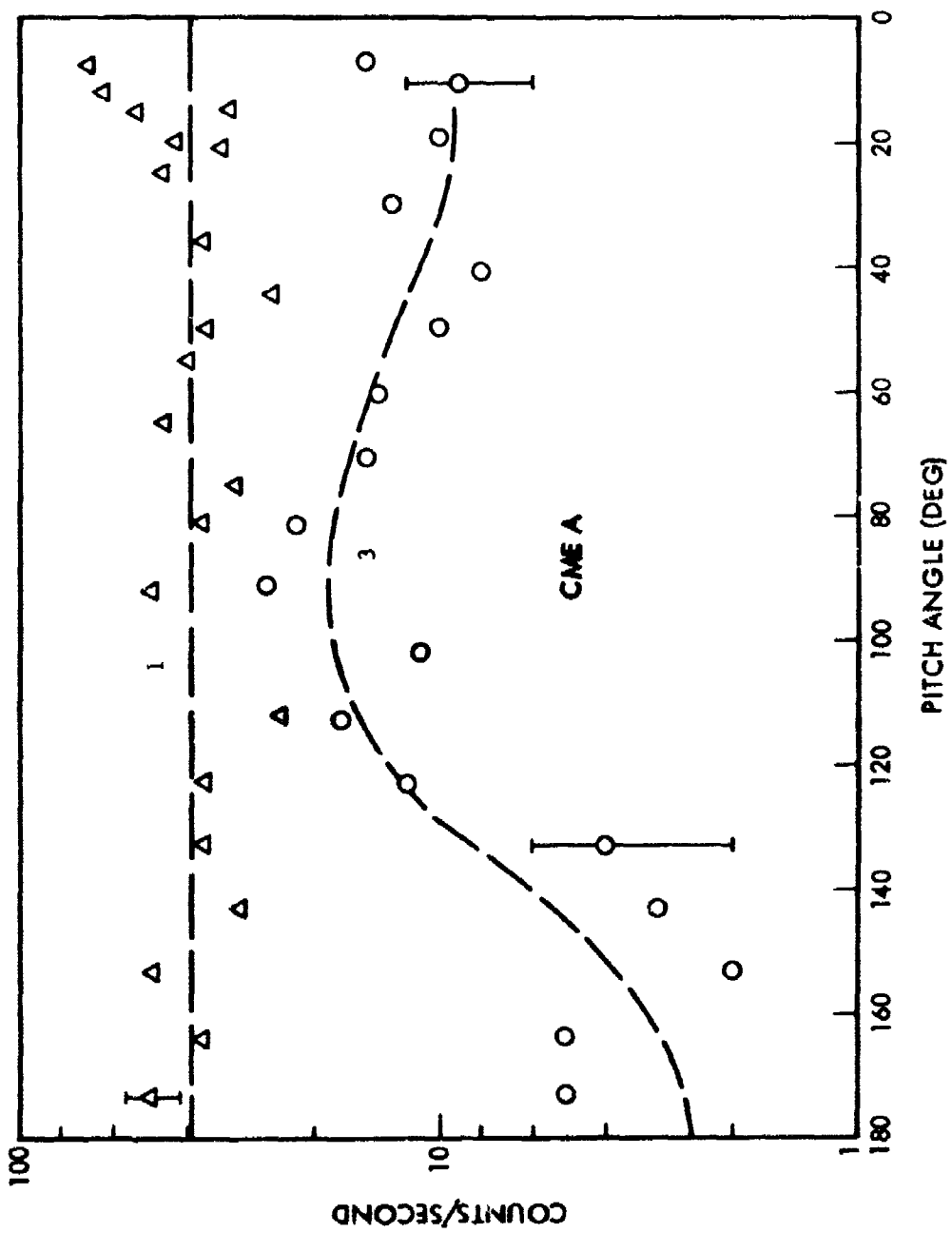


Figure 15a. Pitch-angle data obtained on spins 1 and 3 by the CME A detector.

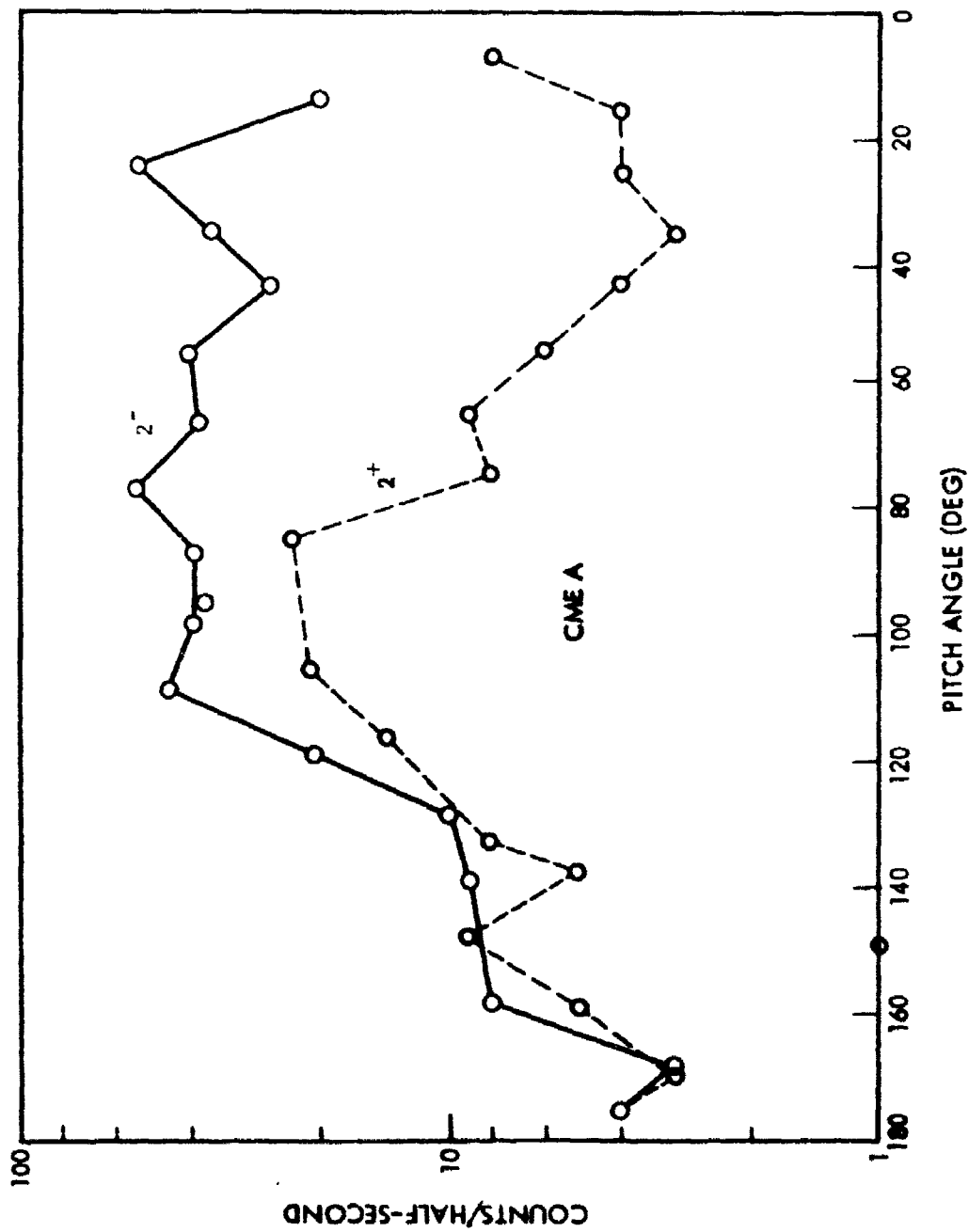


Figure 15b. Pitch-angle data obtained on spin 2 by the CME A detector.

This isotropy is expected on the basis of the pitch-angle diffusion results discussed in Section 2. A diminution of the flux of electrons returning from the near atmosphere (the near loss cone, $\alpha \geq 130^\circ$) is indicated in the perturbed flux on spins 2 and 3.

The pitch-angle distributions measured with the CME B detector on spins 1, 2 and 3 are shown in Figures 16a, b and c, respectively. The counting rates from both scans of the pitch angle range for each spin period are shown in the Figures. Note that the electrons heading toward the near atmosphere are approximately isotropic, except in scan 3⁻. Also note that the near loss cones become progressively deeper and wider in the successive spin periods, and that beyond the edge of the loss cone the counting rates increase in the successive spin periods.

The pitch-angle data obtained with the CME C detector display characteristics similar to those of the CME B detector. For these higher-energy electrons, however, the far atmosphere loss cone, $\alpha \leq 30^\circ$, is evident in the 1⁻ scan. These data are shown in Figures 17a, b and c.

The pitch-angle data obtained on spins 1 and 3 by the CME D detector are shown in Figure 18. The statistical accuracy of the data is rather poor. Nevertheless, the near and far atmospheric loss cones can be discerned. Moreover, the counting rates (open circles) on spin 3 exhibit maxima near the edges of the loss cones, at 40° and 140° .

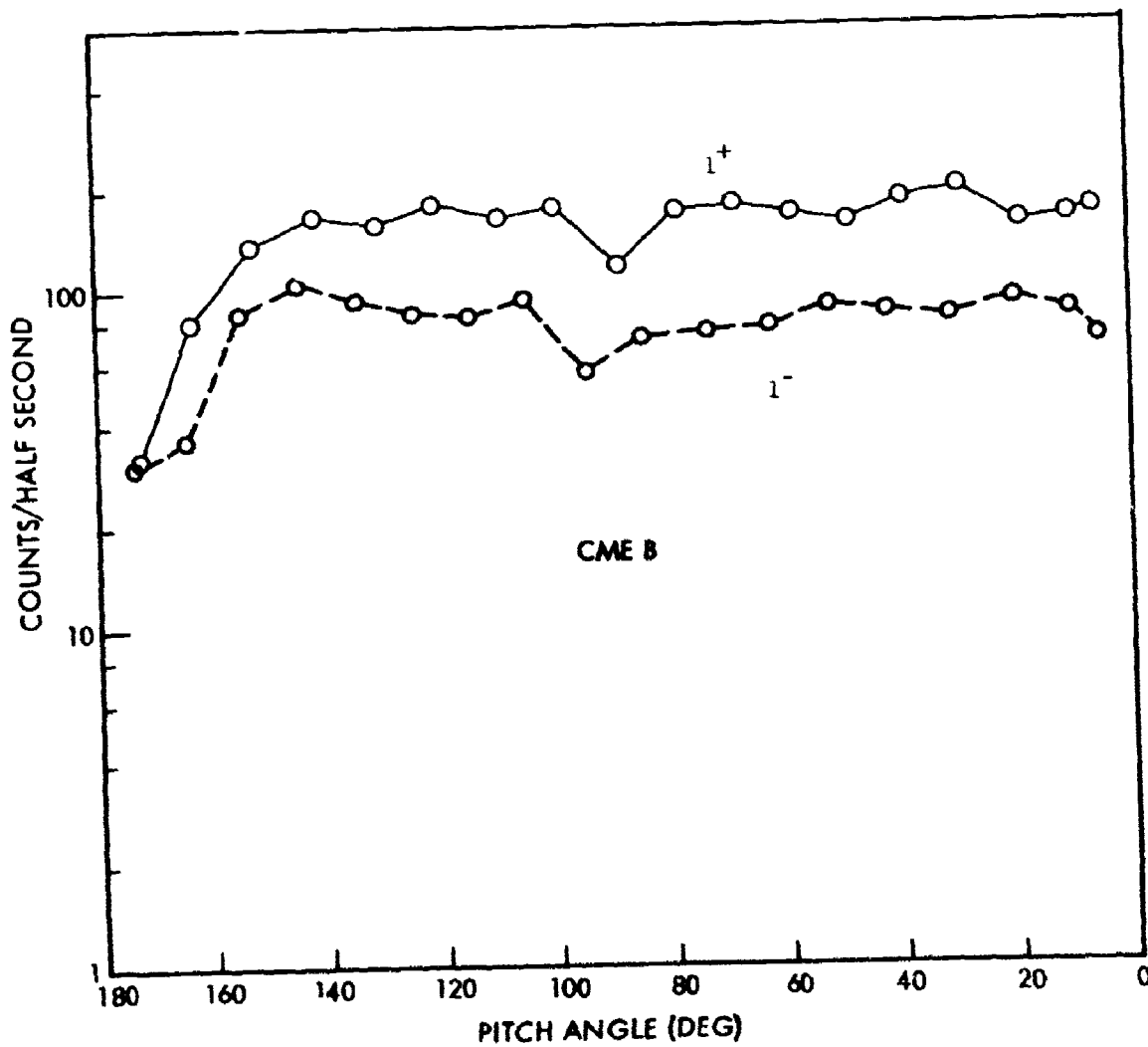


Figure 16a. Pitch-angle data obtained on spin 1 by the CME B detector.

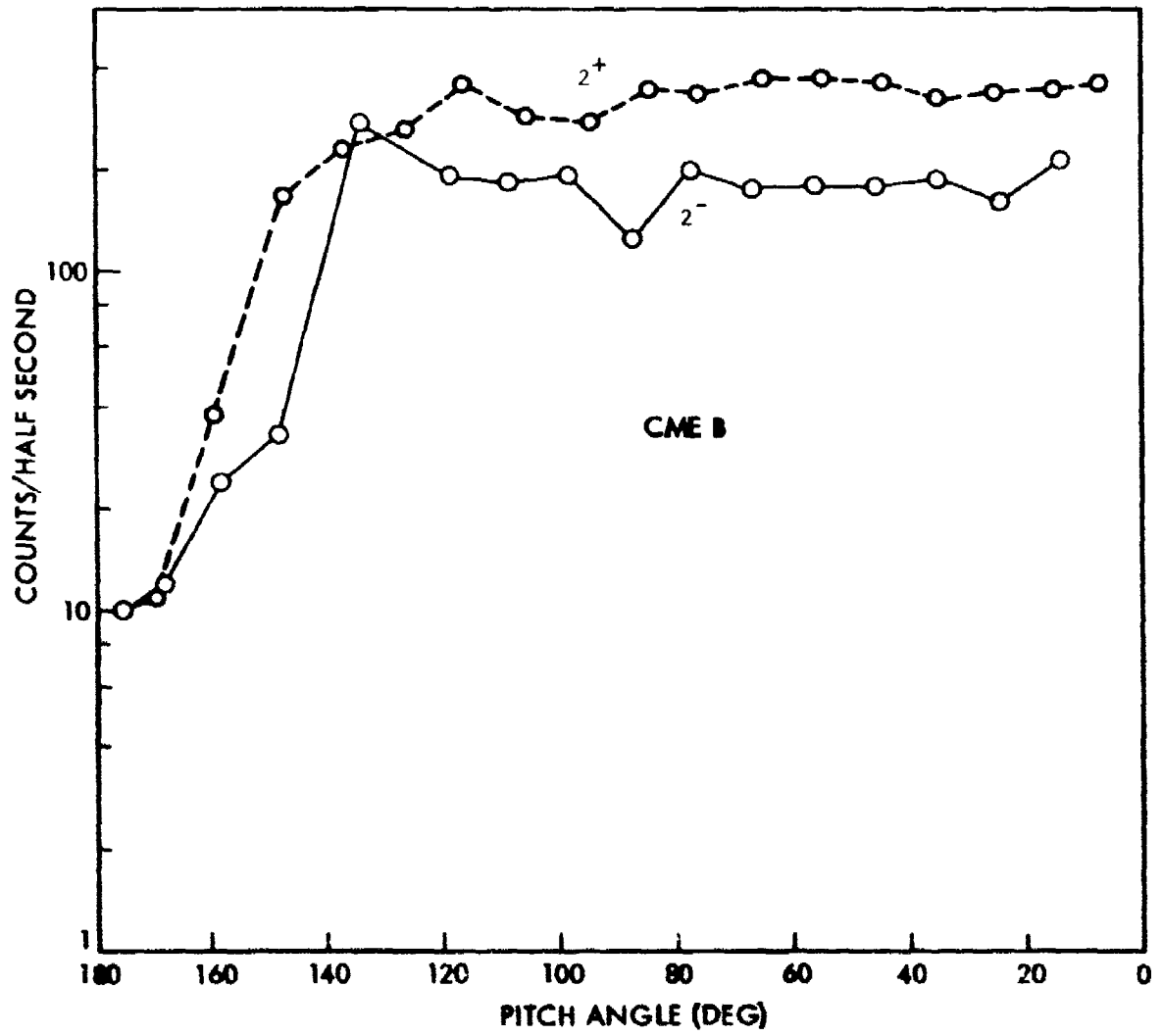


Figure 16b. Pitch-angle data obtained on spin 2 by the CME B detector.

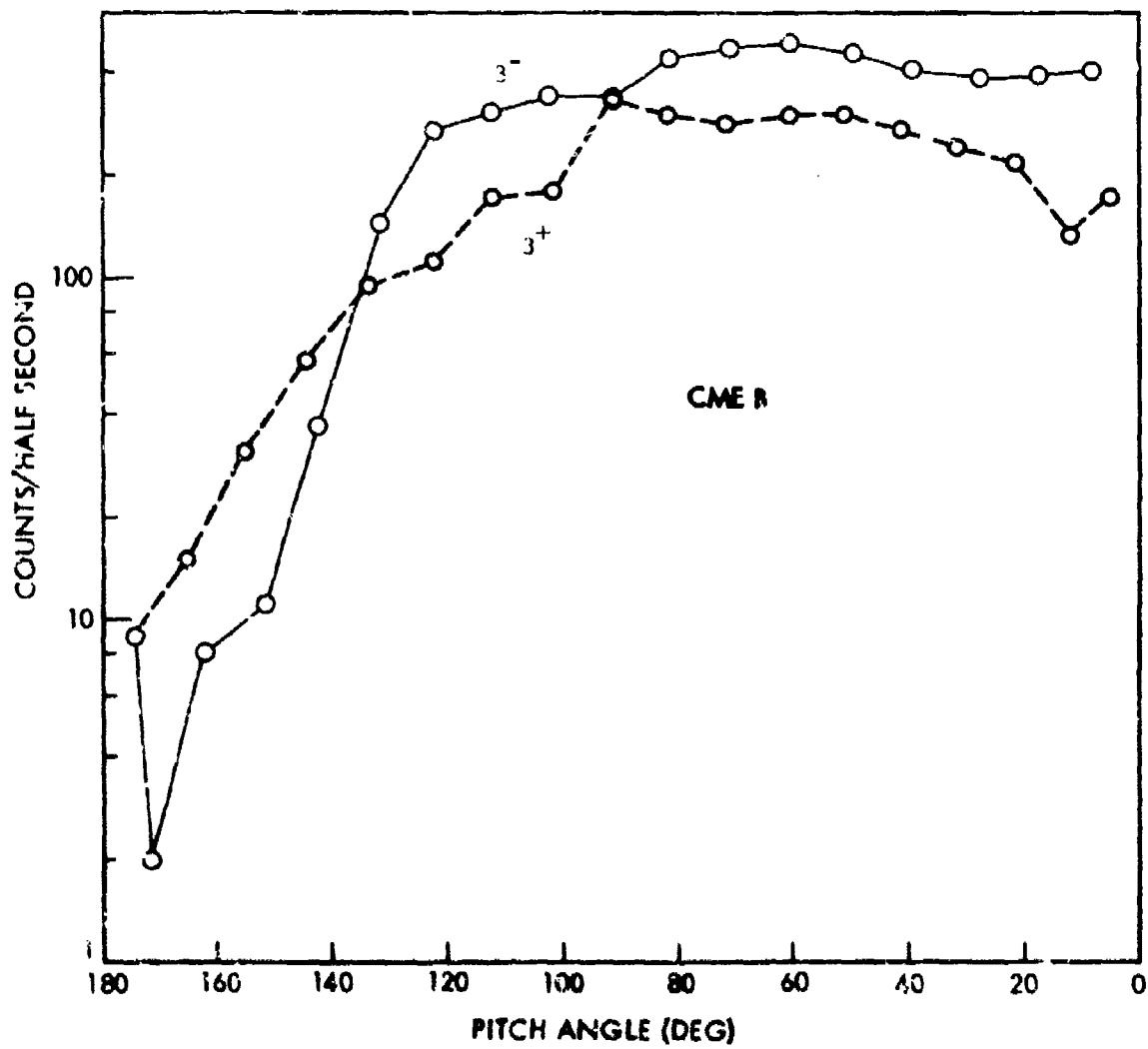


Figure 16c. Pitch-angle data obtained on spin 3 by the CME B detector.

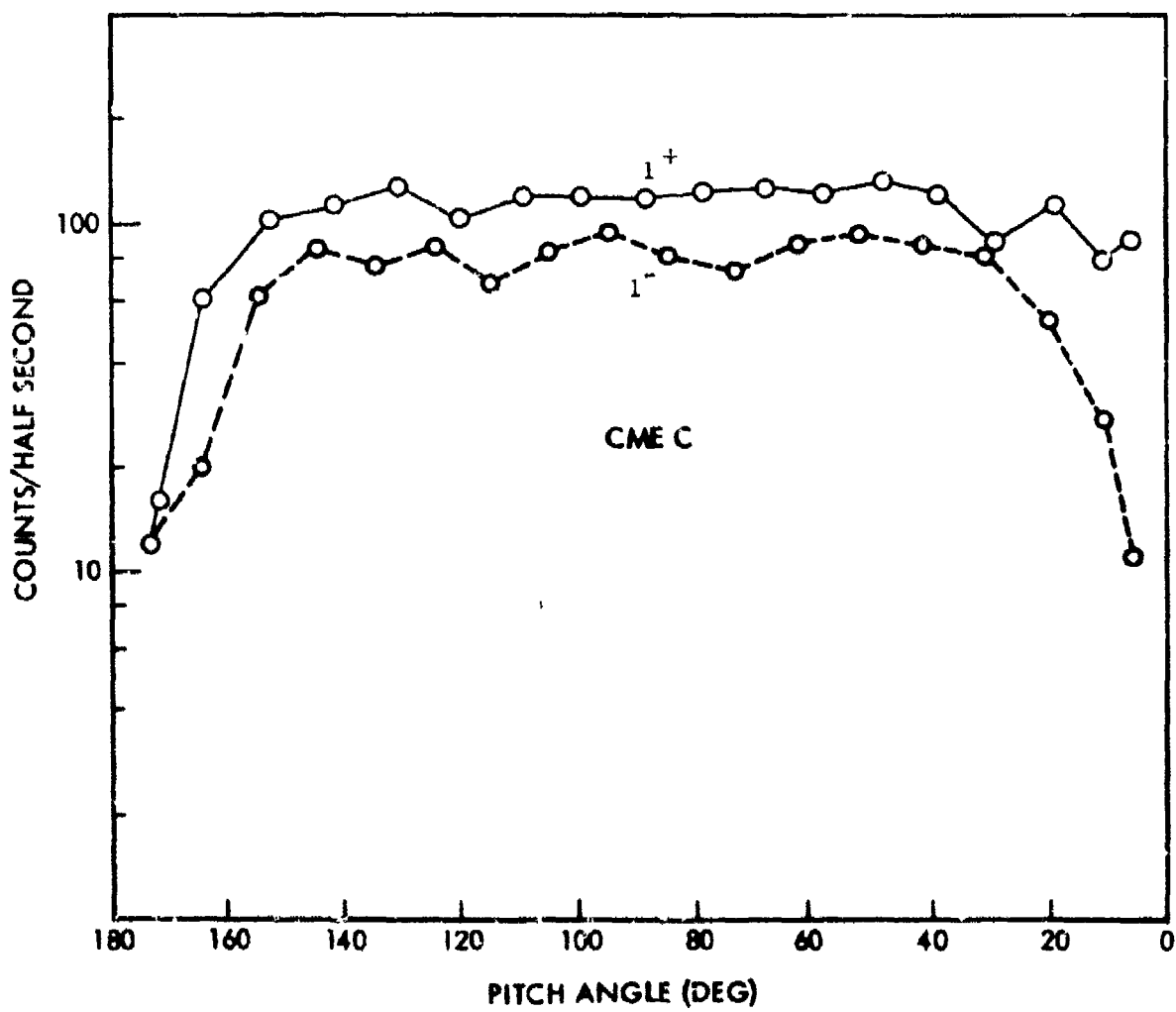


Figure 17a. Pitch-angle data obtained on spin 1 by the CME C detector.

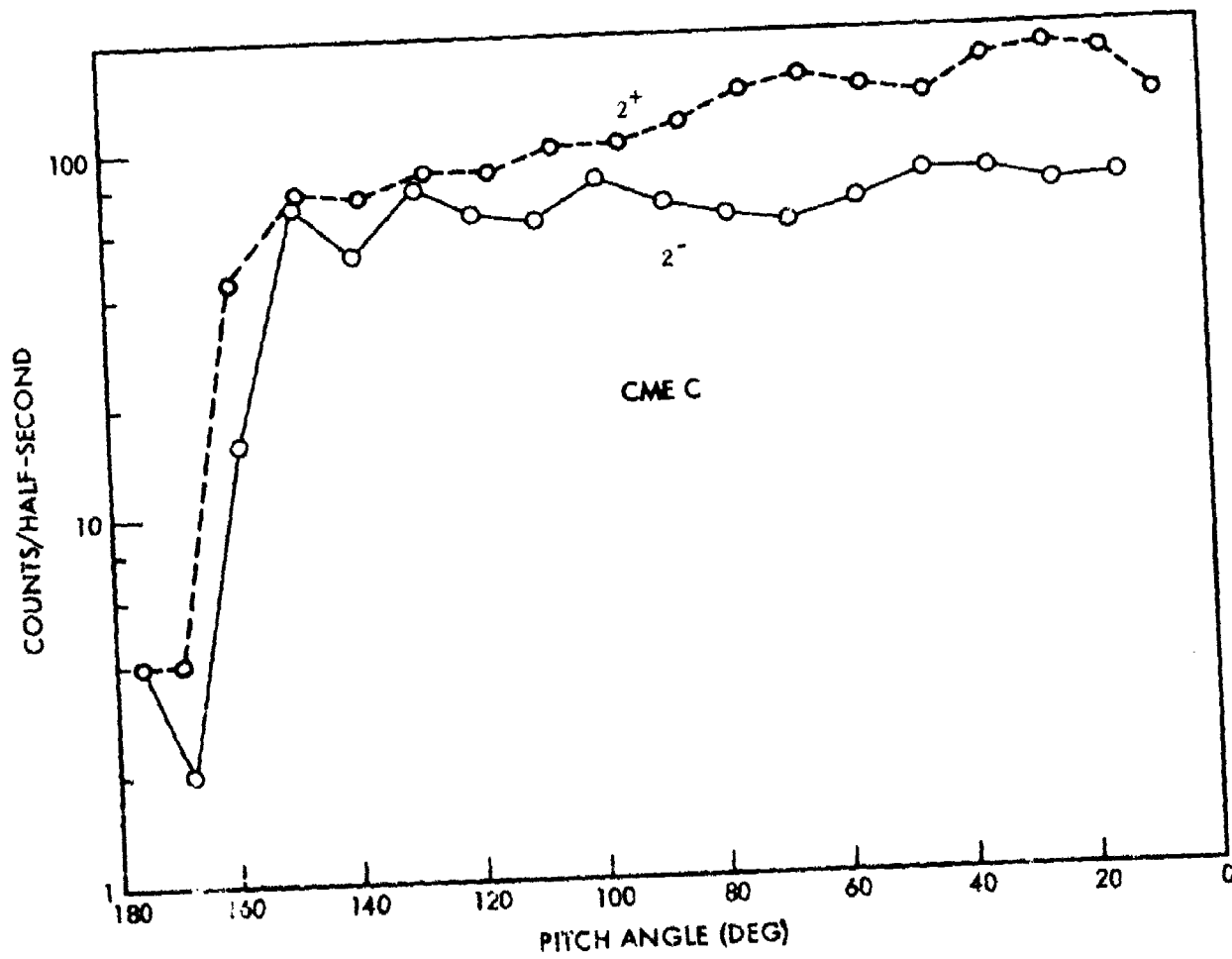


Figure 17b. Pitch-angle data obtained on spin 2 by the CME C detector.

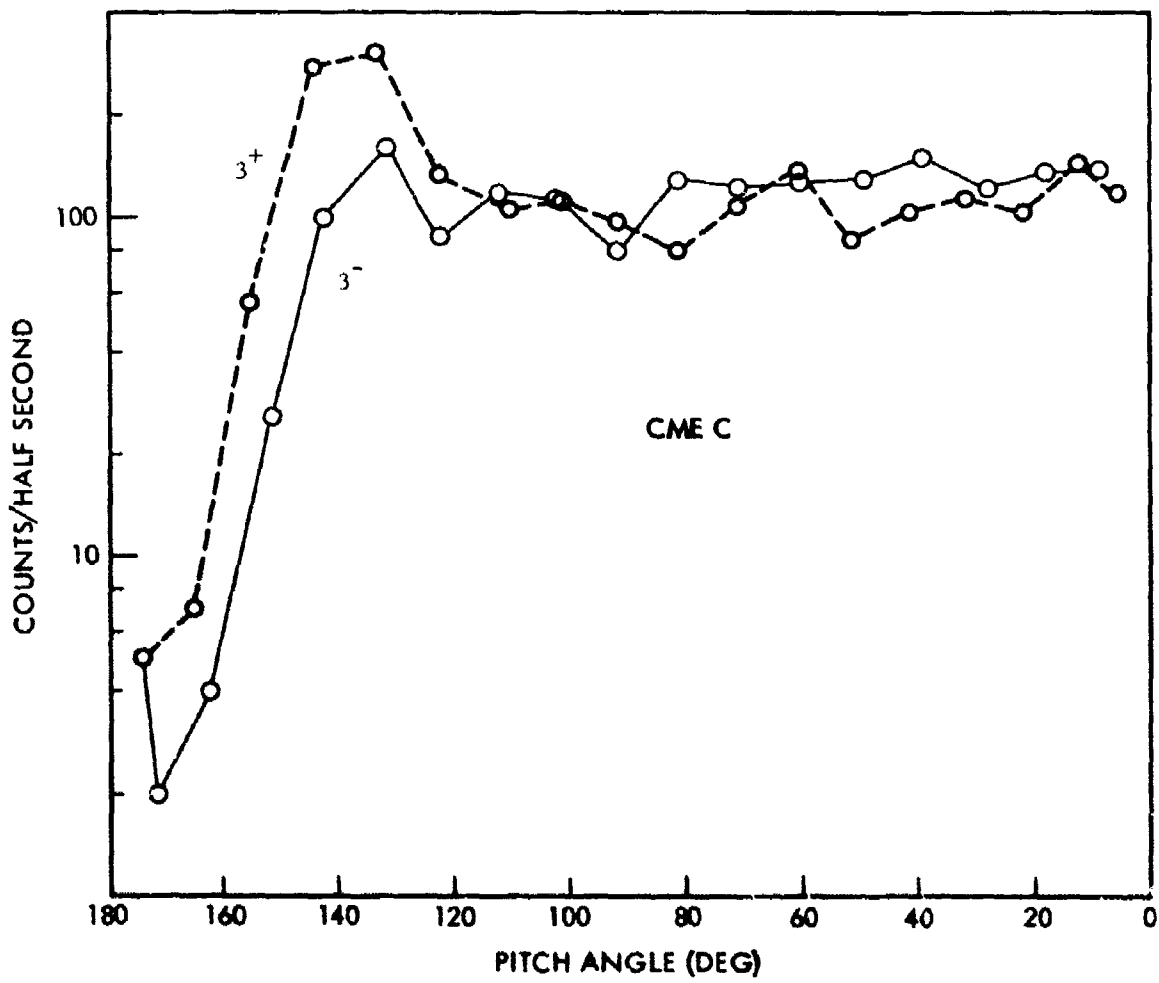


Figure 17c. Pitch-angle data obtained on spin 3 by the CME C detector.

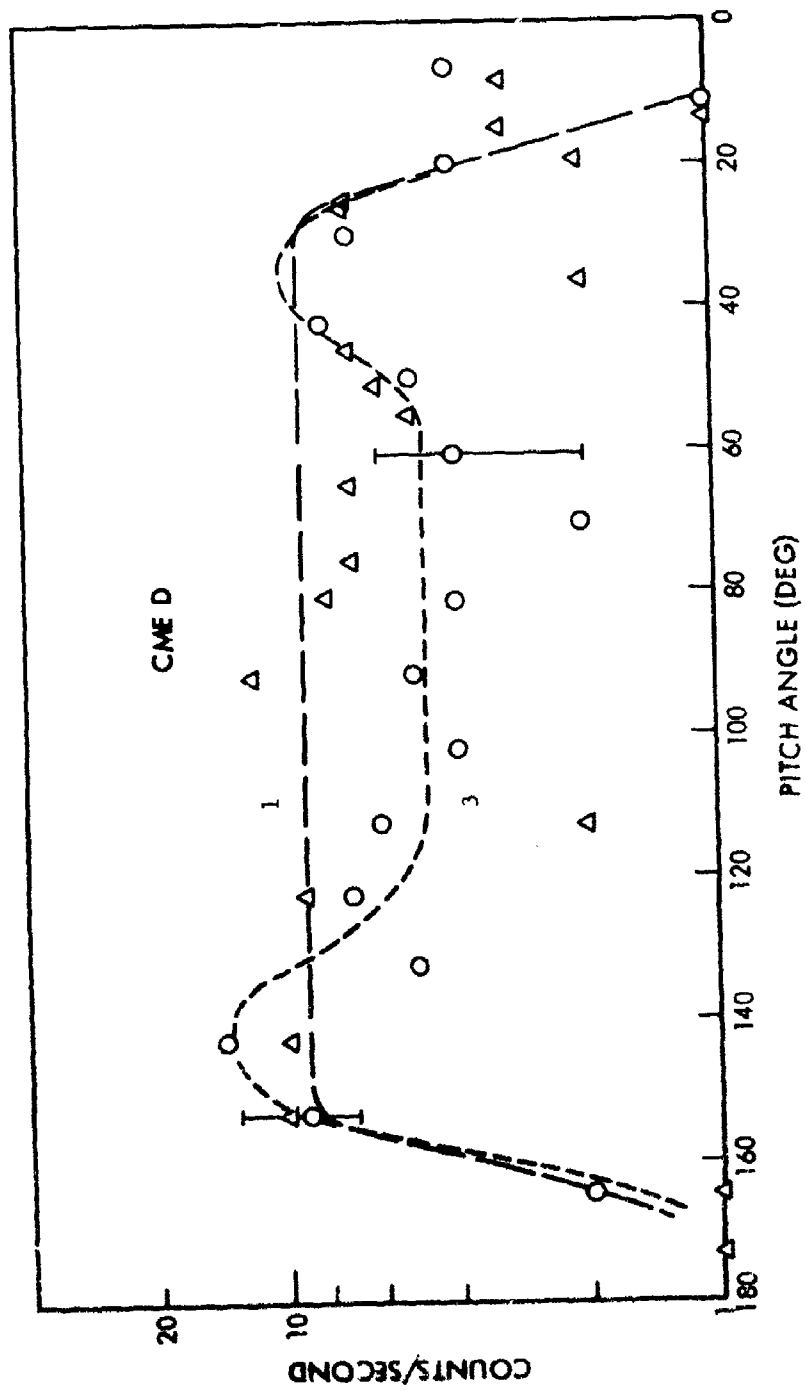


Figure 18 Pitch-angle data obtained on spins 1 and 3 by the CME D detector.

The energy spectra of the electrons detected on spins 1 and 3 are shown in Figure 19. These spectra were obtained simply by dividing the mean values of the counting rates, outside the loss cones, by the geometric factors of the detectors, and plotting the results at the peak-response energies of the detectors. The triangles shown in the figure will be explained later.

The potential difference, φ_b , below the satellite can be estimated from the widths of the near loss cones. The relationship of the edge of a loss cone to the electron energy and φ_b is given in Equation (48). In Figure 20 the width of the loss cone given by this equation is plotted as a function of $e\varphi$ for each of the central energies of the electron detectors. Here, the ordinate, $\Delta\alpha'_{sc}$, denotes the difference $180^\circ - \alpha'_{sc}$. In evaluating Equation (48), the ratio B_s/B_t was set equal to the third power of the ratio of the geocentric distance to the "top" of the atmosphere (altitude ≈ 300 km) to the geocentric distance to the satellite.. The widths of the loss cones estimated from the detector data taken on spins 1, 2 and 3 are listed in Table IV. The values of $e\varphi_b$ corresponding to these widths, as determined from Figure 20, are listed in Table V.

The results indicate that the potential below the satellite was 0 on spin 1, and increased to ~ 1.5 kV on spin 2 and to ~ 3.8 kV on spin 3. The values of $e\varphi_b$ inferred from the CME A data, especially on spin 3, are not reliable because of the extreme sensitivity to the electron energy of the curve shown in Figure 20 for this detector. Moreover, as discussed below,

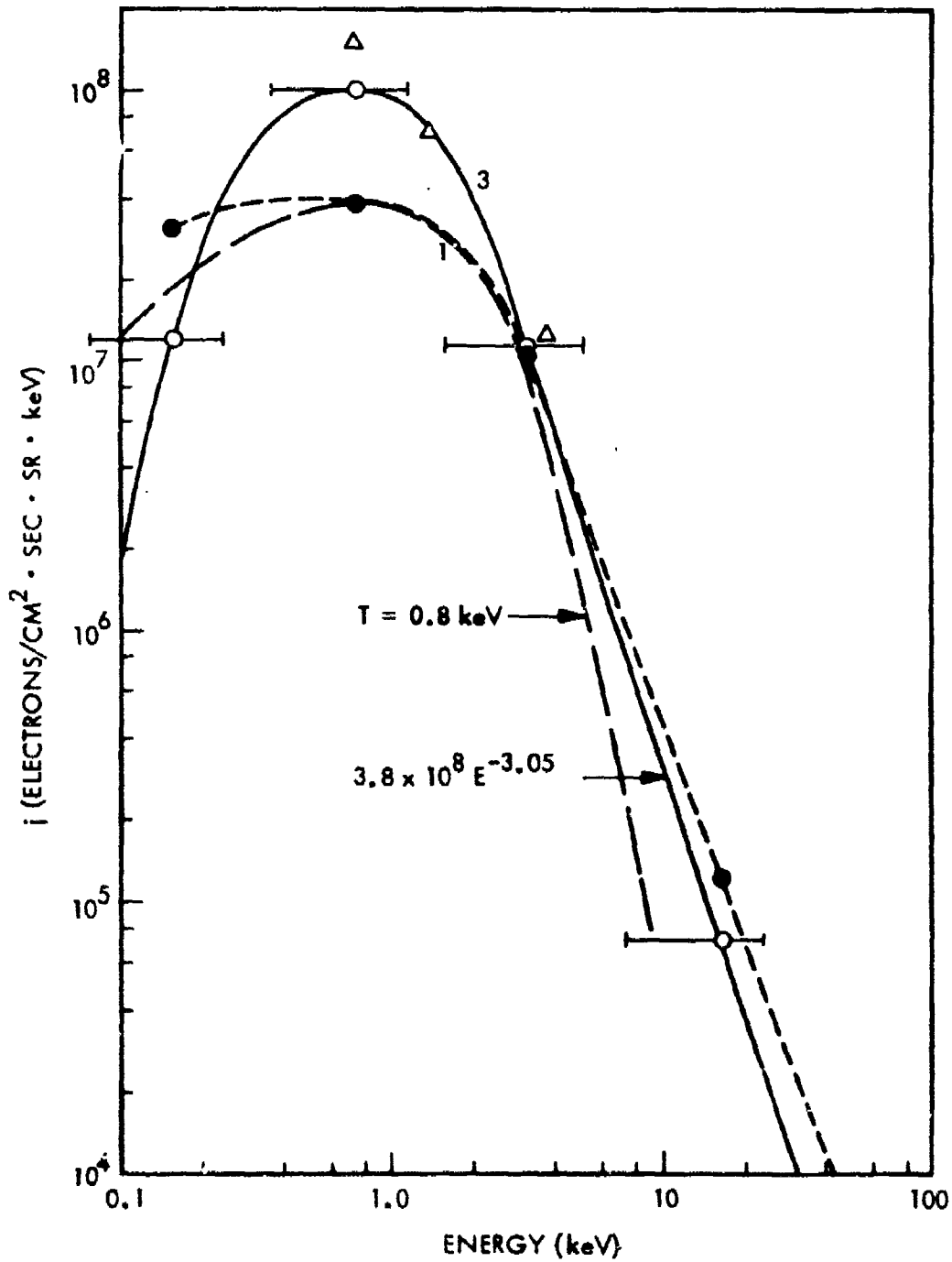


Figure 19. Energy spectra of electrons measured on spins 1 and 3. The triangles are the spectral intensities of the disturbed flux computed from the spin 1 data assuming a .5 kV potential above the satellite. A Maxwellian distribution with $T = .8 \text{ keV}$ is shown for comparison.

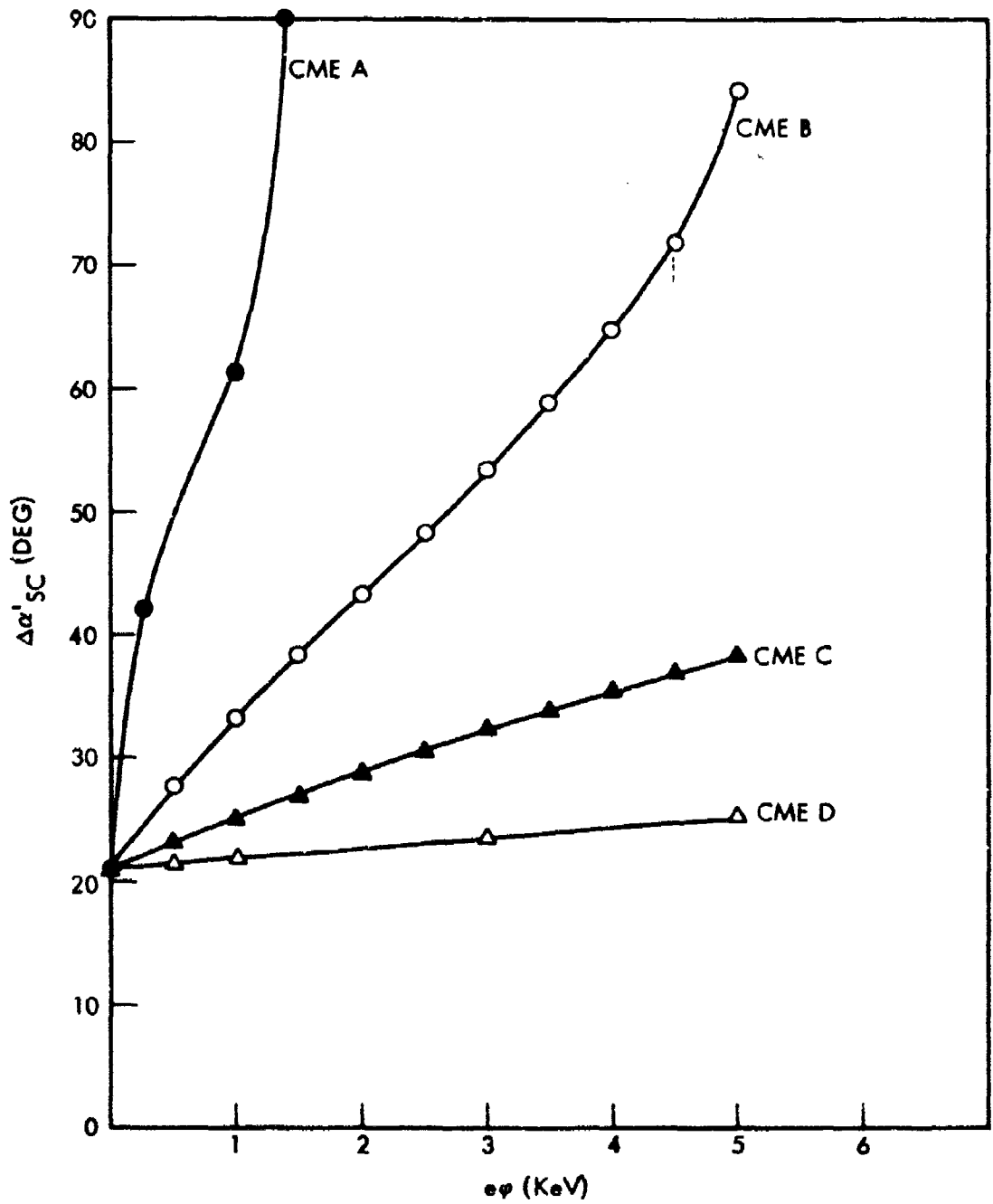


Figure 20. Theoretical relationship of loss-cone width observed by electron detectors to the electric potential below the satellite.

TABLE IV

Observed Values of Loss Cone Widths in Degrees

Spin Number	CME A	CME B	CME C	CME D
1	0	21	21	~ 24
2	70	39	27	
3	75	60	35	~ 27

TABLE V

Values of $e\phi_b$ in keV Inferred From Loss Cone Widths

Spin Number	CME A	CME B	CME C	CME D
1	-	0	0	-
2	1.2?	1.5	1.5	-
3	1.2?	3.6	3.9	-

the reduction of the counting rate of this detector on spin 3 indicates that the electrons above the satellite were accelerated by an additional potential of about 0.5 kV. The detector therefore may have been counting electrons with energies far from its principal energy-response band.

The potential below the satellite was also estimated from the depths of the loss cones, by using the AURORA code to compute the flux of back-scattered electrons for various assumed values of the potential. The incident flux at the top of the potential region was taken to be isotropic and to have the spectra shown in Figure 19. The spin 1 spectrum was used for the $\phi_b = 0$ condition, and the spin 3 spectrum was used for $\phi_b > 0$. Results were obtained for $\phi_b = 1.5, 3.0$ and 4.5 kV. In general, it was found that the backscattered flux of electrons which reached the satellite decreased rapidly as ϕ_b increased. However, for the $\phi_b = 0$ case, the computed back-scattered flux was less than that observed at the satellite on spin 1. This discrepancy is believed to exist because the high-energy AURORA code, which was used for this analysis, does not compute the production of secondary electrons. These electrons are not important for most applications of the code, but they are significant in the computation of the backscattered flux. Because of this difficulty, the loss-cone depth computed for each value of ϕ_b was divided by the depth for $\phi_b = 0$ and the ratios were compared with the ratios formed by dividing the loss-cone depths observed on spins 2 and 3 by the depth observed on spin 1. This procedure tends to cancel errors in the back-scattered flux which are proportional to the flux. The observed ratios are listed in Table VI. Comparison with the computed ratios in Table VII indicates that $\phi_b \approx 1.5$ kV on spin 2 and $\phi_b \approx 4$ kV on spin 3. These values are considered to be in good agreement with those listed in Table V.

TABLE VI

Observed Ratios of Loss Cone Depths

Spin Number	CME C Data
	$\left(\frac{\text{Depth on numbered spin}}{\text{Depth on Spin 1}}\right)$
1	1.0
2	3.0
3	8.8

TABLE VII

Computed Ratios of Loss Cone Depths

Potential, φ_b , in kV	AURORA Code Results
	$\left(\frac{\text{Depth for } \varphi = \varphi_b}{\text{Depth for } \varphi=0}\right)$
0	1
1.5	2.8
3.0	5.6
4.5	10

The O^+ and H^+ ion data indicate somewhat higher values of ϕ_b . On spin 1, of course, the ions were not present, which is consistent with $\phi_b = 0$. The data from the energy-mode channels prevailing at the time of spin 2 indicated high fluxes of O^+ at 3.3 keV and H^+ ions at 0.94 keV. On spin 3 high fluxes of both O^+ and H^+ ions were observed at 4.5 keV.

The electron data also indicate that a potential of about 0.5 kV existed above the satellite on spin 3. Application of Equation (37), taking as the undisturbed flux, $j(\alpha_s, B_s, w_s)$, the flux detected on spin 1 (see Figure 19) and assuming $\phi_1 \approx .5$ kV, the calculated flux disturbed by the electric field reproduces fairly well the flux observed on spin 3. The flux values calculated in this manner, using the CME A, CME B, and CME C data on spin 1, are given by the triangles in Figure 19. This potential is also consistent with the peaking of the CME A counting rates at 90° and the approximate symmetry of the counting rates about 90° on scans 2⁺ and 3. This detector is evidently counting principally electrons which are backscattered from the atmosphere and reflected from the potential above the satellite. Furthermore, the potential above the satellite is inferred from the enhanced counting rates of the CME C and CME D detectors near the edges of the loss cone. For small values of B_s/B_1 , the electric potential above the satellite reduces the pitch angles of the electrons such that the lower energy electrons within the detector energy bands are more nearly aligned with the magnetic field. This effect appears to account entirely for the CME D counting rates. The peak in the CME C detector may also be due to trapping of the electrons between the electric field above the satellite and the magnetic field below. Application of Equation (50), with B_1 set equal to the magnetic field intensity 1000 km above the satellite, indicates that electrons of energies .94 - 2.63 keV (within the response of the CME C detector) may be trapped in this manner for $\phi_b = 3.7$ kV and $\phi_1 = 0.5$ kV.

5. IONOSPHERIC IRREGULARITIES DUE TO ATMOSPHERIC HEAVE

A high altitude nuclear detonation heats the atmosphere principally through the absorption of X-rays near 80 km. The heated atmosphere rises, approximately vertically, and through collisions moves plasma across the magnetic field. As in the case of the dynamo, an electric field is induced in the plasma. The polarization field resulting from the induced field propagates up magnetic field lines and causes the plasma all along the field line to convect outward at the $\bar{E} \times \bar{B}$ drift velocity. The situation is similar to the atmospheric dynamo which is driven by the tidal motions of the atmosphere. If the velocity of the ions relative to the electrons exceeds the thermal velocity of the ions, the Farley-Buneman instability (Refs. 8 and 51) may occur and lead to the formation of magnetic-field aligned plasma irregularities.

The Farley-Buneman instability is based on the familiar plasma ion wave instability known as the two-stream instability. This instability for the case of a highly ionized collisionless plasma has received considerable theoretical study and is well understood (Refs. 51, 52, 53, 54 and 55).

Farley (Ref. 8) extended the simple two-stream theory to the problem of field-aligned irregularities in the ionosphere, taking into account the presence of the geomagnetic field and the effect of collisions between the charged and neutral ionospheric particles. The results show that plane electrostatic waves, and associated irregularities in ionization density along field lines, will

appear spontaneously in ionospheric regions where strong currents flow perpendicular to the geomagnetic field lines, providing $\hat{k} \cdot \bar{v}_d > a_i$. Here \hat{k} is the unit wave propagation vector, \bar{v}_d is the relative drift velocity between the electrons and ions, and a_i is the thermal speed of the ions.

Buneman (Ref. 56) has also considered the electrojet problem, using the Navier-Stokes fluid equation rather than the more complicated Boltzmann equation applied by Farley. In the high collision frequency limit where the two approaches may be compared, Farley found that his and Buneman's dispersion equations are essentially in agreement.

The conditions required for the onset of the Farley-Buneman instability have been verified for both the equatorial and auroral regions (Refs. 57, 58, 59, 60 and 61).

Much attention has already been given to processes which may be responsible for the striations photographed during the high altitude nuclear tests; and, indeed, the effects of specific mechanisms have been incorporated in various codes. To our knowledge, the mechanism discussed here has not yet been considered (Ref. 62). Yet, it appears to be quite straightforward, and it does account for a feature not explained by other mechanisms, namely the 30-40 sec delay time in the appearance of the striations following a nuclear burst. In the proposed mechanism, this feature is expected because the atmosphere below the burst does not move upward sufficiently rapidly at times shorter than the observed delay time.

In this section we discuss the possibility that the Farley-Buneman instability might occur following a nuclear detonation.

The ionosphere and debris near a high altitude nuclear explosion are rendered highly conducting. The net effect is to enhance the tendency of plasma to move as a single fluid in which ions and electrons are tied firmly to the field lines. The likelihood of plasma instabilities driven by relative motion between ions and electrons is therefore low in the ionosphere below the detonation point. At large distances, however, the conductivity remains only slightly elevated; so the question remains whether instabilities could be excited there.

A simplified model was used to estimate the relative drift motion of the ions and electrons in regions of the ionosphere where the atmospheric heave is not prominent. The model is illustrated in Figure 21. The ion velocity across the magnetic field, driven by the expansion of the atmosphere, is assumed to be uniform within the circular region of radius R . \bar{E}_{ind} is the resulting $\bar{v}_i \times \bar{B}$ electric field induced by the plasma motion. This field is generally directed toward the west for the burst occurring in the northern hemisphere. Outside the circular region the heave motion is assumed to be negligible. The field \bar{E}_{ind} will therefore produce polarization charges at the boundary of the circular region, as indicated in the figure, and these charges will propagate upward along the local magnetic field lines. Since the atmosphere expands on a long time scale -- tens to hundreds of seconds -- charges spread to distances along the magnetic field which are much greater

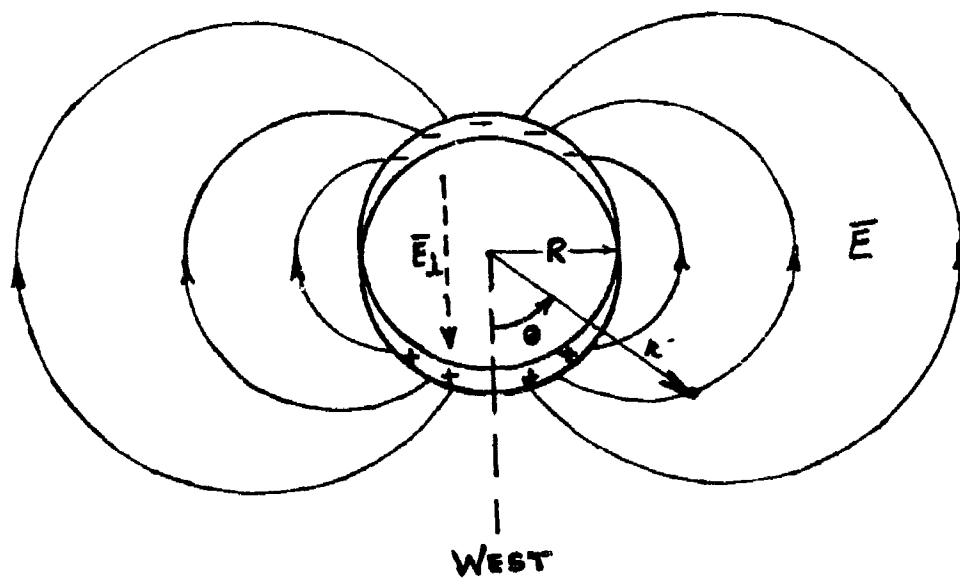


Figure 21. Schematic representation of electric field distribution resulting from the atmospheric heave. R is the effective radius of the "heave" region. E_L is the induced electric field, and E is the electrostatic field.

than the transverse extent of the electrostatic field. Accordingly, the charges were assumed distributed in a tubular region, and a two-dimensional solution, in a plane perpendicular to \bar{B} , was obtained for the ensuing electrostatic potential.

In cylindrical coordinates, r, θ , the solution inside the tubular region is,

$$\phi_i = E_{\text{ind.}} r \cos \theta . \quad (60)$$

The electrostatic field inside the tube is therefore equal and oppositely directed to $\bar{E}_{\text{ind.}}$. Hence, the plasma in the tube will drift with the velocity $-\bar{E}_{\text{ind.}} \times \bar{B} = (\bar{v}_i)$, which is the velocity at which the ions near the base of the tube are forced across the magnetic field by the neutral atmosphere. Hence, the relative velocity of the ions and electrons will be zero.

Outside the tube the potential solution is,

$$\phi = E_{\text{ind.}} \frac{k_i R^2}{k_o r} \cos \theta \quad (61)$$

where k_i and k_o are the dielectric constants of the plasma inside and outside the tubular region. The electric-field components outside the region are, therefore,

$$E_r = E_{\text{ind.}} \frac{k_i R^2}{k_o r^2} \cos \theta \quad (62)$$

$$\text{and } E_\theta = E_{\text{ind.}} \frac{k_i R^2}{k_o r^2} \sin \theta . \quad (63)$$

The distribution of this electric field is depicted in Figure 21.

According to the MICE code results for a Standard SPARTAN (200 km), the ion velocity in the ionospheric region beneath the burst where the ions are coupled to the neutrals is about 5×10^5 cm/sec. Similar velocities are given by the MRHYDE code for the Check Mate test. If the inclination of the magnetic field is taken to be 45° and $B \approx .5$ gauss, then the induced field is very high, about 1.8 V/m. The dielectric constants are approximately proportional to the plasma density. In the undisturbed E-region of the ionosphere the ionization density during the daytime at mid-latitudes is about 3×10^5 ions/cm³. Results of the MRHYDE and MICE codes indicate E-region ionization enhancements by a factor of 100 to 1000. For the Standard SPARTAN (200 km) the effective value of k_i/k_o is in the range 10 to 100 for $R \approx 1000$ km. This value of R seems appropriate because the Spartan data indicated that there the ion velocities are down by more than a factor of 10 and the ion temperatures are nearly equal to the undisturbed E-region ion temperatures. Using these values in Equation (63) to evaluate E, the resulting $E \times B$ drift velocity, for $B = .5$ gauss, at $r = 2R$ is found to be greater than about 10^7 cm/sec. This velocity, which is nearly equal to the relative ion-electron velocity in the E-region of the ionosphere, is much higher than the ion thermal velocity ($\approx 10^5$ cm/sec) in the undisturbed E-region of the ionosphere. Hence, the Farley-Buneman instability criterion is satisfied.

In this analysis the effect of the ionospheric conductivity on the magnitude of the electrostatic field in the E-region has not been taken into account. The conductivity would reduce the field. However, the effect is not expected to be severe. In the auroral zones, electric fields of about .06 V/m observed above the ionosphere are found to produce relative velocities in the E-region greater than the ion thermal velocity and to form field-aligned

irregularities. Such fields are smaller than the one estimated above by more than an order of magnitude.

It may be concluded that the Farley-Buneman instability has not been ruled out in the ionosphere near a high altitude nuclear explosion, but, because of elevated conductivities there, this instability mechanism is not unlikely. In the distant E-region, the plausibility of the Farley-Buneman instability has been demonstrated. However, the uncertainties in the calculation make it imperative that a more detailed calculation be performed.

6. CONCLUSIONS AND RECOMMENDATIONS

It was found that:

o Large amplitude scintillations can occur at all times in mid-latitudes, but show no strong correlation with well known ionospheric and geomagnetic activity indicators.

o The distribution of trapped particles precipitating into the ionosphere depends on diffusion into the loss cone, backscatter from the atmosphere, azimuthal drift, and electric fields aligned along the magnetic field; all of which produce recognizable and distinguishable effects.

o Several characteristics of the electric fields due to plasma instabilities in the upper ionosphere, and the effects of these fields on ions in the ionosphere and electrons in the magnetosphere, have been inferred from analyses of the Satellite 1973-65B data.

o The Farley-Buneman instability can be excited by a high altitude nuclear explosion. The resulting plasma irregularities in the ionosphere may extend to distances of several thousand kilometers about the "sub-burst" point in the ionosphere.

It is recommended that:

o The WIDEBAND program, and future programs, be directed to make the best use of opportunities to obtain mid-latitude scintillation data; and the theoretical efforts be expanded to further the understanding of the underlying mechanisms that lead to ionospheric instabilities - both in mid and high latitudes.

o Further Satellite 1973-65B data on the energy and angular distributions of keV-type ions and electrons be analyzed to obtain additional information on electric fields produced in the auroral and polar regions and the conditions under which they occur.

o Satellite 1973-65B data on the energy and angular distributions of 10-100 keV electrons be analyzed to obtain definitive information on the diffusion rates of trapped electrons at mid-latitudes, hence to calibrate the theoretical model discussed in Section 2.

o Further studies be conducted to determine the electric fields and currents in and above the ionosphere that result from high-altitude nuclear explosions and to test the results against existing plasma-instability criteria.

REFERENCES

1. J. B. Cladis, G. T. Davidson, W. E. Francis, M. Walt; "Ionospheric Effects Resulting from Precipitating Electrons at Mid and High Latitudes," DNA Report 3884F, Headquarters, Defense Nuclear Agency, Washington, D.C. 20305, 1976.
2. G. T. Davidson, M. Walt; "Pitch Angle Diffusion Within the Loss Cone of Trapped Electrons," J. Geophys. Res. in press, 1976.
3. M. Walt, W. E. Francis; "Penetration of Auroral Electrons into the Atmosphere," Physics of the Magnetosphere, R. L. Carovillano, J. F. McClay, eds., Reinhold, New York, p. 534, 1968.
4. J. B. Cladis, G. T. Davidson, W. E. Francis, L. L. Newkirk, M. Walt; "Ionospheric Disturbances Affecting Radio Wave Propagation," DNA Report 3103F, Headquarters, Defense Nuclear Agency, Washington, D.C. 20305, 1973.
5. E.G. Shelley, R.D. Sharp, and R.G. Johnson, "Satellite Observations of an Ionospheric Acceleration Mechanism," Geophys. Res. Letters, 3, 654, 1976.
6. C.E. McIlwain, "Bouncing Clusters of Ions at Seven Earth Radii," EOS Trans. Am. Geophys. Union, 57, 307, 1976.
7. F.S. Mozer, B. Parady, and R.B. Torbert, "Vector Electric Field and Density Fluctuations Measured on a High Altitude Polar Orbiting Satellite," EOS, Trans. Am. Geophys. Union, 57, 986, 1976.
8. D.T. Farley, Jr., "A Plasma Instability Resulting in Field-Aligned Irregularities in the Ionosphere," J. Geophys. Res., 68, 6083, 1963.
9. M. Schulz, L.J. Lanzerotti, Particle Diffusion in the Radiation Belts, Springer, New York, 1974.
10. M. Walt, W.M. MacDonald, "Energy Spectrum of Electrons Trapped in the Geomagnetic Field," J. Geophys. Res. 66, 2047, 1961.
11. C.F. Kennel, H.E. Petschek, "Limit on Stably Trapped Particle Fluxes," J. Geophys. Res. 71, 1, 1966.
12. J.M. Cornwall, "Scattering of Energetic Trapped Electrons by Very-Low Frequency Waves," J. Geophys. Res., 69, 1251, 1964.

13. G.T. Davidson. "An Improved Empirical Description of the Bounce Motion of Trapped Particles," J. Geophys. Res. 81, 4029, 1976.
14. G.C. Theodoridis, F.R. Pachini, "Pitch Angle Diffusion of Relativistic Outer-Belt Electrons," Annales de Geophysique 23, 375, 1967.
15. C. F. Kennel; "Consequences of a Magnetospheric Plasma," Rev. Geophys. 7, 373, 1969.
16. T. A. Fritz; "The Pitch Angle Distribution of > 40 keV Electrons," Magnetospheric Physics, B. M. McCormac, ed., Reidel, Dordrecht, Holland, p. 105, 1974.
17. L. R. Lyons, R. M. Thorne; "Equilibrium Structure of Radiation Belt Electrons," J. Geophys. Res. 78, 2142, 1973.
18. M. Schulz; "Relation Between Bounce-Averaged Collisional Transport Coefficients for Geomagnetically Trapped Electrons," J. Geophys. Res. 81, 5212, 1976.
19. L. R. Lyons, R. M. Thorne, C. F. Kennel; "Pitch-Angle Diffusion of Radiation Belt Electrons within the Plasmasphere," J. Geophys. Res. 77, 3455, 1972.
20. L. R. Lyons, R. M. Thorne, C. F. Kennel; "Electron Pitch Angle Diffusion Driven by Oblique Whistler Mode Turbulence," J. Plasma Phys. 6, 589, 1971.
21. W. N. Spjeldvik, R. M. Thorne; "The Cause of Storm After Effects in the Middle Latitude D-Region," J. Atm. Terr. Phys. 37, 777, 1975.
22. W. Spjeldvik, "Radiation Belt Electrons, Structure of the Loss Cone," (unpub.) NOAA, ERL, Boulder, Colorado.
23. J. B. Cladis, G. T. Davidson, L. L. Newkirk; eds., The Trapped Radiation Handbook, Defense Nuclear Agency, Washington, D.C. 20305, DNA 2524H, revised 1974.
24. M. Ben-Ari, Aharon Eviatar; "Replenishment of Electrons Lost in the South Atlantic Anomaly by Gyroresonant Pitch-Angle Diffusion," Plan Sp. Sci 23, 671, 1975.
25. W. L. Imhof; "Electron Precipitation in the Radiation Belts," J. Geophys. Res. 73, 4167, 1968.

26. E.J. Fremouw, R.C. Livingston, "WIDEBAND Satellite Observations," SRI, Menlo Park, Calif., Bimonthly Report, Oct. 20, 1976.
27. F.W. Perkins, "Plasma-wave Instabilities in the Ionosphere Over the Aurora," J. Geophys. Res. 73, 6631, 1968.
28. J.M. Kindel and C.F. Kennel, "Topside Current Instabilities," J. Geophys. Res., 76, 3055, 1971.
29. L.P. Block, "Potential Double Layers in the Ionosphere," Cosmic Electrodyn. 3, 349, 1972.
30. L.P. Block, "Double Layers, Physics of the Hot Plasma in the Magnetosphere" in Proc. Thirtieth Nobel Symp., Plenum Press, 1975.
31. P. Carlqvist and R. Bostrom, "Space Charge Regions Above the Aurora," J. Geophys. Res., 75, 7140, 1970.
32. K. Papadopoulos and T. Coffey, "Nonthermal Features of the Aurora Plasma Due to Precipitating Electrons," J. Geophys. Res., 79, 674, 1974.
33. D.W. Swift, "On the Formation of Auroral Arcs and Acceleration of Auroral Electrons," J. Geophys. Res. 80, 2096, 1975.
34. D.W. Swift, H.C. Stenbaek-Nielsen, and R.J. Hallinan, "An Equipotential Model for Auroral Arcs," J. Geophys. Res., 81, 3931, 1976.
35. K. Papadopoulos, "A Review of Anomalous Resistivity for the Ionosphere," NRL Memorandum Report 3275, 1976.
36. R.A. Hoffman and D.S. Evans, "Field-Aligned Electron Bursts at High Latitude Observed by OGO-4," J. Geophys. Res., 73, 6201, 1968.
37. D.S. Evans, B. Maehlum and T. Wedde, "High Latitude Observations of Field Aligned Electron Beams," EOS Trans. Am. Geophys. Union, 52, 731, 1972.
38. G. Paschman, R.G. Johnson, R.D. Sharp, and E.G. Shelley, "Angular Distributions of Auroral Electrons in the Energy Range 0.8-16 keV," J. Geophys. Res., 77, 6111, 1972.
39. B.N. Maehlum and H. Moestue, "High Temporal and Spatial Resolution Observations of Low Energy Electrons by a Mother-Daughter Rocket in the Vicinity of Two Quiescent Auroral Arcs," Planet. Space Sci., 21, 1957, 1973.

40. R.L. Arnoldy, P.B. Lewis and P.O. Isaacson, "Field-Aligned Auroral Electron Fluxes," J. Geophys. Res., 79, 4208, 1974.
41. J.M. Bosqued, G. Cardona and H. Reme, "Auroral Electron Fluxes Parallel to the Geomagnetic Field Lines," J. Geophys. Res., 79, 98, 1974.
42. B. Hultqvist, H. Borg, W. Riedler and P. Christopherson, "Observations of a Magnetic Field-Aligned Anisotropy for 1 and 6 keV Positive Ions in the Upper Ionosphere," Planet. Space Sci., 19, 279, 1971.
43. H. Reme and J.M. Bosqued, "Evidence Near the Auroral Ionosphere of a Parallel Electric Field Deduced from Energy and Angular Distributions of Low-Energy Particles," J. Geophys. Res., 76, 7683, 1971.
44. E.M. Wescott, H.C. Stenbaek-Nielsen, T.N. Davis, W.B. Murcray, H.M. Peek, and P.J. Bottoms, "The Oosik Barium Plasma Injection Experiment and Magnetic Storm of March 7, 1972," J. Geophys. Res., 80, 951, 1975.
45. G. Haerendel, E. Rieger, A. Valenzuela, H. Foppl, and H. Stenbaek-Nielsen, "First Observation of Electrostatic Acceleration of Barium Ions into the Magnetosphere," Preprint, Max Planck Institute for Physics and Astrophysics, Garching, 1976.
46. F.S. Mozer, "Anomalous Resistivity and Parallel Electric Fields," Tech. Report, Space Sci. Lab., University of Calif., Berkeley, 1975.
47. D.S. Evans, "Evidence for the Low Altitude Acceleration of Auroral Particles," in Physics of the Hot Plasma in the Magnetosphere, ed. by B. Hultqvist and L. Stenflo, Plenum Publ. Corp., New York, 1975.
48. M. Lampton, "Daytime Observations of Energetic Auroral-Zone Electrons," J. Geophys. Res., 72, 5817, 1967.
49. T. Winiecki, "Analysis of Rapid Temporal Fluctuations in Auroral Particle Fluxes," M. Sci. Thesis, Space Sci. Dept., Rice Univ., Houston, Texas, 1967.
50. R.L. Arnoldy, "Rapid Fluctuations of Energetic Auroral Particles," J. Geophys. Res., 75, 228, 1970.
51. O. Buneman, "Dissipation of Currents in Ionized Media," Phys. Rev. 115, 503, 1959.
52. J.D. Jackson, "Longitudinal Plasma Oscillations," J. Nucl. Energy, C(1), 171, 1960.

53. I.B. Bernstein, and R.M. Kulsrud, "Ion Wave Instabilities," Phys. Fluids, 109, 937, 1960.
54. O. Penrose, "Electrostatic Instabilities of a Uniform Non-Maxwellian Plasma," Phys. Fluids, 3, 258, 1960.
55. B.D. Fried and R.W. Gould. "Longitudinal Ion Oscillations in a Hot Plasma," Phys. Fluids, 4, 139, 1961.
56. O. Buneman, "Excitation of Field-Aligned Sound Waves by Electron Streams," Phys. Rev. Letters, 10, 285, 1963.
57. M.C. Kelley and F.S. Mozer, "Electric Field and Plasma Density Oscillations Due to High-Frequency Hall Current Two-Stream Instability in the Auroral E-Region," J. Geophys. Res., 78, 2214, 1973.
58. J.B. Cladis, G.T. Davidson, W.E. Francis, L.L. Newkirk and M. Walt, Investigation of Phenomena Affecting Auroral Ionosphere, Final Report DNA 3327F, 15 May 1974.
59. E. Ungstrup, A. Bahnsen, J.K. Olesen, F. Primdahl, F. Spangler, W.J. Heikkila, D.M. Klumpar, J.D. Winningham, U. Fahleson, C.G. Falthammar, and A. Pederson; "Rocket-Borne Particle, Field and Plasma Observations in the Cleft Region," Geophys. Res., Letters, 2, 345, 1975.
60. K.L. Bowles, B.B. Balsley, and R. Cohen, "Field-Aligned E-Region Irregularities Identified with Acoustic Plasma Waves," J. Geophys. Res., 68, 2485, 1963.
61. B.B. Balsley, "Some Characteristics of Non Two-Stream Irregularities in the Equatorial Electrojet," J. Geophys. Res., 74, 2333, 1969.
62. W.G. Chesnut, Stanford Research Institute (personal communication).

DISTRIBUTION LIST

DEPARTMENT OF DEFENSE

Director
 Defense Advanced Research Proj. Agency
 ATTN: Nuclear Monitoring Research
 ATTN: Strategic Tech. Office

Defense Communication Engineer Center
 ATTN: Code R103, J. Raffensberger
 ATTN: Code 700, J. Lebo
 ATTN: Code R103, D. T. Worthington
 ATTN: Code R720, John Worthington

Director
 Defense Communications Agency
 ATTN: Code 810, R. W. Rostron

Defense Documentation Center
 Cameron Station
 12 cy ATTN: TC

Director
 Command, Control Technical Center
 ATTN: C650, W. Heidig

Director
 Defense Intelligence Agency
 ATTN: DT-1, Mr. Knoll
 ATTN: DT-1C
 ATTN: DI-7D

Director
 Defense Nuclear Agency
 ATTN: RAAE, Gordon Soper
 ATTN: STVL, E. Lavier
 ATTN: RAAE, Major R. Bigoni
 ATTN: RAEV
 2 cy ATTN: RAAE, Charles A. Blank
 ATTN: TISL, Archives
 3 cy ATTN: TITL, Tech. Library
 ATTN: RAAE, Paul Fleming

Dir. of Defense Research & Engineering
 Department of Defense
 ATTN: S&SS (OS)

Commander
 Field Command
 Defense Nuclear Agency
 ATTN: FCPR

Director
 Interservice Nuclear Weapons School
 ATTN: Document Control

Director
 Joint Strat. Target Planning Staff, JCS
 ATTN: Doc. Control

Chief
 Livermore Division, Field Command, DNA
 Lawrence Livermore Laboratory
 ATTN: FCPRL

DEPARTMENT OF DEFENSE (Continued)

Director
 National Security Agency
 ATTN: TDL
 ATTN: Technical Library

OJCS/J-3
 ATTN: WWMCCS, Eval. Ofc. Mr. Toma
 ATTN: J-3, Environmental Services Div.

OJCS/J-5
 ATTN: Nuc. Div.

DEPARTMENT OF THE ARMY

Commander/Director
 Atmospheric Sciences Laboratory
 US Army Electronics Command
 ATTN: R. Olsen
 ATTN: E. Butterfield, DRSEL-BL-SY-R
 ATTN: F. E. Miles, DRSEL-BL-SY-S
 ATTN: Robert Rubio
 ATTN: H. Ballard

Director
 BMD Advanced Tech. Center
 Huntsville Office
 ATTN: ATC-T, Melvin T. Capps
 ATTN: ATC-O, W. Davies

Program Manager
 BMD Program Office
 ATTN: DACS-BMT, John Shea

Commander
 BMD System Command
 ATTN: BDMSC-TEN, Noah J. Hurst

Dep. Chief of Staff for Research Dev. & Acq.
 Department of the Army
 ATTN: DAMA-WSZ-C
 ATTN: DAMA-CSZ-C

Chief of Engineers
 Department of the Army
 ATTN: Fernand DePercin

Deputy Chief of Staff for Ops. & Plans
 Department of the Army
 ATTN: DAMO-DDC, COL David W. Einsel
 ATTN: DAMC-SSN

Commander
 Harry Diamond Laboratories
 2 cy ATTN: DRXDO-NP, F. N. Wimenitz

Director
 US Army Ballistic Research Labs.
 ATTN: Tech. Lib., Edward Bailey
 ATTN: John C. Mester
 ATTN: J. Heimerl
 ATTN: M. Aregel

PRECEDING PAGE BLANK-NOT FILLED

DEPARTMENT OF THE ARMY (Continued)

Commander
US Army Electronics Command
ATTN: DRSEL-RD-P
ATTN: DRSEL-PL-ENV, Hans A. Bomke
ATTN: DRSEL-IL-IR, Edwin T. Hunter
ATTN: DRSEL-XL-D
ATTN: Stanley Eronenberg

Commander
US Army Foreign Science & Tech. Center
ATTN: R. Jones

Commander
US Army Materiel Dev. & Readiness Command
ATTN: DRCLDC, J. A. Bender
ATTN: DRXCD-TL

Commander
US Army Missile Command
ATTN: DRSMI-XS, Chief Scientist
ATTN: DRSMI-ABL

Commander
US Army Nuclear Agency
ATTN: MONA-WE, J. Berberet

Commander
US Army Satcom Agency
ATTN: Technical Library

Chief
US Army Research Office
ATTN: ORDARD-P, Robert Mace
ATTN: ORDARD-DCS, Hermann R. Robl

Commander
Whippany Field Office (BMDSC-WS-Q)
Bell Telephone Laboratories
ATTN: John Turner

Commander
White Sands Missile Range
ATTN: STWS-TE-NT, Marvin P. Squires
ATTN: AMSEL-NL-SD, Willis W. Webb

DEPARTMENT OF THE NAVY

Chief of Naval Operations
Navy Department
ATTN: OP 981
ATTN: Code 604C3, Robert Piacesi

Chief of Naval Research
Navy Department
ATTN: Code 461, Jacob L. Warner
ATTN: Code 461, R. Gracen Joiner

Commander
Naval Electronic Systems Command
Naval Electronic Systems Command Hqs.
ATTN: ELEX 03
ATTN: PME 117-T, Satellite Comms. Project Off.

Commanding Officer
Naval Intelligence Support Center
ATTN: Code 40A, E. Blase
ATTN: Document Control

DEPARTMENT OF THE NAVY (Continued)

Commander
Naval Ocean Systems Center
ATTN: Code 2200, Jorgen Richter
ATTN: William F. Moler
ATTN: Code 2200, Richard Pappert
ATTN: Code 2200, Tiam Ruthmuller
TN: Tech. Lib. for T. J. Keary

Superintendent (Code 1424)
Naval Postgraduate School
ATTN: Code 61, DY, J. N. Dyer
ATTN: Code 61, MN, E. A. Mine
ATTN: Code 2124, Tech. Rpts. Librarian

Director
Naval Research Laboratory
ATTN: Code 4004, Emanuel L. Brancato
ATTN: Code 5174, Frederick W. Raymond
ATTN: Code 7125.7, Donald J. Horan
ATTN: Code 6625, Francis J. Campbell
ATTN: Code 6604F, Richard L. Statler
ATTN: Code 2600, Tech. Lib.
ATTN: Code 7127, Charles Y. Johnson
ATTN: Code 7128, James D. Kurfess
ATTN: W. Neil Johnson
ATTN: Code 7120, Gerald H. Share
ATTN: Code 7701, Jack D. Brown
ATTN: Code 7709, Wahab Ali
ATTN: Code 7750, Klaus Bain
ATTN: Code 7750, J. Bolder
ATTN: Code 7750, J. Davis
ATTN: Code 7750, S. L. Ossakow
ATTN: Code 7120, Robert L. Kinzer
ATTN: Code 7700, Timothy P. Coffey
ATTN: Code 7750, Darrell Strobel

Commander
Naval Surface Weapons Center
ATTN: Code WA501, Navy Nuc. Prgms. Off.
ATTN: Code WX21, Tech. Lib.
ATTN: D. L. Land
ATTN: L. Rudlin

Commander
Naval Weather Service Command
Naval Weather Service Headquarters
ATTN: Mr. Martin

Commanding Officer
Navy Astronautics Group
6 cy ATTN: W. J. Gleason

Commanding Officer
Nuclear Weapons Training Center Pacific
Naval Air Station, North Island
ATTN: Nuclear Warfare Department

Commander
Nuclear Weapons Training Group Atlantic
ATTN: Nuclear Warfare Department

DEPARTMENT OF THE AIR FORCE

Commander
ADC/DO
ATTN: DOF
ATTN: DOFS
ATTN: DOA

DEPARTMENT OF THE AIR FORCE (Continued)

Commander
ADCOM/XPD
ATTN: XPQDQ
ATTN: Bqs. 15th Aerospace Force (LVN)
ATTN: XPQDQ, Maj G. Kuch

AF Geophysics Laboratory, AFSC
ATTN: OPR, Alva T. Stair
ATTN: L&B, William Swider, Jr.
ATTN: LKB, A. Laire
ATTN: L. Katz
ATTN: PHG, J. C. McClay
ATTN: LKB, Kenneth S. W. Champion
ATTN: OP, John S. Garing
ATTN: LKB, Socco S. Naresi
ATTN: LKS, F. R. Innes
ATTN: LKO, Robert E. Hutiman
ATTN: OPR, F. DeGrego
ATTN: OPR, J. Kennealy
ATTN: OPR, T. Connelly
ATTN: SPOLA, E. L. Cunha
ATTN: OPR-1, J. C. Ulwick
ATTN: LKB, F. B. Innes
ATTN: LKB, T. Kemeshea
ATTN: OPR, F. Billingley
ATTN: LKS, R. A. VanTassel
ATTN: OPR, R. E. Murphy
ATTN: OPR, H. Gardener
ATTN: OPR, R. O'Neill

AF Weapons Laboratory, AFSC
ATTN: SUL
ATTN: DYT, Capt Gary D. Cable
ATTN: DYT, Capt Hollars
ATTN: CA, Arthur H. Guenther
ATTN: DYC, Joseph Janni
ATTN: CC, Col G. J. Freyer

AFTAC
ATTN: Tech. Lib.
ATTN: TF/Maj Wiley
ATTN: TN
ATTN: TN-E, Lt Col E. C. Thomas

Headquarters
Air Force Systems Command
ATTN: DLS
ATTN: Lt Col B. C. Nealy
ATTN: Lt Col W. Beam
ATTN: Lt Col H. Simmons
ATTN: DLXP, Capt Roisel
ATTN: SCTSW, Wpns. & Wpns. Effects Div.
ATTN: SDS/DLSE
ATTN: DCLAW

Headquarters
Electronic Systems Division, (AFSC)
ATTN: James Whelan
ATTN: W. C. Morton

Headquarters
Electronic Systems Division/ES
ATTN: ESTT

Commander
Foreign Technology Division, AFSC
ATTN: NICD, Library
ATTN: TDPSS, Kenneth N. Williams

DEPARTMENT OF THE AIR FORCE (Continued)

Hq. USAF/IN
ATTN: IN

Hq. USAF/RD
ATTN: RDPM
ATTN: RDSA
ATTN: RDPS
ATTN: RDQSM
ATTN: RD

Commander
Rome Air Development Center, AFSC
ATTN: OCSE, J. J. Simons
ATTN: EMILD, Doc. Library
ATTN: V. Govne

SAMSO/AW
1b cy ATTN: AWX

SAMSO/SZ
ATTN: SZJ, Major Lawrence Doan

Commander in Chief
Strategic Air Command
ATTN: XPFS, Maj Brian G. Stephan
ATTN: ADW, Lt Col J. S. Greene, Jr.
ATTN: ADWATE, Capt Bruce Bauer

USAFETAC/CB
ATTN: CBT, Mr. Cresti

Commander
ASD
ATTN: ASD-YH-EX, Lt Col Robert Leverette

DET 1, 12 WS
Space Forecasting Section
ATTN: Capt R. M. Heslin

ENERGY RESEARCH & DEVELOPMENT ADMINISTRATION

Division of Military Application
CS Energy Research & Dev. Admin.
ATTN: Doc. Con. for Frank A. Ross
ATTN: Doc. Con. for Colonel T. Cross
ATTN: Doc. Con. for David H. Slade
ATTN: Doc. Con. for Major D. A. Baycock

University of California
Lawrence Livermore Laboratory
ATTN: Tech. Info. Dept. L-3
ATTN: J. F. Tinney, L-517

Sandia Laboratories
Livermore Laboratory
ATTN: Doc. Con. for Thomas B. Cook, Org. 8000

Sandia Laboratories
ATTN: Doc. Con. for W. D. Brown, Org. 1353
ATTN: Doc. Con. for J. C. Eckhardt, Org. 1250
ATTN: Doc. Con. for Clarence R. Mehl, Org. 5230
ATTN: Doc. Con. for Org. 9220
ATTN: Doc. Con. for Morgan L. Kramm, Org. 5720
ATTN: Doc. Con. for 3422, Sandia Rpt. Coll.

ENERGY RESEARCH & DEVELOPMENT ADMINISTRATION
(Continued)

Los Alamos Scientific Laboratory

ATTN: Doc. Con. for J. Judd
ATTN: Doc. Con. for R. A. Jeffries
ATTN: Doc. Con. for Martin Tierney, J-10
ATTN: Doc. Con. for E. A. Bryant, (NO DASIAC)
ATTN: Doc. Con. for Donald Kerr
ATTN: Doc. Con. for David W. Steinhaus
ATTN: Doc. Con. for E. W. Hones, Jr.
ATTN: Reference Library, Ann Beyer
ATTN: Doc. Con. for S. Rockwood
ATTN: Doc. Con. for William Maier
ATTN: Doc. Con. for John Zinn
ATTN: Doc. Con. for W. D. Barfield
ATTN: Doc. Con. for Marge Johnson
ATTN: Doc. Con. for W. M. Hughes, MS 559
ATTN: Doc. Con. for John S. Malik
ATTN: D. M. Rohrer, MS 518

US Energy Research & Dev. Admin.
Division of Headquarters Services
Library Branch G-043

ATTN: Doc. Con. for Richard J. Kandel
ATTN: Doc. Con. for H. H. Kurzweg
ATTN: Doc. Con. for D. Kohlstad
ATTN: Doc. Con. for George L. Rogosa
ATTN: Doc. Con. for Class Tech. Lib.
ATTN: Doc. Con. for Rpts.
ATTN: Doc. Con. for Joseph D. LaFleur

OTHER GOVERNMENT AGENCIES

Central Intelligence Agency
ATTN: RD/SI, Rm. 5048 Hq. Bldg. for NED/OSI -
2048 Hqs.

Department of Commerce
National Bureau of Standards

ATTN: Sec. Officer for M. Krauss
ATTN: Sec. Officer for J. Cooper
ATTN: Sec. Officer for D. R. Lide
ATTN: Sec. Officer for Lewis H. Gevantman
ATTN: Sec. Officer for Office of Director
ATTN: Sec. Officer for M. Scheer
ATTN: Sec. Officer for D. Garvin
ATTN: Sec. Officer for B. Stiener
ATTN: Sec. Officer for George A. Sinnatt
ATTN: Sec. Officer for K. Keesler

Department of Commerce
Office of Telecommunications
Institute for Telecom Science
ATTN: William F. Utlaut

NASA

Goddard Space Flight Center
ATTN: R. F. Benson
ATTN: H. A. Taylor
ATTN: M. Suglura
ATTN: S. J. Bauer
ATTN: James I. Vette
ATTN: J. Siry
ATTN: Technical Library
ATTN: Gilbert D. Mead, Code 641
ATTN: G. Levin
ATTN: A. C. Aiken
ATTN: A. Tempkin
ATTN: J. P. Hepner

OTHER GOVERNMENT AGENCIES (Continued)

NASA

George C. Marshall Space Flight Center
ATTN: W. T. Roberts
ATTN: R. Chappell
ATTN: R. D. Hudson
ATTN: N. H. Stone
ATTN: C. R. Balcher
ATTN: W. A. Oran

NASA

ATTN: R. A. Schiffer
ATTN: M. Tepper
ATTN: D. P. Gauffman
ATTN: G. Sharp
ATTN: J. Findlay
ATTN: A. Schardt
ATTN: Code ST, W. L. Taylor
ATTN: P. Eaton
ATTN: R. Fellows
ATTN: Code ST, D. R. William
ATTN: E. R. Schmerling
ATTN: J. Naugle

NASA

Johnson Space Center
ATTN: Owen Garriot
ATTN: Classified Lib., Code BM6

NASA

Ames Research Center
ATTN: C. P. Sonett
ATTN: N-245-3, Palmer Dyal
ATTN: M-254-4, R. Whitten
ATTN: X-245-4, Ila G. Poppoff

NASA Scientific & Technical Info. Fac.
ATTN: SAR/DLA-385
ATTN: Acq. Branch

National Oceanic & Atmospheric Admin.
National Weather Service
Department of Commerce
ATTN: L. Machta
ATTN: J. K. Angell

National Oceanic & Atmospheric Admin.
National Ocean Survey
Department of Commerce
Washington Science Center
ATTN: John W. Townsend, Jr.
ATTN: Ronald L. Lavoie
ATTN: Edward S. Epstein
ATTN: Wayne McGovern
ATTN: Gerald A. Peterson

National Oceanic & Atmospheric Admin.
Environmental Research Laboratories
Department of Commerce
ATTN: A. H. Snalley
ATTN: R4J, Donald J. Williams
ATTN: RX1, Robert W. Knecht
ATTN: Robert B. Doeker
ATTN: R43, Herbert H. Sauer
ATTN: Eldon Ferguson
ATTN: Walther N. Spjeldvik
ATTN: George C. Reid, Aeronomy Lab.

OTHER GOVERNMENT AGENCIES (Continued)

National Science Foundation
ATTN: W. D. Adams
ATTN: Fred D. White
ATTN: M. K. Wilson
ATTN: Rolf Sinclair
ATTN: R. S. Zapolisky
ATTN: E. P. Todd
ATTN: W. H. Cramer
ATTN: R. Manka
ATTN: F. Gilman Blake

US Arms Control & Disarmament Agency
ATTN: Office of Director
ATTN: Reference Info. Center

DEPARTMENT OF DEFENSE CONTRACTORS

Aerodyne Research, Inc.
ATTN: M. Camac

Aeronomy Corporation
ATTN: S. A. Bowhill

Aerospace Corporation
ATTN: Julian Reinheimer
ATTN: J. Sorrels
ATTN: G. Millburn
ATTN: V. Josephson
ATTN: M. Berg
ATTN: L. W. Aukerman
ATTN: V. Wall
ATTN: J. Woodford
ATTN: S. P. Bower
ATTN: F. Keller
ATTN: R. D. Rawcliffe
ATTN: George Paulikas
ATTN: T. Friedman
ATTN: D. C. Pecka
ATTN: J. Stevens
ATTN: J. B. Blake
ATTN: N. Cohen
ATTN: Harris Mayer
ATTN: Thomas D. Taylor

Analytical Systems Engineering Corp.
ATTN: J. A. Caruso

Battelle Memorial Institute
ATTN: Donald J. Hamman
ATTN: Radiation Eff. Info. Center

The Boeing Company
ATTN: Glen Keister

The Trustees of Boston College
Chestnut Hill Campus
ATTN: R. Hegblom
ATTN: R. L. Casovillao
2 cy ATTN: Chairman, Dept. of Chem.
ATTN: R. Eather
ATTN: Library for Technical Documents

Brown Engineering Company, Inc.
ATTN: J. E. Cato
ATTN: J. Dobkins
ATTN: Roland Patrick
ATTN: Romeo A. DeLiberis

DEPARTMENT OF DEFENSE CONTRACTORS (Continued)

Univ. of California at Los Angeles
Office of Contract & Grant Admin.
ATTN: T. A. Farley, Space Sci. Ltr.

Univ. of California at Riverside
ATTN: James N. Pitts, Jr.
ATTN: Alan C. Lloyd

Univ. of California at San Diego
ATTN: C. E. McIlwain, Physics Dept.
ATTN: S. C. Lin

University of California
Berkeley Campus Room 318
Sproul Hall
ATTN: Kinsey A. Anderson

State of California Air Resources Board
ATTN: Leo Zafonte

University of California
Space Sciences Laboratory
ATTN: Bodo Parady

Calspan Corporation
ATTN: Robert A. Fluerge
ATTN: M. G. Dunn
ATTN: Technical Library
ATTN: W. Wurster
ATTN: C. E. Treanor

University of Colorado
Office of Contracts & Grants
ATTN: Jeffrey B. Pearce, LASP
ATTN: Charles A. Barth, LASP
ATTN: A. Phelps, JILA
ATTN: C. Lineberger, JILA

The Trustees of Columbia University
City of New York
ATTN: Sec. Officer, H. M. Foley
ATTN: Richard N. Zare

Comsat Laboratories
ATTN: Document Control

Epsilon Laboratories, Inc.
ATTN: Henry Miranda
ATTN: Carl Accardo

Computer Sciences Corporation
ATTN: C. Hulbert

ESL, Inc.
ATTN: James Marshall

General Dynamics Corp.
Convair Division
ATTN: Library, D. H. McCoy
ATTN: Library, 128-00

General Electric Company
Re-Entry & Environmental Systems Div.
ATTN: A. A. Sinisgalli

DEPARTMENT OF DEFENSE CONTRACTORS (Continued)

General Electric Company
Space Division
Valley Forge Space Center
ATTN: P. Zavitsanos
ATTN: Joseph C. Peden, CCF 8401
ATTN: Tech. Info. Center
ATTN: M. H. Bortner, Space Sci. Lab.
ATTN: F. Alvea
ATTN: T. Baurer

General Electric Company
TIMPO-Center for Advanced Studies
ATTN: Don Chandler
ATTN: B. Gambill
ATTN: Mike Durlash
ATTN: Warren S. Knapp
5 cy ATTN: DASIAC
ATTN: Tim Stephens

General Research Corporation
ATTN: John Ise, Jr.

General Research Corporation
Washington Operations
ATTN: Thomas M. Zakrzewski

Geophysical Institute
University of Alaska
ATTN: R. Parthasarathy
ATTN: J. S. Wagner, Physics Dept.
ATTN: T. N. Davis
ATTN: A. Belon
ATTN: S. I. Akasofu
ATTN: D. J. Henderson
ATTN: Neal Brown
ATTN: Henry Cole
ATTN: Technical Library

Crumman Aerospace Corporation
ATTN: Michael D. Agostino
ATTN: Marton Rossi

Harvard College Observatory
Smithsonian Astrophysical Observatory
Center for Astrophysics
ATTN: J. Patrick Henry

HRB-Singer, Inc.
ATTN: Tech. Info. Center 650, L. J. McBride

HSS, Inc.
ATTN: H. Stewart
ATTN: M. P. Shuler
ATTN: Donald Hansen

IBM Corporation
ATTN: Technical Rpts. Center (912 A816)

IIT Research Institute
ATTN: Technical Library

Institute for Defense Analyses
ATTN: Joel Bengtson
ATTN: IDA Librarian, Ruth S. Smith
ATTN: Hans Wolfhard

Johns Hopkins University
Applied Physics Laboratory
ATTN: Document Librarian
ATTN: Peter E. Partridge
ATTN: S. M. Krimigis

DEPARTMENT OF DEFENSE CONTRACTORS (Continued)

Kaman Sciences Corporation
ATTN: Frank H. Shelton
ATTN: Library

Lockheed Missiles & Space Company, Inc.
ATTN: D. R. Churchill
ATTN: J. Cretcher
ATTN: S. T. Weiss, D/68-01
ATTN: D. L. Crowther, D/62-25
ATTN: Edwin A. Smith, Dept. 85-85
ATTN: F. E. Crowther, D/60-01
ATTN: J. H. Bockenberry, D/60-07
ATTN: J. T. Hart, Jr., D/61-03
ATTN: Q. A. Riepe, D/60-80
ATTN: D. F. McClinton

Lockheed Missiles & Space Company, Inc.
ATTN: R. D. Sharp, D/52-12
ATTN: Richard G. Johnson, Dept. 52-12
ATTN: L. L. Newkirk, D/52-21
ATTN: John B. Cladis, Dept. 52-12
ATTN: W. E. Francis, D/52-12
ATTN: G. T. Davidson, D/52-54
ATTN: Martin Walt, Dept. 52-10
ATTN: John E. Evans, Dept. 52-54
ATTN: Tech. Info. Center, D/COIL
ATTN: R. K. Landshoff
ATTN: W. D. Frye, D/52-21
ATTN: W. I. Imhof, D/52-12
ATTN: T. D. Dassel
ATTN: G. H. Nakano
ATTN: R. D. Meyerott
ATTN: J. B. Reagan, D/52-12
ATTN: James W. Schallau
ATTN: R. P. Caren, D/52-20
ATTN: D. C. Fisher, D/52-14
ATTN: Billy M. McCormac, Dept. 52-54
ATTN: A. D. Anderson, D/52-54
ATTN: R. A. Breuch, D/52-21

Maxwell Laboratories, Inc.
ATTN: Victor Fargo

McDonnell Douglas Corporation
ATTN: William Olsen
ATTN: A. D. Goedeke

University of Minnesota
ATTN: J. R. Winkler

Mission Research Corporation
ATTN: R. Hendrick
ATTN: D. Sappenfield
ATTN: Conrad L. Longmire
ATTN: D. Archer
ATTN: Dave Sowle
ATTN: M. Scheibe

The Mitre Corporation
ATTN: Tech. Lib. for B. Troutman
ATTN: P. Grant
ATTN: Library
ATTN: Tech. Lib. for R. Greeley

National Academy of Sciences
ATTN: National Materials Advisory Board for
Edward R. Dyer
ATTN: National Materials Advisory Board for
J. R. Sievers
ATTN: National Materials Advisory Board for
William C. Bartley

DEPARTMENT OF DEFENSE CONTRACTORS (Continued)

Pennsylvania State University
Industrial Security Office
ATTN: J. S. Nisbet
ATTN: I. Hale

Photometrics, Inc.
ATTN: Irving L. Kofsky

Physical Dynamics, Inc.
ATTN: A. Thompson
ATTN: Joseph B. Workman

Physical Sciences, Inc.
ATTN: Kurt Wray
ATTN: K. L. Taylor

University of Pittsburgh of the Comwlth. Sys. of
Higher Education
Cathedral of Learning
ATTN: Frederick Kaufman
ATTN: Manfred A. Biondi

R & D Associates
ATTN: R. G. Lindgren
ATTN: Robert E. Lelevier
ATTN: Albert L. Latter
ATTN: H. A. Dry
ATTN: William J. Karzas
ATTN: William R. Graham, Jr.
ATTN: Forrest Gilmore
ATTN: P. Turco

R & D Associates
ATTN: Herbert J. Mitchell

The Rand Corporation
ATTN: Technical Library
ATTN: Paul Tamarin
ATTN: Cullen Crain

Rice University
Department of Space Science
ATTN: Joseph Chamberlain
ATTN: Ronald F. Stebbings

Rockwell International Corporation
Space Division
ATTN: William Atwell

Sanders Associates, Inc.
ATTN: Jack Schwartz

Science Applications, Inc.
ATTN: D. Sachs
ATTN: Daniel A. Hamlin

Professor Chalmers F. Sechrist
ATTN: C. Sechrist

Smithsonian Astrophysical Observatory
ATTN: A. Dalgarno

University of Southern California
ATTN: S. W. Benson

Space Data Corporation
ATTN: Edward F. Allen

DEPARTMENT OF DEFENSE CONTRACTORS (Continued)

Stanford Research Institute
ATTN: Allen M. Peterson
ATTN: Felix T. Smith
ATTN: Arthur Lee Whitson
ATTN: B. R. Gasten
ATTN: Ray L. Leadabrand
ATTN: J. Lomax
ATTN: G. Black
ATTN: M. Baron
ATTN: Ronald White
ATTN: R. D. Hake, Jr.
ATTN: Walter G. Chesnut
ATTN: L. V. Cobb
ATTN: E. Kindermann
ATTN: James R. Peterson

Stanford Research Institute
ATTN: Warren W. Berning

Stanford University
Radio Science Laboratory
ATTN: R. S. Belliwell
ATTN: D. L. Carpenter

TRW Defense & Space Sys. Group
ATTN: Tech. Info. Center/S-1930
ATTN: R. K. Plebuch, R1-2078
ATTN: F. Scarf, R5-1280
ATTN: Robert M. Webb, R1-2410
ATTN: R. Watson, R1/1096
ATTN: O. E. Adams, R1-1144
ATTN: J. F. Frlichtenicht, R1-1196
ATTN: H. H. Holloway, R1-2016

United Technologies Corporation
ATTN: Robert B. Bullis
ATTN: H. Michels

Utah State University
ATTN: C. Wyatt
ATTN: Doran Baker
ATTN: D. Burt
ATTN: Kay Baker

VisiDyne, Inc.
ATTN: J. W. Carpenter

Wayne State University
ATTN: Pieter K. Rol, Chem. Engrg. & Mat.
Sci.
ATTN: R. H. Kummier

Wayne State University
Dept. of Physics
ATTN: Walter E. Kauppila